DLR-IB-FA-BS-2020-6

Structural Analysis and Validation of a 20m Wind Rotor Blade Model

Masterarbeit

Rakesh Ravi
Christian Willberg

DLR Deutsches Zentrum für Luft- und Raumfahrt

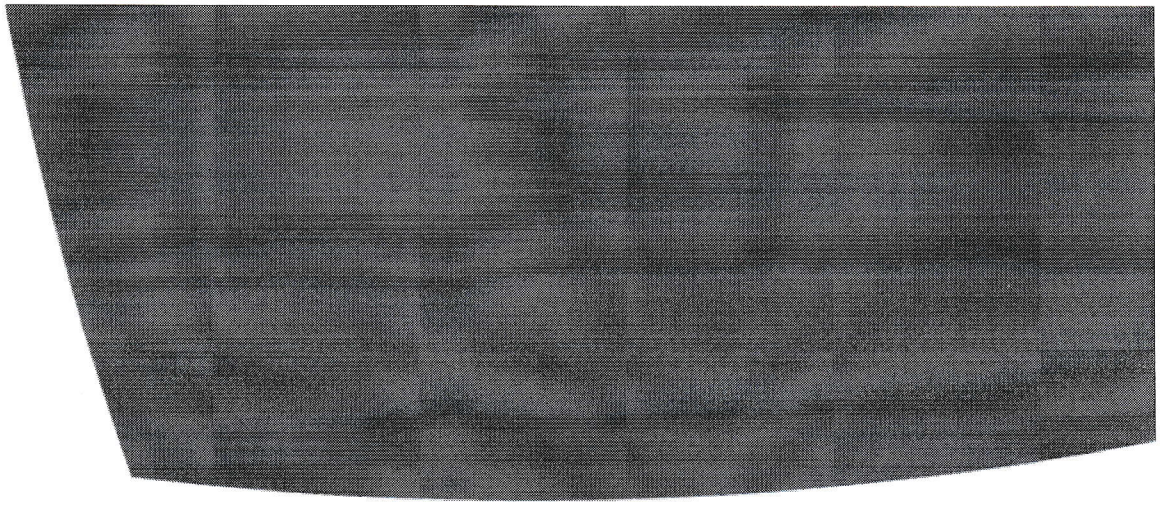

Institut für Faserverbundleichtbau und Adaptronik

DLR-IB-FA-BS-2020-6

Structural Analysis and Validation of a 20m Wind Rotor Blade Model

Zugänglichkeit:

Stufe 1 Allgemein zugänglich: Der Interne Bericht wird elektronisch ohne Einschränkungen in ELIB abgelegt. Falls vorhanden, ist je ein gedrucktes Exemplar an die zuständige Standortbibliothek und an das zentrale Archiv abzugeben.

Braunschweig, *Juni, 2020*

Abteilungsleiter:
Dr.-Ing. Tobias Wille

Der Bericht umfasst: 117 Seiten

Autoren:
M. Sc. Rakesh Ravi

Dr.-Ing. Christian Willberg

Deutsches Zentrum
DLR für Luft- und Raumfahrt

UNIVERSITÄT DUISBURG ESSEN

Offen im Denken

DLR

Fakultät für Ingenieurwissenschaften
Universität Duisburg-Essen, Campus Essen

Master Thesis

for attainment of the academic degree of

Master of Science

in

Computational Mechanics

Structural Analysis and Validation of a 20m Wind Rotor Blade Model

Author:

Rakesh Ravi

Mat. No: 3045892

January 16, 2020

Advisers:

Supervisor 1
Dr.-Ing. Christian Willberg
Deutsches Zentrum
für Luft- und Raumfahrt e.V. (DLR)
Institut für Faserverbundleichtbau
und Adaptronik

Supervisor 2
Dr.-Ing. Alexander Schwarz
Universität
Duisburg-Essen
Fakultät für
Ingenieurwissenschaften

Ravi, Rakesh:
Structural Analysis and Validation
of a 20m Wind Rotor Blade Model
Master Thesis, Universität Duisburg-Essen
Essen, 2019.

Abstract

The goal of this study is to validate the finite element model of a wind turbine blade based on the results from a test bench. The finite element model, its design discrepancies and the simulated experimental setup are explained. The design and tests were performed in the projects SmartBlades and SmartBlades 2. The following analyses have been carried out for verification purposes.

- Flapwise and edgewise extreme bending tests and comparison with global displacement and local strain measurements. There were four bending tests in total
- Torsion tests and comparison with global displacement and local strain measurements. There were three torsion tests in total

The compared data is analyzed. The effect of variations in load introduction and boundary conditions are studied. Eventually, the wind turbine blade and all data from the load case scenarios are published for further use.

Keywords Validation · Wind turbine blade · Structure mechanics · FEM

Contents

Abstract

1 Introduction
1.1 Motivation . . . 3
1.2 Scope . . . 4

2 Literature review
2.1 Wind turbine blade design . . . 5
2.2 Materials for wind turbine blades . . . 7
2.3 SmartBlades . . . 7
2.4 Full scale blade testing . . . 8
2.5 Finite element method theoretical insight . . . 10
2.5.1 Solid quadratic element . . . 10
2.5.2 Shell element . . . 11
2.6 MASS 21 - Structural Mass . . . 12

3 Experimental description
3.1 Experimental setup . . . 15
3.1.1 Preliminary note . . . 15
3.1.2 Initial setup . . . 15
3.2 Bending stiffness tests . . . 16
3.2.1 Introduction . . . 16
3.2.2 Testing Procedure . . . 17
3.2.3 Blade orientations during the static bending tests . . . 18
3.3 Strain Rosette for Strain Measurement . . . 18
3.3.1 Test execution . . . 20
3.4 Torsional stiffness tests . . . 20
3.4.1 Introduction . . . 20
3.4.2 Test execution . . . 20
3.4.3 Load scenarios . . . 22

4 Model description and validation
4.1 Material and Layup 23
4.2 Finite element model 24
4.3 Discrepancies to design 24
4.4 Boundary conditions 26
4.5 Load introduction 26

5 Results and discussions
5.1 Scenarios and variations 29
5.2 Displacement 29
5.3 Strain measurements 32
5.3.1 Mxmax results 32
5.3.2 Mxmin results 43
5.3.3 Mymax results 53
5.3.4 Mymin results 63
5.4 Torsion results 74
5.4.1 Displacement plots for all the torsion load cases 75
5.4.2 Strain plots - Torsion LC_1 77
5.4.3 Strain plots - Torsion LC_2 81
5.4.4 Strain plots - Torsion LC_3 85
5.5 Effect of orientation of the blade 85

6 Summary and Conclusions
6.1 Summary 89
6.2 Conclusion 91

A Load frame geometry

B Strain guage list

C List of Figures

D List of Tables

E Bibliography

1 Introduction

1.1 Motivation

Wind energy has emerged as one of the key renewable energy sources of the world in generating sustainable energy. Particularly in Germany it plays a major role in future energy generation. Strong state subsidies are intended to increase the share of wind energy in gross electricity generation from currently around 7% to 17% in 2020 and to 30% in 2030 [1]. In order to achieve this goal, two paths are being taken: On the one hand, so-called "repowering" involves replacing wind turbines on the coast or inland with more powerful ones. On the other hand, offshore wind farms with extremely powerful turbines of extreme size and class are being planned to a considerable extent far off the coast. Because of this reason current researches in this field are working on achieving high degree of utilization as well as enhancing the structural durability of wind turbines. Therefore, the ability to identify the structural damage and prevent component failure is a significant tool of interest which ultimately helps in reducing the cost of energy.
Wind turbine rotor blades are essential substructures of wind turbines. They carry huge loads in the process of capturing energy from the wind. They must be designed to maximize performance and dependability. At the same time care must be taken to minimize their cost as they contribute to about 20% overall cost of the wind turbine [2]. With increasing energy demand there is a need to increase the power output. To achieve this the size of the turbine blades have increased over the past three decades[3].

As the size of the turbine blades increases they are susceptible to failure more frequently than smaller turbine blades. Thus there is a need to reduce the weight which can be achieved by implementing lighter designs. After implementing a new design, the rotor blade must undergo testing in order to check whether it meets the design criteria. Testing also helps in under-

standing the failure mechanisms in a better manner. Furthermore, to complement the experimental studies, numerical models capable of predicting failure of rotor blades are also essential.

1.2 Scope

The Smartblades 2[1] rotor blade (20 m twist bend coupled blade) was subjected to various static tests, modal analysis and fatigue tests by Fraunhofer IWES . Static tests included bending and torsion stiffness tests. The blade was loaded flap-wise and edgewise with extreme loads for both the static and dynamic tests. The static tests were repeated once again after the dynamic tests [4].
A structural mechanics model based on finite element method was developed by DLR for the same rotor blade. This model is helpful to analyze the structural behavior.
The focus of this thesis is to validate this structural mechanic model by comparing the simulation results to the results from the test bench based on the static tests. Model Validation is a rigorous undertaking involving correct development, proposing an acceptable model and applying a correlation technique to enhance the model based on test results [5]. The outcome of the validation process is an understanding of the durability of the model and the modeling process to make useful forecasts.

[1] a BMWi funded research project

2
Literature review

2.1 Wind turbine blade design

The structural design of a wind turbine blade consists of a hollow air foil profile formed by two asymmetrically shaped shell structures glued together as seen in Figure 2.1 [6]. The two sides of the air foil forms the aerodynamic suction side and pressure side enabling the turbine blade to generate the necessary lift for the turbine to rotate. Wind turbines blades are designed mainly for two types of loads. They are the wind loads and the gravity loads. The wind loads act on the rotor blades in the flap-wise direction and the gravity loads act on the rotor blades in the edge-wise direction. To protect the rotor blade from failure due to extreme loads in the flap-wise direction, a load carrying girder is placed inside the turbine blade. They restrain the cross section against transverse deformation and the panels against buckling. To protect the rotor blade from failing due to the edge-wise loads the leading edge and the trailing edge are strengthened, mainly by adding more material. To prevent failure due to buckling, sandwich structures are used. Sandwich concepts are primarily used in the shear webs, trailing edge panels and leading edge panels. The rotor blades are also designed to be very flexible. The turbine blades are manufactured from composite materials consisting of layers and laminates which have various length scales. The failure mechanisms at each length scales must be known before designing a rotor blade. The wind turbine blade is designed by taking both the aerodynamic and the structural requirements into consideration [7]. The root of the turbine blade is circular and very thick so that it can withstand the high loads. The root of the rotor blade is fixed to the hub of the turbine. The span of the rotor blade is designed to be thinner so that it meets the aerodynamic requirements. The lift force generated when wind flows over the airfoil structure helps to rotate the wind turbine blade. Lift force is perpendicular to the rel-

ative velocity. The performance of the wind turbine increases with the increase in the ratio of lift force to drag force [8]. The angle at which the wind is incident on the turbine blade when the performance is maximum is called the optimum angle of attack. The wind turbine blade must be therefore designed in such a way that the wind hit the blade at the optimum angle of attack. The rotor blade velocity is not constant and it increases from root to tip. A continuous twist is given to the rotor blade from root to tip in order to counteract the change in the relative velocity. The wind turbine blades are also capable of rotating about its own axis (also known as pitching) in order to achieve optimum angle of attack with varying wind condition. Power extracted by the wind turbine is proportional to the square of the length of the rotor blade[9]. But with increase in turbine blade length deflection of blade tip due to axial wind force also increases. It is not possible to increase the wind turbine blade length beyond a limit because the wind turbine produces noise when the tip velocity increases beyond a limit[10]. Another problem with long turbine blades are, they require huge mechanical structures for installations which leads to heavy investments. The power output can be increased by increasing the wind turbine blade size because the power rating of a wind turbine is proportional to the swept area of the rotor [11]. Thus, even small increase in the blade length can greatly increase the power output. However, large rotors lead to new technical challenges: For example, the output of a wind turbine increases with the second power of the rotor blade length, while the mass of a rotor blade increases with the third power of its length. The result is an imbalance between load and power increase. In addition, large rotors are exposed to higher local turbulence, which causes higher local and global loads in the rotor blades.

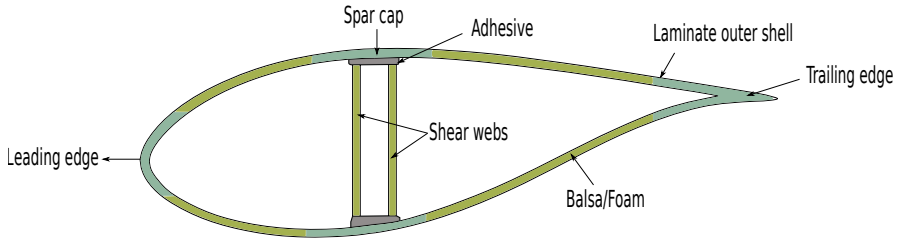

Figure 2.1: Example of an airfoil cross section of a wind turbine blade with two shear webs.

2.2 Materials for wind turbine blades

Most of the structural elements of the wind turbine blades are made of glass fiber reinforced plastics [12]. Typically, the glass/epoxy composites for wind blades contain up to 75 weight percentage glass [13]. The layers are made of bi-axial, tri-axial, or unidirectional layups (depended on the structural element). Layers are in-homogeneous and an-isotropic. To avoid buckling of large areas, sandwich stiffened designs are used. Sandwich has the core materials as balsa wood or polymeric foam which are glued with epoxy adhesives. Balsa and adhesives are isotropic. The material law is Hook's law and it is a linear elastic model [14].

2.3 SmartBlades

Wind turbine rotor blades are subjected to severely fluctuating wind loads. The result is high loads for the rotor blade material and an enormous challenge when it comes to the control system. To overcome the effects of gust and fatigue loads, a new concept for intelligent rotor blades which are capable of adapting themselves to varying load conditions was developed as a collaborative effort of the German Aerospace Center and the Fraunhofer Institute for Wind Energy Systems . A technique called Bend-Twist coupling is used in this concept where when the blade is deflected it also twists. This helps in load alleviation i.e., reduce the aerodynamic angle of attack, hence reducing aerodynamic loading. In order to achieve Bend-Twist coupling, we have to step away from the traditional quasi-isotropic laminates and fiber angles breaking some traditional design rules.

Figure 2.2: Picture of a SmartBlade developed by DLR and Fraunhofer IWES

2.4 Full scale blade testing

Full-scale blade testing is a technique for validating the performance of wind turbine blades and therefore it is an obligatory requirement for certification of wind turbine blades [15]. The purpose of the full scale tests is to verify that the specified limit states are not reached and that the type of blade in question bears the estimated strength and life span. Therefore, it allows an insight into the failure mechanisms of the rotor blades [16].
According to **DNVGL-ST-0376** standard, a full scale blade test comprises the following tests [17]:

- Mass, stiffness distribution and eigen frequency tests
- Static tests
- Fatigue tests
- Post fatigue static tests

All the tests are performed in a flap-wise and edge-wise directions. These tests are carried out to obtain two sets of information. One, the ability to withstand the loads for which the rotor blade has been designed. Two, to obtain the properties of the rotor blade like strains and deflections arising

from the applied loads. An overview about a few test studies made so far has been discussed below.

A full scale testing of a 45.7 m wind turbine blade was performed to examine the effect of crack propagation on the turbine blade's performance[18]. The fatigue results showed that, for a 200 mm crack between the web and spar cap at 9 m from the blade root, the crack did not propagate at 50% of the target bending moment up to 62,110 cycles. But when the load was increased to 70% of target bending moment, some damages were noticed at the pressure side of the blade. Next, the 200 mm crack was increased to 1000 mm. The crack began to propagate only after the applied load exceeded 100% of target bending moment. The failures that were recorded were adhesive joint failure, compression failure and sandwich core failure.

A 34 m wind turbine blade was tested in edgewise direction for 80% of maximum loads[19]. The blade was reinforced according to a Risø DTU invention, where the trailing edge panels are coupled. The coupling is implemented to prevent the out of plane deformations and to reduce peeling stresses in the adhesive joints. The test was repeated before and after a maintenance hole in the web was reinforced. This reinforcement reflected on the measurement results. Test results with and without the reinforcement implemented were compared. It showed that the maximum amplitude of the trailing edge panel deformation was reduced by approximately 20%. However, at the same time the area of the deformation increased. The measurements indicating the deformation of the box girder showed increase of the distortion behavior when implementing the reinforcement. The DIC (advanced 3D optical measuring system) measurements presenting the displacement field of the panel indicate that there is a double wave. This behavior was also revealed by the displacement measurements. The DIC results also confirm that the displacement of the middle points of the panels is reduced when the blade is reinforced.

Kong et al. proposed a structural design for developing a wind turbine blade made of E-glass/epoxy for a 750 kW class horizontal axis wind turbine system[20]. A prototype was manufactured and a full-scale static structural test was carried out. The experimental results showed that the designed blade was stable. The predicted properties like mass, center of gravity, blade tip deflection and first flap-wise eigen frequency agreed well with the corresponding measured values with 4% error. Furthermore, the measured strain results had good agreement with the analytic results.

A comprehensive review of full scale blade testing, including static and

fatigue testing is discussed in this paper [15]. In the present work, the Smartblade 2 was subjected to full scale blade testing which includes static tests, mass distribution and natural frequency tests and fatigue tests. This is the first bend-twist tested rotor blade.

Static testing

The behavior of the wind turbine blade under static loading is monitored in the static tests. The loads are applied using hydraulic cylinders and a pulley system. The cylinders are connected to a series of load frames mounted on the turbine blade (Source: Fraunhofer IWES). Each load frame is custom designed and built for the specific cross-section of the blade being tested. The tests are performed perpendicular to the floor of the test hall. The applied loads are dependent on the size of the rotor blade . The tests are monitored with the aid of a number of measuring signals, in combination with an optical measurement system that can record three-dimensional deflection of the blade[21]. The measurement frequency depends on the system used.

2.5 Finite element method theoretical insight

To model the wind turbine blade and it's thick adhesive layers both solid and layered shell elements are used. The caps are modeled using thick shell formulation taking shear deformation into account. The elements are located at the mid thickness of the caps, and shell offsets are not needed. The shear webs are modeled using a combination of shell and solid elements [22]. The reinforcement of the webs consists of adhesives and they are modeled with solid elements. Local masses are modeled as point masses like mass element MASS21.

2.5.1 Solid quadratic element

Quadratic elements are used, because they are more robust against distortion. They also show a good compromise between higher order finite elements and a dense low order mesh. This is advantageous in the adhesive layers of the blade. In Ansys, SOLID186 element is commonly used to model the adhesives refer Figure 2.3. It is a hexahedral 20 noded solid element that exhibits quadratic displacement behavior. The downside of the solid element is that the processing time is huge.

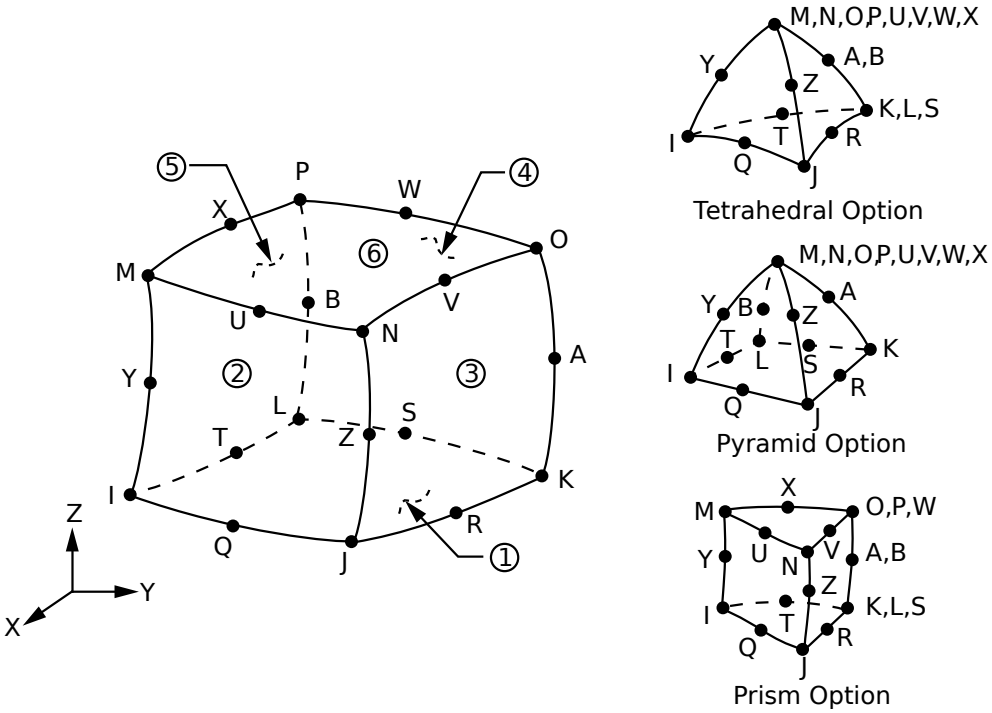

Figure 2.3: SOLID186 - 3-D 20-Node homogeneous Structural Solid

2.5.2 Shell element

Shells are solids of special shape(Hollow solids). For thin shells (like thin beams) the stress in the direction perpendicular to the shell surface is negligible. In Finite Element Analysis [FEA] shell elements can be utilized for effective results. It can lead to huge computational time savings since they allow modeling of thin features with fewer mesh elements. They are less prone to negative Jacobian errors which might occur when using extremely thin solid features. SHELL281 is used to model the composite layups and the spar of the rotor blade as it supports modeling of composite and sandwich constructs. It has 8-nodes with six degree of freedom at each node, three translations and three rotations. The element also supports degeneration into a triangular form. SHELL281 formulation incorporates for initial curvature effects refer Figure 2.5. Data can be retrieved for each layer of the shell. Once the output has been written to the result file, the LAYER command can be used to specify the element layer for which the data has to be retrieved. By default the entire element is considered to be one layer and the data that is retrieved is the top of the top layer and bottom of the bottom layer. Furthermore, the SHELL command can be used to specify the location within a

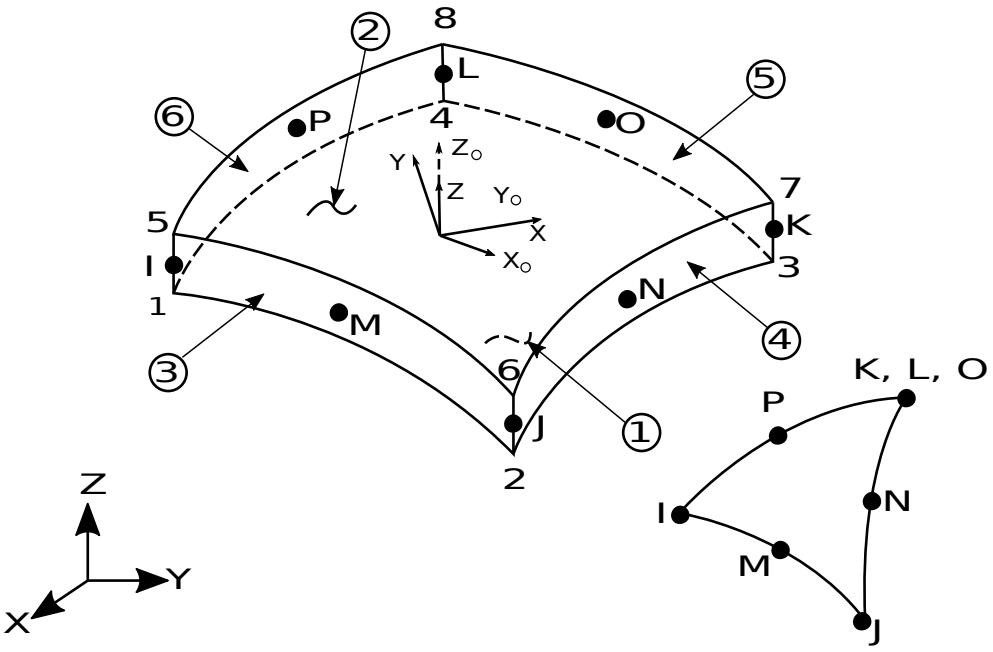

Figure 2.4: SHELL281 - 8-Node Shell

layer (or element i.e. if the layer command is set/left default) for output i.e. top, mid or bottom of layer. By default ANSYS averages the values of top and bottom surface and displays the results. The layer command can be used to overwrite the default and display or print results for various locations within a layer. Note that while using the LAYER command with SHELL281, KEYOPT (8) must be set to 2 in order to store results for all layers.

2.6 MASS 21 - Structural Mass

MASS21 is a zero mass point element having up to six degrees of freedom: translations in the nodal x, y, and z directions and rotations about the nodal x, y, and z axes. This point mass can be used as a point of load application. Concerning the output from the element, the nodal displacements are included as a default nodal solution data. From the elemental solution only the reaction forces and energies could be requested as an output. In a static analysis the MASS21 element has no effect if there is no rotation or no acceleration or inertial relief is not turned on (IRLF command).
In ANSYS APDL, various commands could be used to develop constraint equations like CE, RBE3, CERIG. The constraint equations developed using commands mentioned above are for component based analysis only and

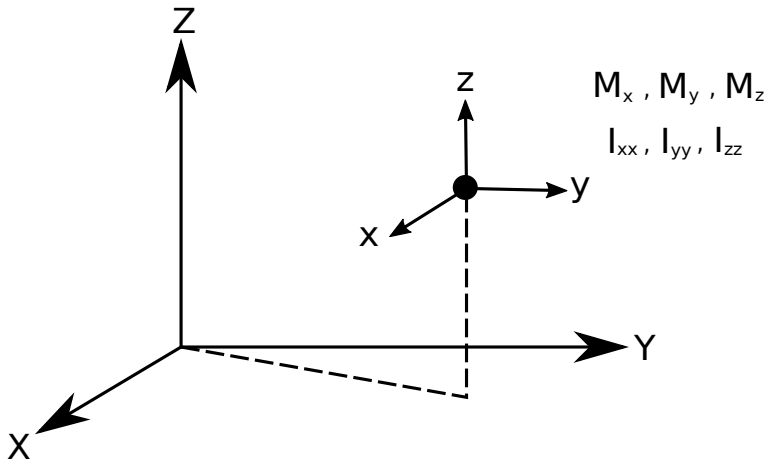

Figure 2.5: MASS21 Structural point Mass

do not work for assemblies in which contact based constraint equations are to be developed. The CERIG command develops rigid links, by connecting nodes (masters and slaves), offering one to six degree of freedoms (translational and rotational). The master node controls the behavior of the slave nodes. Any translation, rotation, forces and moment enforced onto the master node is transferred to the slaves. Rotation and moments take into account the distance between the master and the slaves.
An extensive research on FE model of wind rotor blades where deflections, strains and eigen frequencies are found, see ref. [20][23]

3
Experimental description

3.1 Experimental setup

3.1.1 Preliminary note

The static tests were performed for the 20-meter long rotor blade Smartblades 2. All the tests were conducted in the 90 m test hall of Fraunhofer IWES in Bremerhaven, Germany from January 23 to February 06 2018. The test description is based on the technical report of Bernd Haller from Fraunhofer IWES [4].

3.1.2 Initial setup

The first step was to calculate the blade's mass and center of gravity. The blade was lifted to calculate the weight. The weight of the transport structures, loading chains and shackles were subtracted. The mass of the blade was found to be 1800 kg.
The center of gravity was found out by adding the moments with respect to the center of the blade root. It was calculated in the direction along the span and chord of the blade. The center of gravity was found to be at 6.58 m ±0.2 m from the root and at 0.1 m±0.04 m in the y-direction.
Draw wire sensors were used to measure the vertical displacements at the load frames and at the tip. For the flap-wise bending, the sensors were placed one at the leading edge and one at the trailing edge. For the edgewise bending, the sensors were placed one at the suction side and one at the pressure side in line with the shear center of the cross section. In addition to the draw wire displacement sensors an optical displacement measurement measurement sensor was used to measure the three dimensional deformation of the blade.

The strain gauges were used to measure strains at various locations of the blade along the span as shown in Figure 3.1. For the positions R = 5000 mm and R = 8000 mm the profile is strongly instrumented to be able to capture the accurate deformation of the profiles. The relative measurement error made by these sensors are ±2%. The absolute error was determined analyzing the zero load time signal. The absolute error was found to be ±2μ m/m.

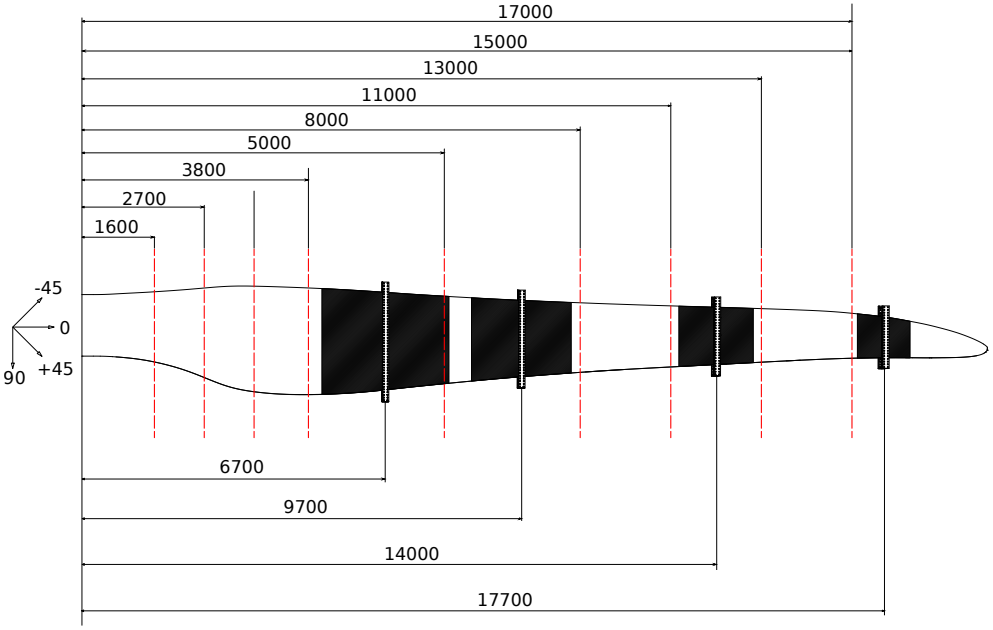

Figure 3.1: Positions of strain gauges and load frames (Distances in mm)

Load cells were used to measure the applied load at each load frame. Climate sensors were used to measure the temperature and humidity inside the test hall at regular intervals. The temperature inside and outside the blade was also measured using these climate sensors. The twisting of the blade root and the rotation of the load frames were measured using angle measurement sensors.

3.2 Bending stiffness tests

3.2.1 Introduction

The Smartblades 2 rotor blade was subjected to flap-wise and edgewise bending tests. The four bending tests were named as:

- MXMAX: Leading edge under compression
- MXMIN: Trailing edge under compression
- MYMAX: Suction side under compression
- MYMIN: Pressure side under compression

3.2.2 Testing Procedure

The basic testing procedure was the same for each loading case. The rotor blade was mounted to the test bench at an angle of 7.5° to the ground. Loads were applied with the help of hydraulic cylinders. The applied loads were measured using load cells which are attached to the load frames. In addition to the load cells, draw wire displacement sensors (DWS) are connected to the blade which measure the vertical displacements and the strain gauges measure the normal strains. The load frame positions and the sensors on the blade is referenced to the blade coordinate system where x-axis runs parallel to the ground from the blade root to the tip, y-axis runs left watching from root to tip and z-axis runs vertical with the origin at the center of the root. The general test set up is shown in Figure 3.2

Figure 3.2: Configuration example of a static loading rotor blade test performed by Fraunhofer IWES in Bremerhaven - Source: report of Bernd Haller [4]

3.2.3 Blade orientations during the static bending tests

The blade is initially oriented with the trailing edge facing up, leading facing down, suction side left and the pressure side right. This orientation is considered as 0°. For the load case Mxmax, the blade was oriented in the original position 0°, cf. Figure 3.3a. The blade was loaded at the first and the fourth load frame.
For the load case Mxmin, the blade was rotated to an angle of 180° with the leading edge facing upwards, cf. Figure 3.3b. For this load case, the blade was loaded at the outer 3 load frames.
For the load case Mymax, the blade was rotated to an angle of 90° with the pressure side facing upwards, cf. Figure 3.4a. The blade was loaded at the load frames 2, 3 and 4.
For the load case Mymin, the blade was rotated to an angle of 270° with the suction side facing upwards, cf. Figure 3.4b. The blade was loaded on the outer three load frames for both these load cases.

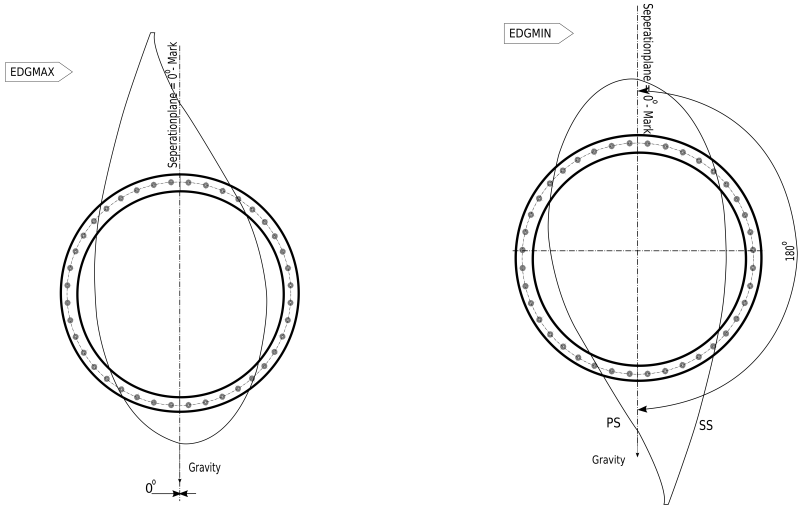

(a) Blade orientation during load case Mxmax

(b) Blade orientation during load case Mxmin

Figure 3.3: Blade orientation Mx load cases.

3.3 Strain Rosette for Strain Measurement

Strain gauges are used to measure strains at various locations in the test specimen. At each of the positions strain gauges for ε_{0° measurement were

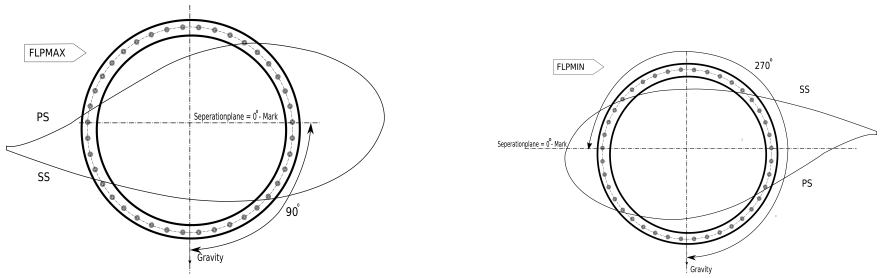

(a) Blade orientation during load case Mymax and torsion tests

(b) Blade orientation during load case Mymin

Figure 3.4: Blade orientation My and torsion load cases.

placed at both belts, the leading and trailing edge. For three positions (1600 mm, 8000 mm and 15000 mm) the spars were instrumented. The strain components $\varepsilon_{0°}$, $\varepsilon_{90°}$ and $\varepsilon_{\pm 45°}$ were measured. At two position (5000 mm and 8000 mm) multiple strain gauges were placed around the profile. For these sensors the strain components $\varepsilon_{0°}$, $\varepsilon_{90°}$ and $\varepsilon_{\pm 45°}$ were measured. An overview about the sensor names and their position are given in Table B.1. To validate the simulated strains the components of a strain gauge rosette ε_a, ε_b and ε_c illustrated in Figure 3.5 [24] have to be transformed in the strain components ε_x, ε_x and ε_{xy}.

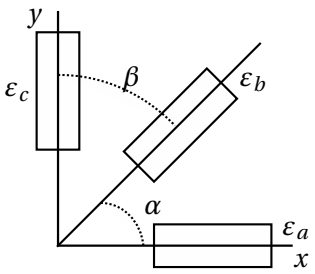

Figure 3.5: Definition of a strain gauge rosette.

For $\alpha = 45°$, $\beta = 45°$ and the engineering shear strain defined as $\gamma_{xy} = \varepsilon_{xy} + \varepsilon_{yx} = 2\varepsilon_{xy}$ we get

$$\begin{aligned} \varepsilon_{xx} &= \varepsilon_a \\ \varepsilon_{yy} &= \varepsilon_c \\ \varepsilon_{xy} &= \varepsilon_b - \frac{\varepsilon_a + \varepsilon_c}{2} \end{aligned} \tag{3.1}$$

3.3.1 Test execution

Quasi static loading was achieved by slowing increasing the loads in four load steps (i.e. 40%, 60%, 80% and 100%)

The loads, which have been used in the further validation for all the load cases are shown in Table 3.1.

Load point	Radius [m]	Mxmax[kN]	Mxmin [kN]	Mymax [kN]	Mymin [kN]
1	6.7	10.1	0.0	0.0	0.0
2	9.7	0.0	6.5	21.8	14.9
3	14.0	0.0	11.3	18.8	19.8
4	17.7	12.6	6.3	24	15.9

Table 3.1: Applied loads for all the bending load cases

3.4 Torsional stiffness tests

3.4.1 Introduction

The three torsion test were named as follows:

- Load case 1: Torsional stiffness test at load frame 2 (R = 9.7 m)
- Load case 2: Torsional stiffness test at load frame 3 (R = 14 m)
- Load case 3: Torsional stiffness test at load frame 4 (R = 17.7 m)

3.4.2 Test execution

The blade was oriented with the pressure side upwards just like the Mymax case for all the three load scenarios. The blade is mounted at a block angle of 7.5° and hence the torsional moment is not parallel to the pitch axis. Only one load frame was loaded with a pair of parallel forces pulling vertically up and down. The upper attachment was mounted at the shear center and the lower attachment at the end of the frame near the trailing edge as shown in Figure 3.6 **Note**:

- For the test LF2, due to a measurement mistake, the upper attachment was shifted 158 mm toward the leading edge.

Figure 3.6: Torsion test - Forces (represented by red arrows) - Figure taken from the report of Bernd Haller [4]

- For the test LF2, the load frame 1 was dismounted, for the test LF3, the load frames 1 and 2 were dismounted and for the test LF4, the load frames 1, 2 and 3 were dismounted to reduce stiffening effects.

The distance between the two draw wire sensors which are placed near the leading and trailing edges of the blade are given in Table 3.2. This distance can be used to find the twisting angles.

Radius [m]	Distance [mm]		
	Load case 1	Load case 2	Load case 3
6.7	2923	2923	2923
9.7	3178	2500	2500
14.0	2717	2717	2050
17.7	2375	2375	2375

Table 3.2: Distance between the draw wire sensors placed in the leading and trailing edges for all the torsion test scenarios

3.4.3 Load scenarios

The test scenarios with the applied loads is shown in Table 3.3

Scenario	Radius [m]	Torsional moment [kNm]
LF2	9.7	-45.0
LF3	14.0	-32.4
LF4	17.7	-27.0

Table 3.3: Applied loads for all the torsion load cases

4

Model description and validation

The structure mechanical model is based on the given design. It has been created as a finite element model. The aerodynamic hull was modeled first followed by the spar, spar caps and adhesive bonds. All sections, model segmentation and material definitions are created in finite element framework Abaqus. The final finite element mesh is translated to input data of finite element tool Ansys. In the following sections the model is explained in detail including the assumptions made and the material nomenclature.

4.1 Material and Layup

Three material classes are used to build the rotor blade. They are glass fiber reinforced plastics, foam material for the sandwich stiffened regions and an adhesive material to glue the parts of the blade. An additional pseudo material was created and assigned to specific regions for convenience. The material and their properties are given in Table 4.1 and their corresponding material numbers in the finite element models are given in Table 4.2.

Material	Orientation	E_1 [MPa]	E_2 [MPa]	G_{12} [MPa]	ν_{12} [-]	ρ [kg/m^3]	h [mm]
UD	0°	44151	14526	3699	0.3	1948	0.827
2AX45	±45°	11316	11316	11978	0.633	1875	0.625
2AX90	0°/90°	26430	27520	3464	0.124	1875	0.651
3AX	0°/±45°	29873	13377	6918	0.466	1875	0.922
3AX manual layup	0°/±45°	21888	9473	5126	0.46	1658	1.318
Balsa Baltek SB.100		35	35	105	0.3	291[1]	19.05
Foam Airex C70-55-20mm-spar		55	55	22	0.3	180[1]	20
Foam Airex C70-55-20mm		55	55	22	0.3	279[1]	20
Foam Airex C70-55-15mm		55	55	22	0.3	314[1]	15
Foam Airex C70-55-10mm		55	55	22	0.3	384[1]	10
Foam Airex C70-55-5mm		55	55	22	0.3	596[1]	5
ADH/HARDENER		4864	4864	1828	0.33	1160	-
Pseudo material		10	10	3.84	0.3	1.0E-5	0.1

Table 4.1: Material parameters based on [25]. 1-Values after matrix infusion

Material	Abaqus	Ansys	Nastran
UD	MAT_UD	7	7
2AX45	MAT_2AX-45_45	22	22
2AX90	MAT_2AX-0_90	24	24
3AX	MAT_3AX	18	18
3AX manual layup	MAT_3AX_HANDLAMINAT	4	4
Balsa Baltek SB.100	MAT_BALSA_SB100	12	12
Foam Airex C70-55-20mm-spar	MAT_SCHAUMSTEGAIREX_C70-55	32	32
Foam Airex C70-55-20mm	SCHAUM_AIREX_C70-55-20MM	37	37
Foam Airex C70-55-15mm	SCHAUM_AIREX_C70-55-15MM	25	25
Foam Airex C70-55-10mm	SCHAUM_AIREX_C70-55-10MM	19	19
Foam Airex C70-55-5mm	SCHAUM_AIREX_C70-55-5MM	13	13
ADH/HARDENER	ADH/HARDENER	23	23

Table 4.2: Material number in the finite element models

4.2 Finite element model

The wind turbine blade model was created in Abaqus and has been converted in Ansys. Thick adhesive joints are modeled with quadratic serendipity finite solid elements and the thin walled structures are modeled with quadratic serendipity finite shell elements. The layups were defined as stacking sequence. The material formulation is based on the classical laminate theory with all the assumptions [26]. The stacking directions are shown in Figure 4.1

The layers were homogenized. Fibers and matrix are not separated and the resulting homogeneous material has a transverse isotropic material symmetry. The balsa woods used as a sandwich core are part of the stacking sequence and have isotropic material symmetry. The bi-axial and tri-axial layups were defined as one thick layer with resulting homogenized parameters.

For easy usability components were defined.

4.3 Discrepancies to design

In this part we discuss about the assumptions and adaptations that were made to reduce the complexity of the model.

- The upper and lower shell stacking of the FE model have no sandwich free region next to the trailing edge. Figure 4.2 shows that for the up-

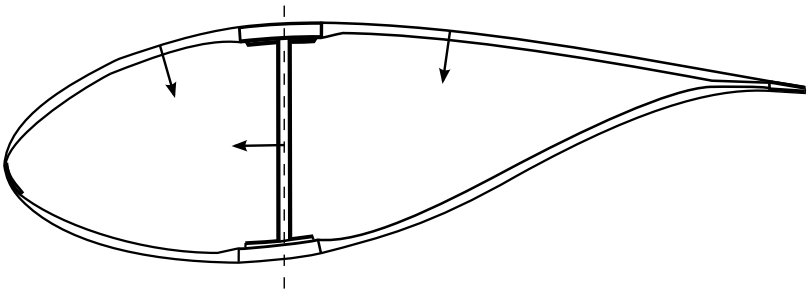

Figure 4.1: Reference planes of the finite shell elements and stacking direction

per part of the turbine. This lead to a higher local bending stiffness at the trailing edge. Analysis of trailing edged buckling load described by [5] will be overestimated. Also local strain measurements will be affected and the errors might be higher. Global effects won't be affected, because the tensile stiffness of the extra foam is very small.

- The tip of the blade was not modeled. The reason for this is the tip does not add additional stiffness to the blade. Due to its shape the meshing of the region is challenging and it adds more elements without adding additional information.
- The adhesive joints between the spar cap and the outer shell are also thicker due to the already described reasons. The thicker adhesives will change the mass distribution of the blade and increase the stiffness. Both are assumed to be small
- The adhesive joint at the leading edge has not been modeled. It is very thin and it's effects are assumed to be negligible.
- For production reasons the root has been build separately and was glued with the rest of the blade. This skew adhesive joint has not been modeled.
- Bolts have not been modeled.
- The adhesive joints are thicker in the model than in reality. The volume of the adhesive is modeled between the reference planes of the shell elements. The thickness of the adhesive is increased by the thickness of the local design layup, but not the modeled one. The reason is, that the aerodynamic shape, which is used as the reference surface for the finite shell elements are independent from the stacking sequence represented by these elements.

- There is overlap between the shell element and volume elements illustrated at a cross section Figure 4.3b

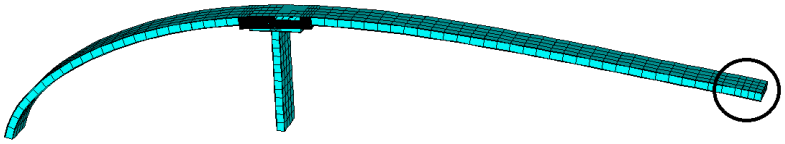

Figure 4.2: Upper shell of the wind turbine blade to illustrate assumptions made at the trailing edge (black circle).

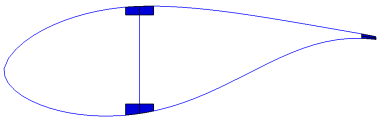

(a) Visualization of the shell and solid element distribution .

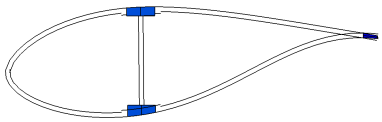

(b) Visualization of the virtual thickness of the shell elements

Figure 4.3: Visualization of the shell and solid element distribution in a cross section.

4.4 Boundary conditions

A very thick steal frame was used to fix the blade at the root. It was found out that the stiffness of the frame is very high in the direction perpendicular to the ground where as it is lower in the direction parallel to the ground comparatively. But this is relevant only for the eigen frequency tests but not the static tests. Therefore, a clamped boundary condition has been assumed. Since the blade is clamped to the test rig at the root, the nodes representing the root were constrained with zero degrees of freedom as shown in Figure 4.4

4.5 Load introduction

Loads are introduced on the blade using the load frames which are fixed to the blade. The mass distribution of the frame does not influence the test results as the sensors were calibrated taking the deformation of the blade due to the mass of the frame into account. Hence a reference node is created as a point mass with infinite stiff connections at all the positions where the loading frame is located. MASS21 element was assigned to this node. This master

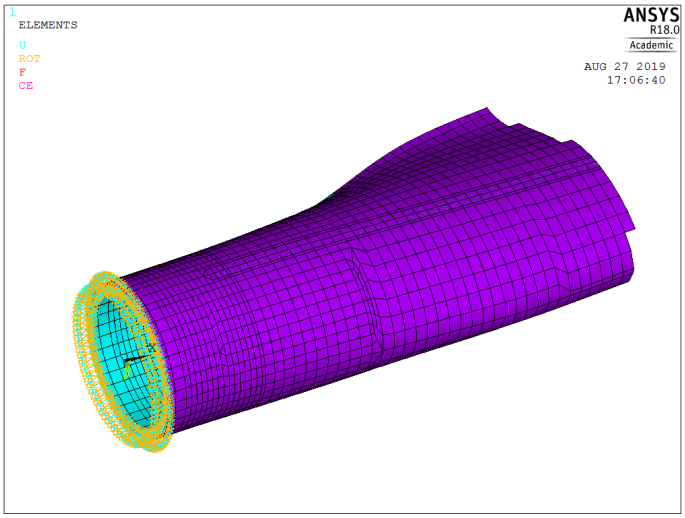

Figure 4.4: Boundary Condition

node was then connected to all the other nodes at the same radius through rigid links using the command CERIG. This is illustrated in Figure 4.5. The loads were applied using the **.mac** files which were called to the main script as input files. The effect of the skew boundary condition and the weight deformation of the blade can be tested by rotating the load vector. In that case the loads are applied in the deformed state coordinates. Since the blade is oriented at an angle of 7.5° to the ground, the load vector has been rotated to achieve this orientation.

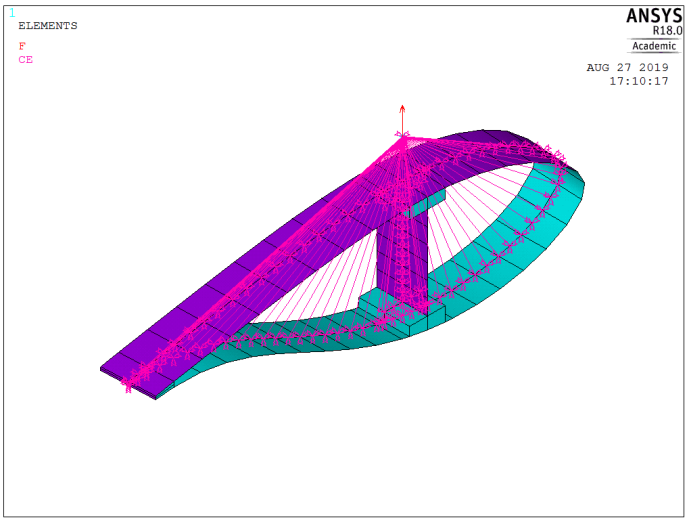

Figure 4.5: Load introduction

5
Results and discussions

5.1 Scenarios and variations

All experimental scenarios are given in Table 3.1 for the bending load cases and Table 3.3 for torsion load cases. All these experiments were modeled in Ansys Mechanical APDL.

Solver

All static analysis were performed with a linear solver.

5.2 Displacement

For all scenarios the displacement at four specific positions were measured at the leading and trailing edge. The positions are at R = 6700 mm, 9700 mm, 14000 mm and 17700 mm. The comparison between the simulation and the experiment at each position for the four bending load cases are shown in Figure 5.1 - 5.4. All results are in good agreement. But a considerable difference can be seen in the MyMax load case, especially at the leading edge. In the experiment, a significantly more pronounced bending-tosion coupling is found for this load case than in the simulation. This behavior cannot really be explained, because the other load case does not show such behavior.

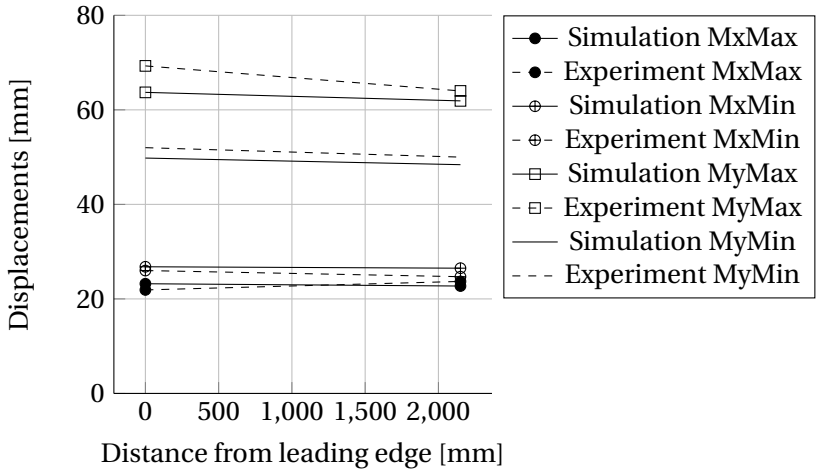

Figure 5.1: Displacements at position $R = 6700\,mm$ for all bending load cases.

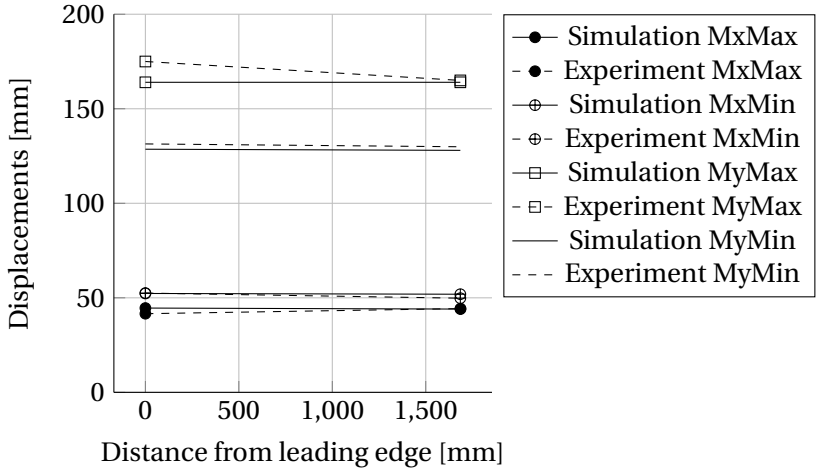

Figure 5.2: Displacements at position $R = 9700\,mm$ for all bending load cases.

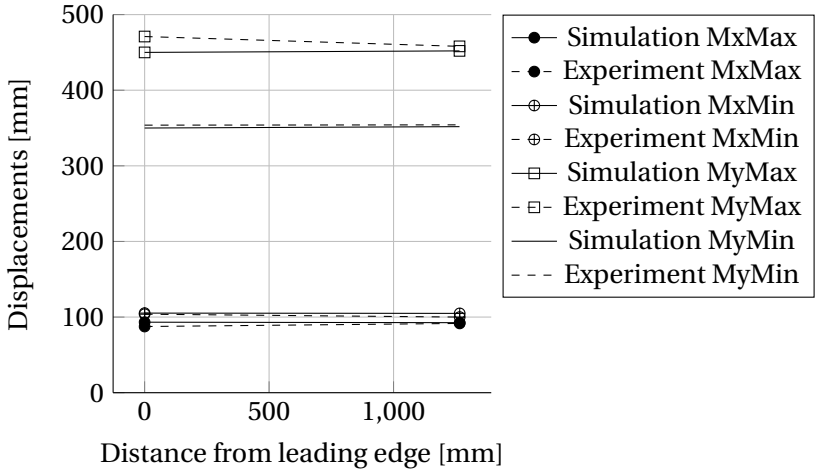

Figure 5.3: Displacements at position $R = 14000\,mm$ for all bending load cases.

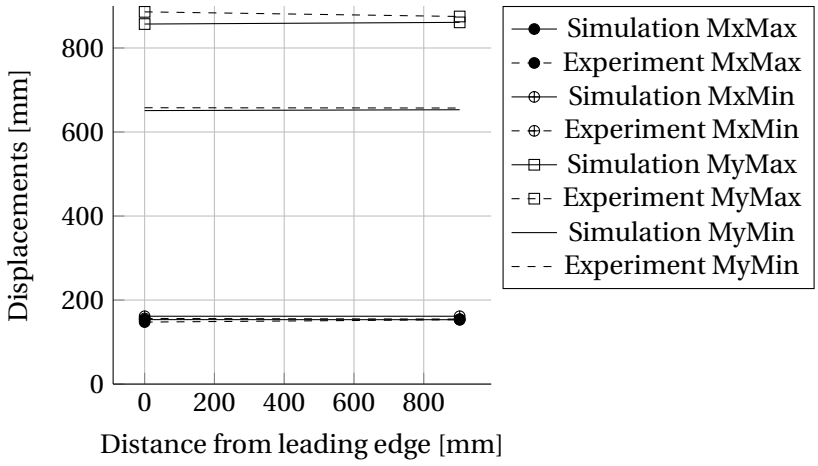

Figure 5.4: Displacements at position $R = 17700\,mm$ for all bending load cases.

5.3 Strain measurements

In Ansys APDL so called paths can be created to export the results for specific regions of interest. This tool is used to compare the strains between the experimental tests and the numerical model. The first paths are defined in radial direction at the belts of the pressure and suction side. The second path is defined starting from the leading edge and tracing along the airfoil cross section till the trailing edge. The paths are separately defined for the pressure side and the suction side at the radius which are instrumented with the strain gauges as shown in Figure 5.5.

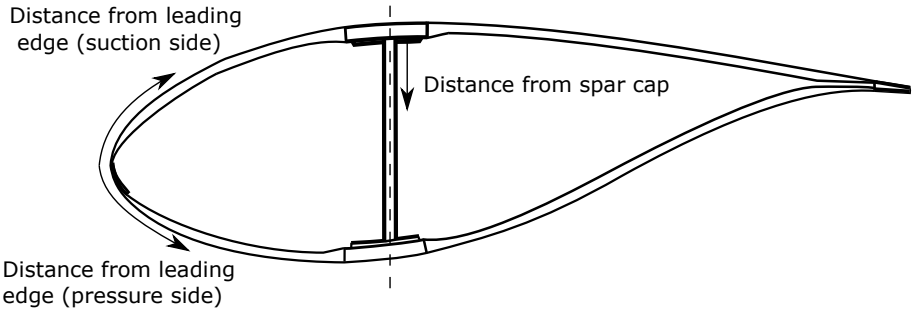

Figure 5.5: Definition of paths for comparing experimental and numerical results.

5.3.1 Mxmax results

The strain comparisons for the load case Mxmax (cf. Figure 3.3a) are shown in Figure 5.6a - Figure 5.18. Because of the orientation of the rotor blade it can be expected that the mechanical strains at leading and trailing edges are greater compared to the mechanical strains at the belt. Both the simulation and the experiment fulfill this expectation, cf. Figure 5.6 for the belts and Figure 5.7 - 5.18 for the leading and trailing edge.

The absolute deviations are small for most measuring positions. As expected, the relative deviations are higher in areas with small strains than in areas with larger strains. This behavior can be seen prominently in the suction side belts than the pressure side belt. The deviations of the strains are in the range of less than 20 $\mu\varepsilon_{xx}$. These are the absolute values for the pressure side. Therefore the deviations are relatively high. The suction side course matches well between simulation and experiment atleast till the mid way of the span and there is a perfect match towards the tip. In the case of

the pressure side, there are larger differences in the area near the root which is again difficult to explain.

The strongly instrumented profiles R = 5000 mm and R = 8000 mm are shown in Figure 5.10 - 5.14. Both the simulated ε_{xx} (cf. Figure 5.10a) and ε_{yy} (cf. Figure 5.11a) strain distribution and values at the suction side are in very good agreement with the experiment at R = 5000 mm. For the results of ε_{xx} at the pressure side (cf. Figure 5.10b) the strain distribution between 0 - 800 mm distance from the leading edge differs between experiment and simulation. It is not clear where this non-linearity comes from, when the suction side does not show such behavior. For ε_{yy} at the pressure side this distribution error does not occur. However, the strain between 1800 mm - 2200 mm are underestimated by the simulation (cf. Figure 5.11b).

For R = 8000mm the simulated ε_{xx} suction side (cf. Figure 5.12a) and pressure side (cf. Figure 5.12b) strain distribution and values are in very good agreement with the experiment. The simulated ε_{yy} strains for the suction side match also with experiments (cf. Figure 5.13a). For the pressure side the experiment shows a weak non-linear behaviour of the strain distribution, while the numerical results are nearly linear (cf. Figure 5.13b).

All measured values ε_{xx} for the profiles R = 1600 mm, 2700 mm, 11000 mm, 13000 mm, 15000 mm and 17000 mm are in good agreement with the simulation. In this profile only the leading and trailing edge were instrumented with strain gauges. Therefore, the profile strain distribution is unknown.

MxMax - belt

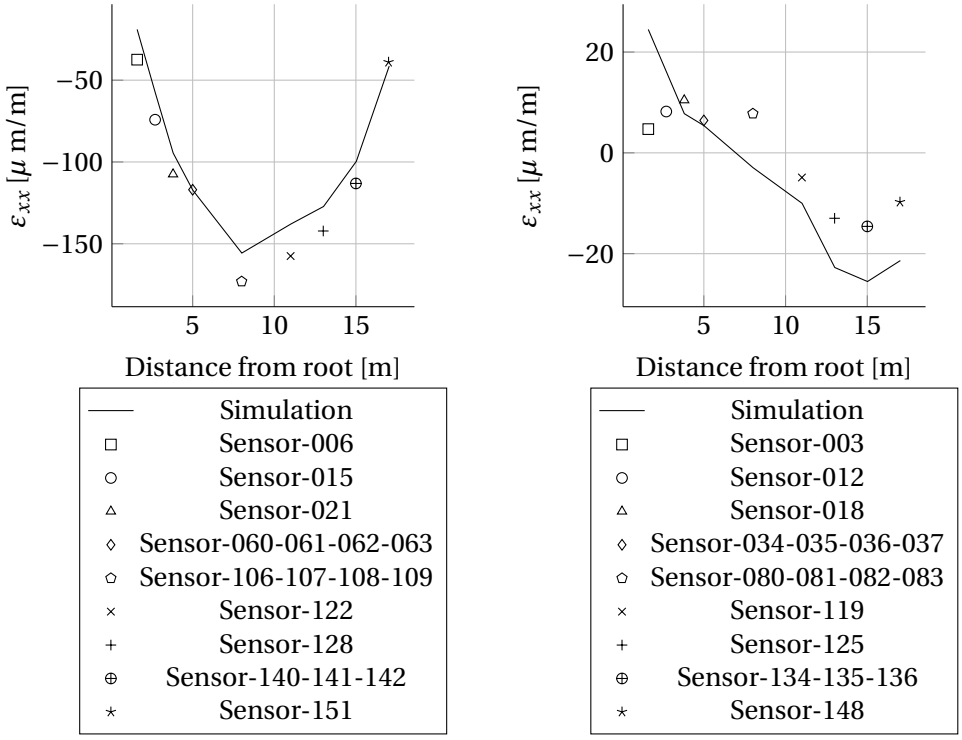

(a) Suction side belt.

(b) Pressure side belt.

Figure 5.6: Strain comparison ε_{xx} for Mxmax load case.

MxMax - Section wise

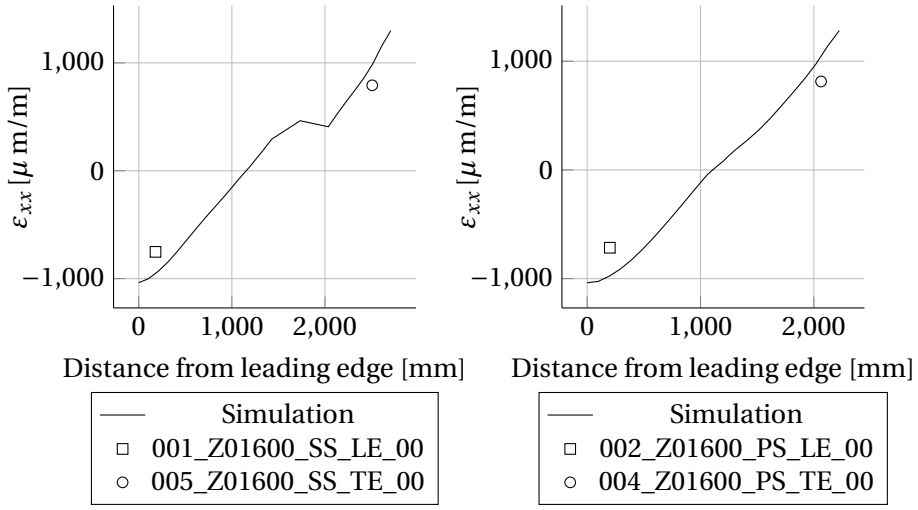

(a) Suction side.

(b) Pressure side.

Figure 5.7: Strain comparison ε_{xx} at radial position $R = 1600\ mm$ for Mxmax load case.

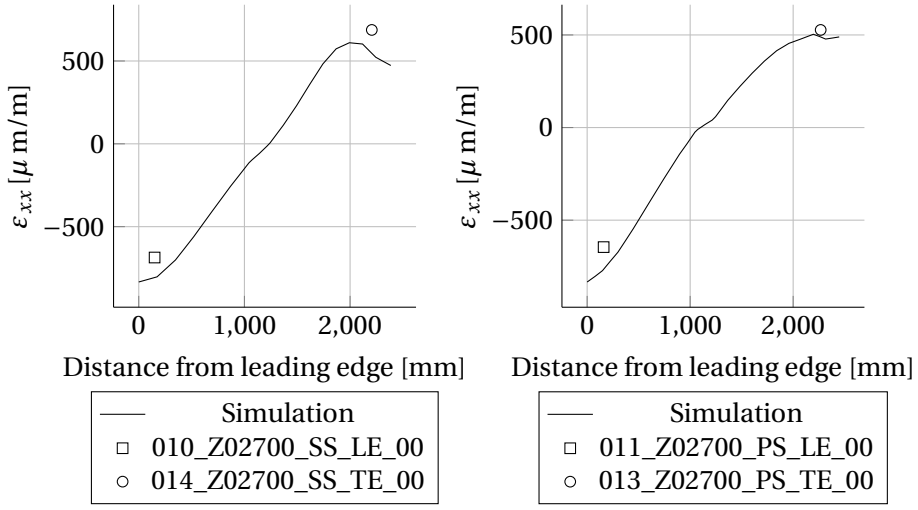

(a) Suction side.

(b) Pressure side.

Figure 5.8: Strain comparison ε_{xx} at radial position $R = 2700\ mm$ for Mxmax load case.

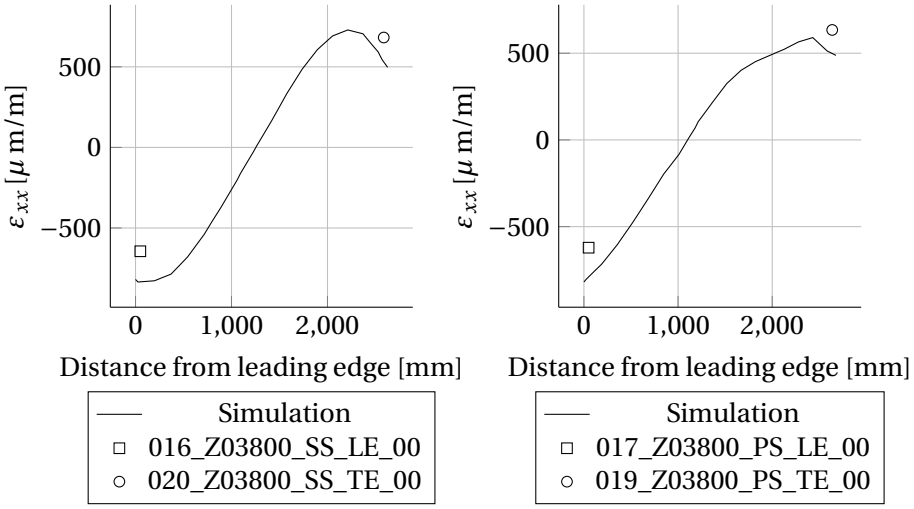

(a) Suction side.

(b) Pressure side.

Figure 5.9: Strain comparison ε_{xx} at radial position $R = 3800\ mm$ for Mxmax load case.

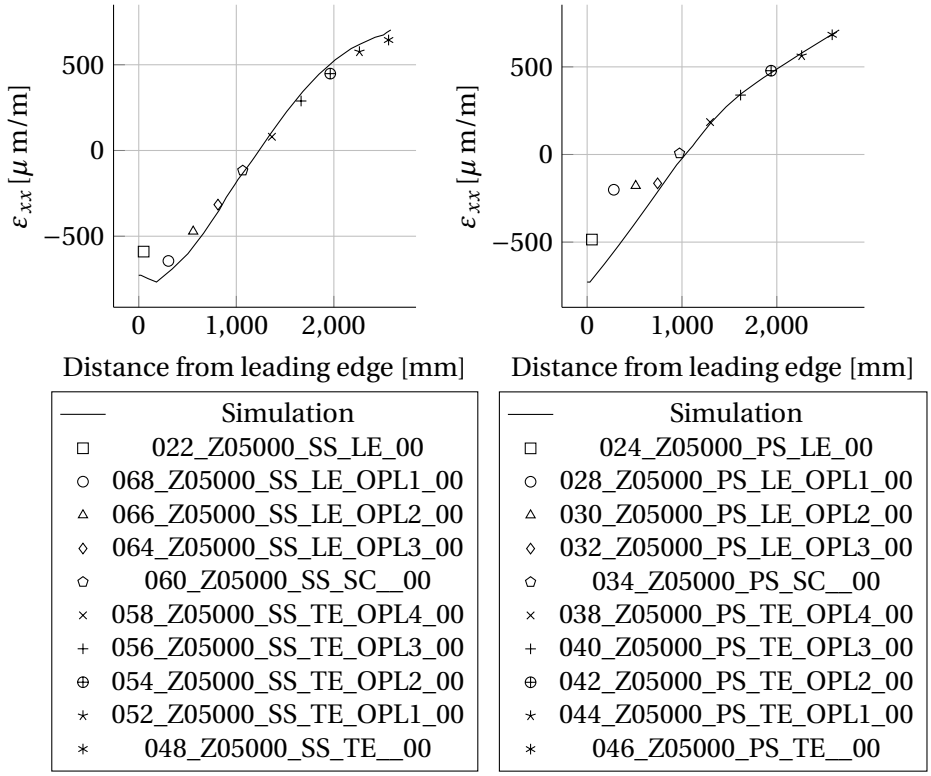

(a) Suction side.

(b) Pressure side.

Figure 5.10: Strain comparison ε_{xx} at radial position $R = 5000\ mm$ for Mxmax load case.

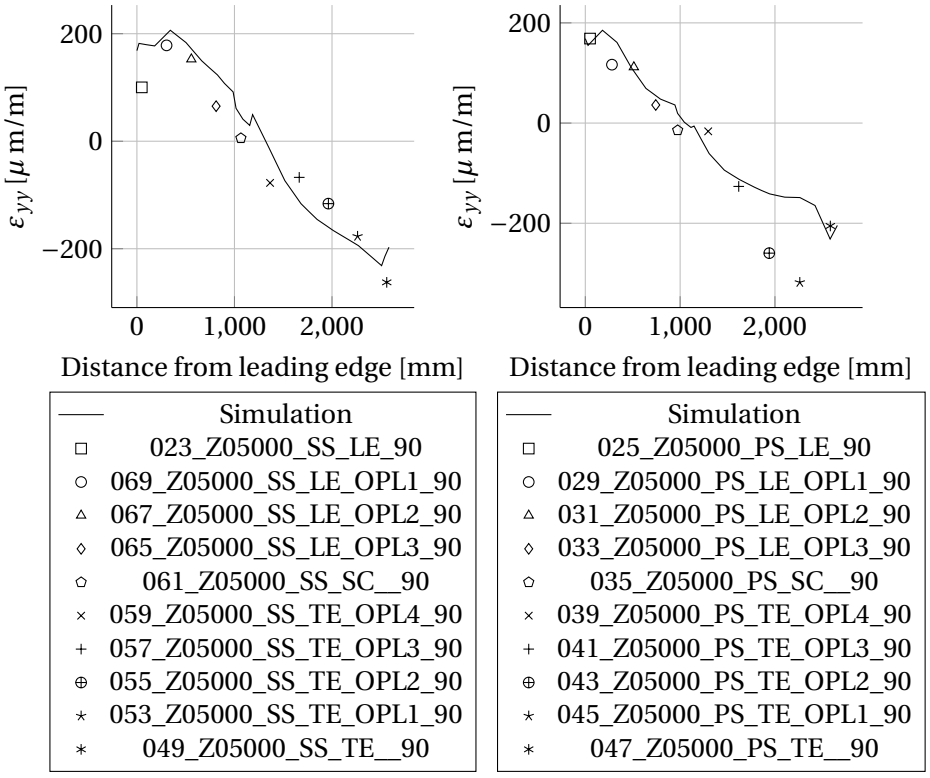

(a) Suction side.

(b) Pressure side.

Figure 5.11: Strain comparison ε_{yy} at radial position $R = 5000\ mm$ for Mxmax load case.

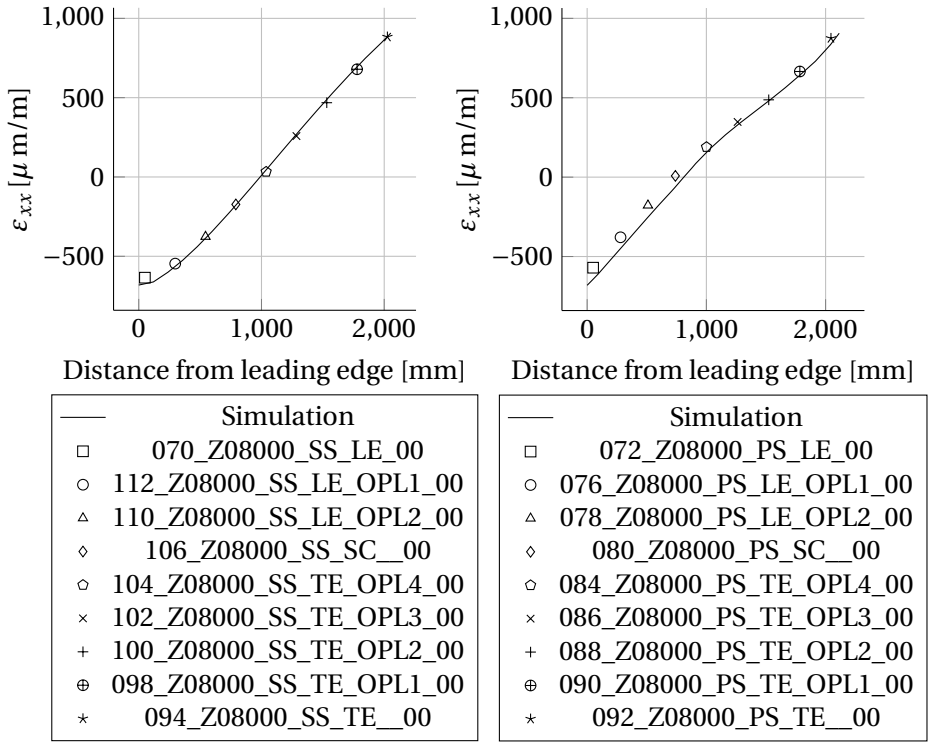

(a) Suction side.

(b) Pressure side.

Figure 5.12: Strain comparison ε_{xx} at radial position $R = 8000\ mm$ for Mxmax load case.

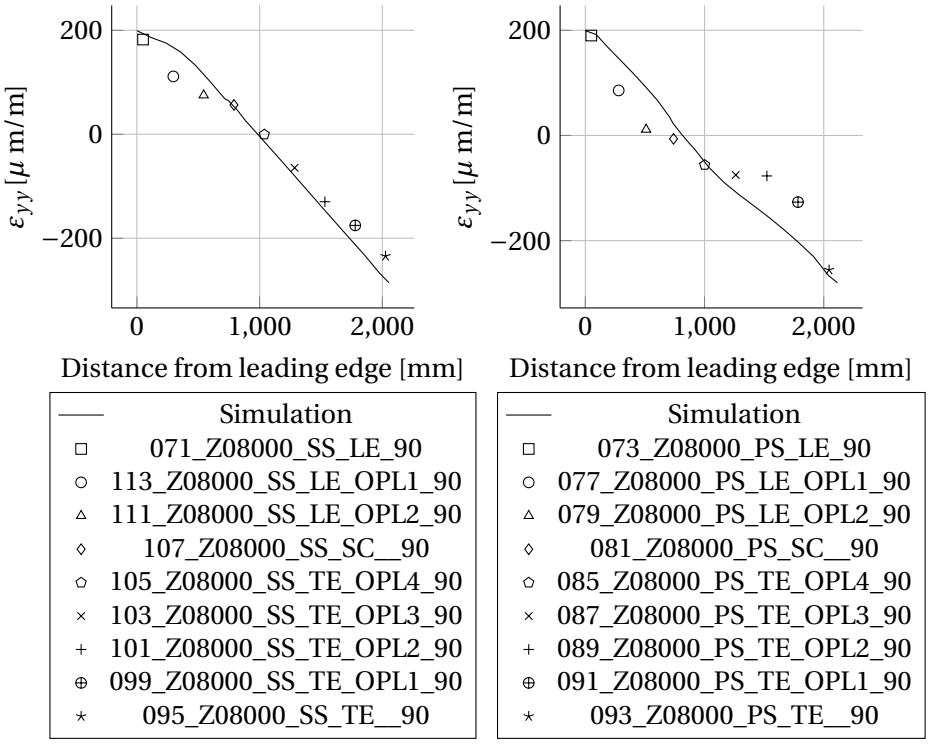

(a) Suction side.

(b) Pressure side.

Figure 5.14: Strain comparison ε_{yy} at radial position $R = 8000\ mm$ for Mxmax load case.

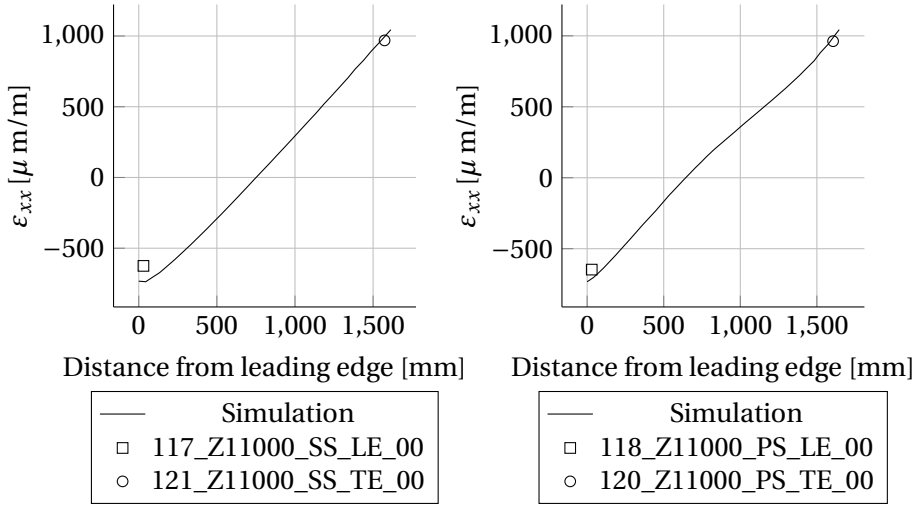

(a) Suction side.

(b) Pressure side.

Figure 5.15: Strain comparison ε_{xx} at radial position $R = 11000\ mm$ for Mxmax load case.

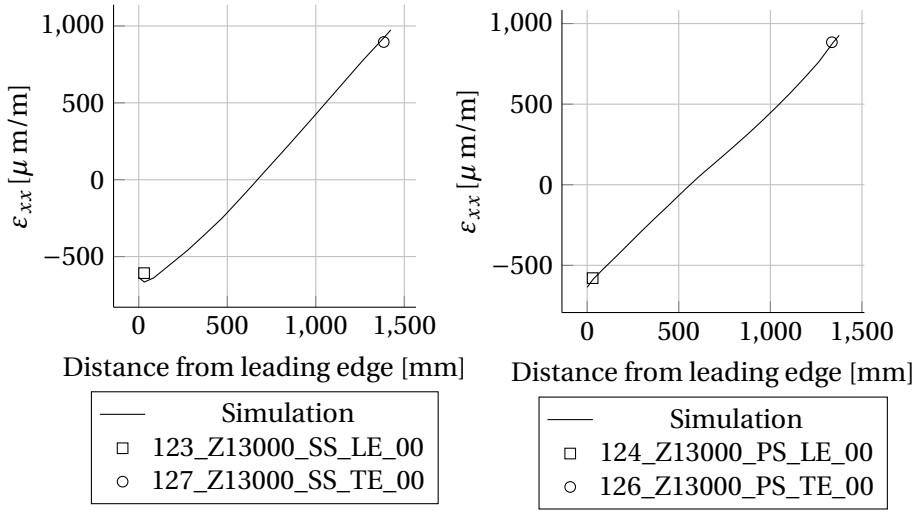

(a) Suction side.

(b) Pressure side.

Figure 5.16: Strain comparison ε_{xx} at radial position $R = 13000\ mm$ for Mxmax load case.

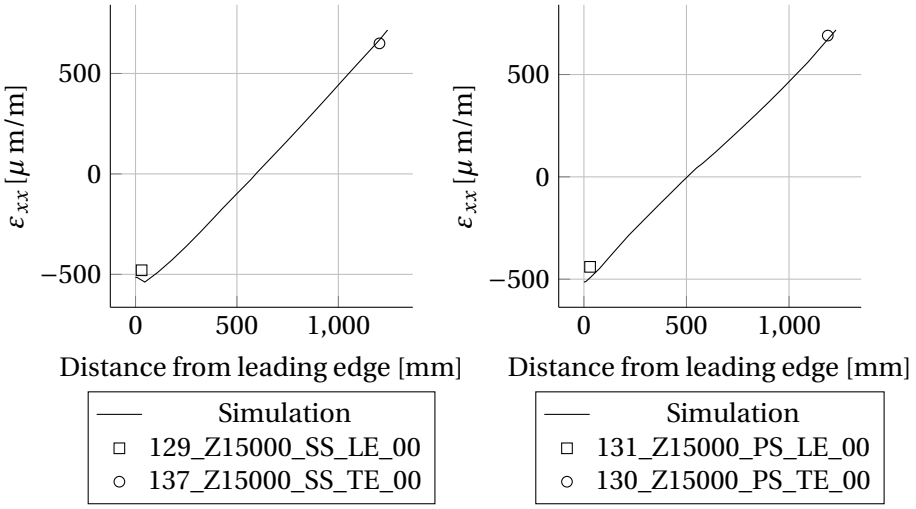

(a) Suction side.

(b) Pressure side.

Figure 5.17: Strain comparison ε_{xx} at radial position $R = 15000\ mm$ for Mxmax load case.

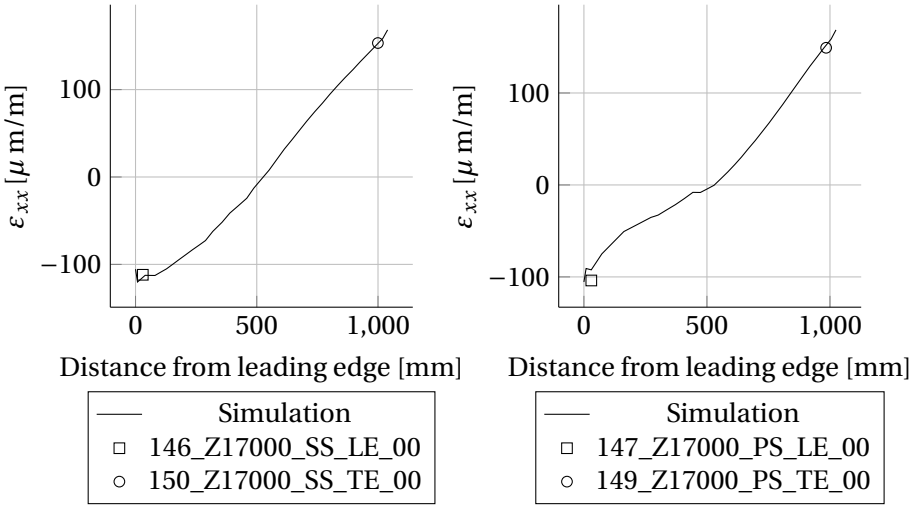

(a) Suction side.

(b) Pressure side.

Figure 5.18: Strain comparison ε_{xx} at radial position $R = 17000\ mm$ for Mxmax load case.

5.3.2 Mxmin results

The results for the load case Mxmin (cf. Figure 3.3b) are shown in Figure 5.19a - Figure 5.31. Due to the orientation of the rotor blade it can be expected that the mechanical strains at leading and trailing edge are greater compared to the belt strains. Both the simulation and the experiment fulfill this expectation, cf. Figure 5.19 for the belts and Figure 5.20 - 5.31 for the leading and trailing edge. Comparing the load cases Mxmax and Mxmin for the belts a switch in signs of the $\mu\varepsilon_{xx}$ strain values can be seen, cf. Figure 5.6a and Figure 5.19a. This is expected because the wind turbine blade was rotated by 180° between the two load cases.

Also for Mxmin the absolute deviations are small for most measuring positions. As expected, the relative deviations are higher in areas with small strains than in areas with larger strains. This behavior can be seen very well when comparing the suction side belt with the pressure side belt. The deviations of the strains are in the range of less than 20 $\mu\varepsilon_{xx}$.

The strongly instrumented profiles R = 5000 mm and R = 8000 mm are shown in Figure 5.23 - 5.27. Both the simulated ε_{xx} (cf. Figure 5.23a) and ε_{yy} (cf. Figure 5.24a) strain distribution and values at the suction side are in very good agreement with the experiment at R = 5000 mm. For the results of ε_{xx} at the pressure side (cf. Figure 5.23b) the strain distribution between 0 - 800 mm distance from the leading edge differs between experiment and simulation. The distribution is similar to the Mxmax load case, cf. Figure 5.10b except for the sign change. Also for the Mxmin load case it is not clear where this non-linear behavior comes from, if the suction side does not show such behavior. For ε_{yy} at the pressure side this distribution error does not occur. However, the strain between 1900 mm - 2200 mm are underestimated by the simulation (cf. Figure 5.24b) which is also seen in Mxmax load case.

For $R = 8000\,mm$ the simulated ε_{xx} suction side (cf. Figure 5.25a) and pressure side (cf. Figure 5.25b) strain distribution and values match very good with the experiment. As for the Mxmax load case the simulated ε_{yy} strains for the suction side are also in good agreement with the experimental results (cf. Figure 5.26a). For the pressure side the experiment shows a stronger non-linear behavior of the strain distribution compared to the Mxmax load case. The simulation shows a very weak non-linearity of the strain profile (cf. Figure 5.26b), which does not represent the measurements.

All measured values ε_{xx} for the profiles R = 1600 mm, 2700 mm, 11000 mm, 13000 mm, 15000 mm and 17000 mm are in good agreement with the simulation. In these profiles only the leading and trailing edge were instrumented with strain gauges. Therefore, the profile strain distribution is unknown.

MxMin - belt

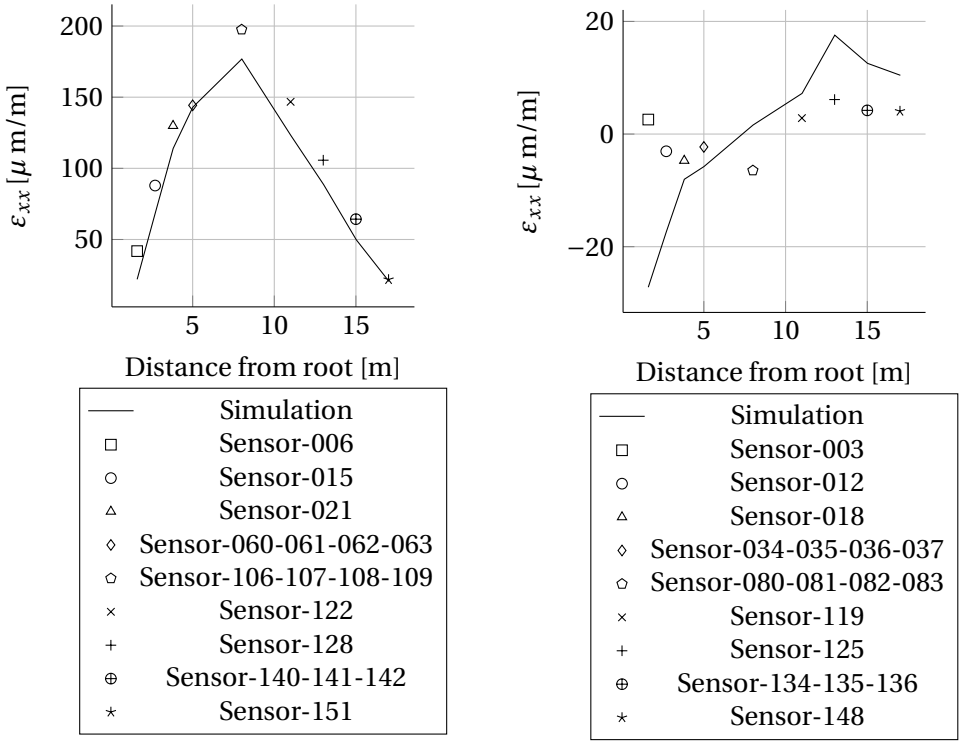

(a) Suction side belt.

(b) Pressure side belt.

Figure 5.19: Strain comparison ε_{xx} for Mxmin load case.

MxMin - Section wise

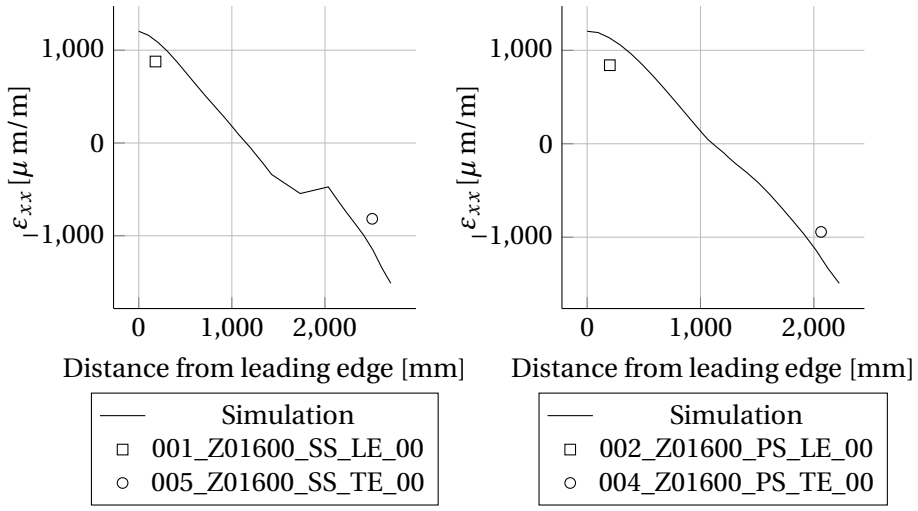

(a) Suction side.

(b) Pressure side.

Figure 5.20: Strain comparison ε_{xx} at radial position $R = 1600\ mm$ for Mxmin load case.

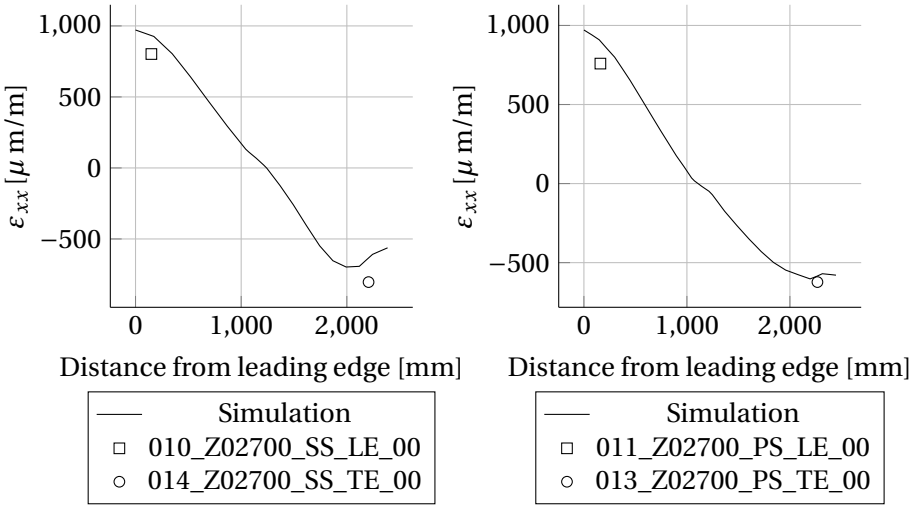

(a) Suction side.

(b) Pressure side.

Figure 5.21: Strain comparison ε_{xx} at radial position $R = 2700\ mm$ for Mxmin load case.

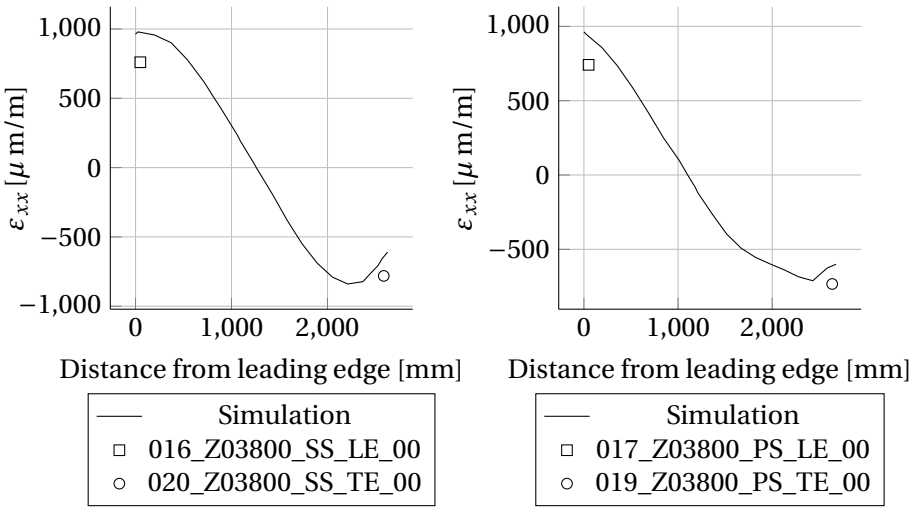

(a) Suction side.

(b) Pressure side.

Figure 5.22: Strain comparison ε_{xx} at radial position $R = 3800\ mm$ for Mxmin load case.

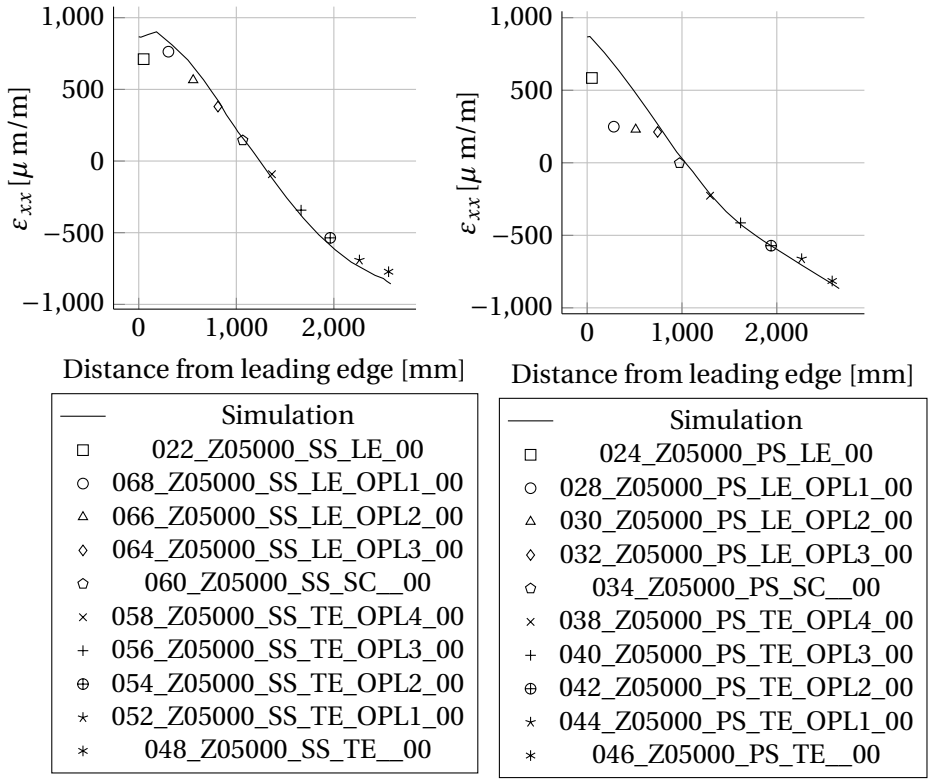

(a) Suction side.

(b) Pressure side.

Figure 5.23: Strain comparison ε_{xx} at radial position $R = 5000\ mm$ for Mxmin load case.

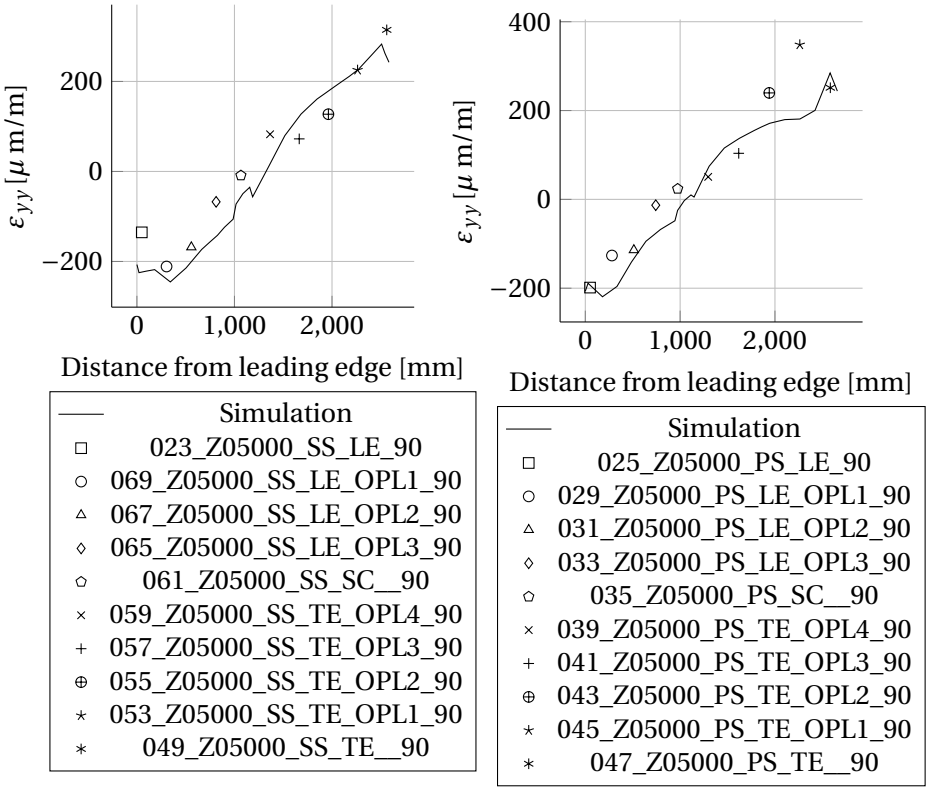

(a) Suction side.

(b) Pressure side.

Figure 5.24: Strain comparison ε_{yy} at radial position $R = 5000\ mm$ for Mxmin load case.

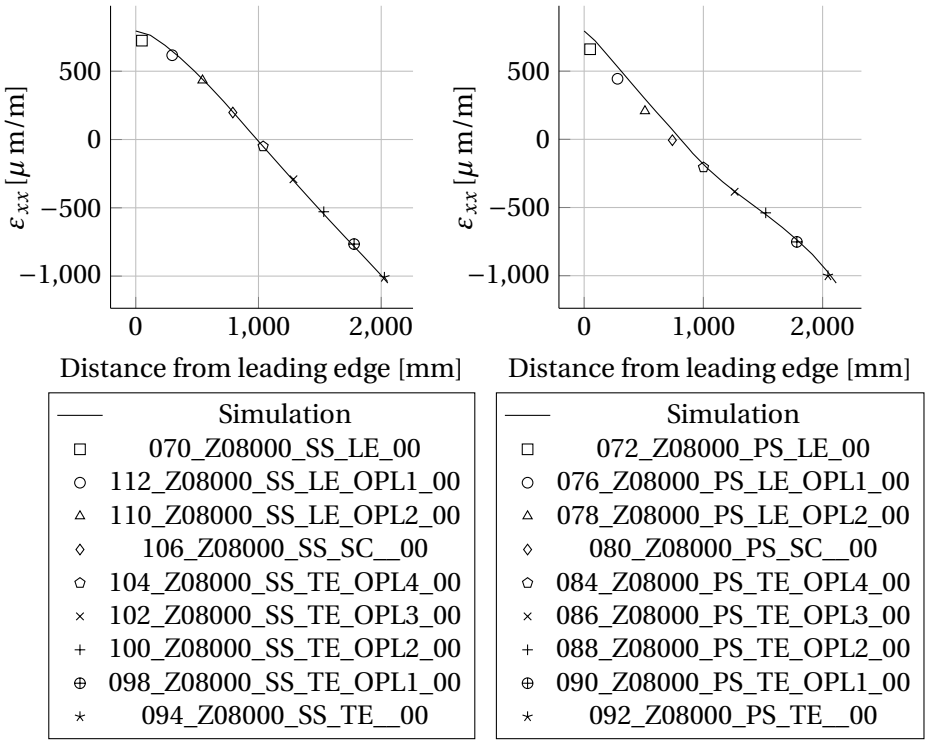

(a) Suction side.

(b) Pressure side.

Figure 5.25: Strain comparison ε_{xx} at radial position $R = 8000\ mm$ for Mxmin load case.

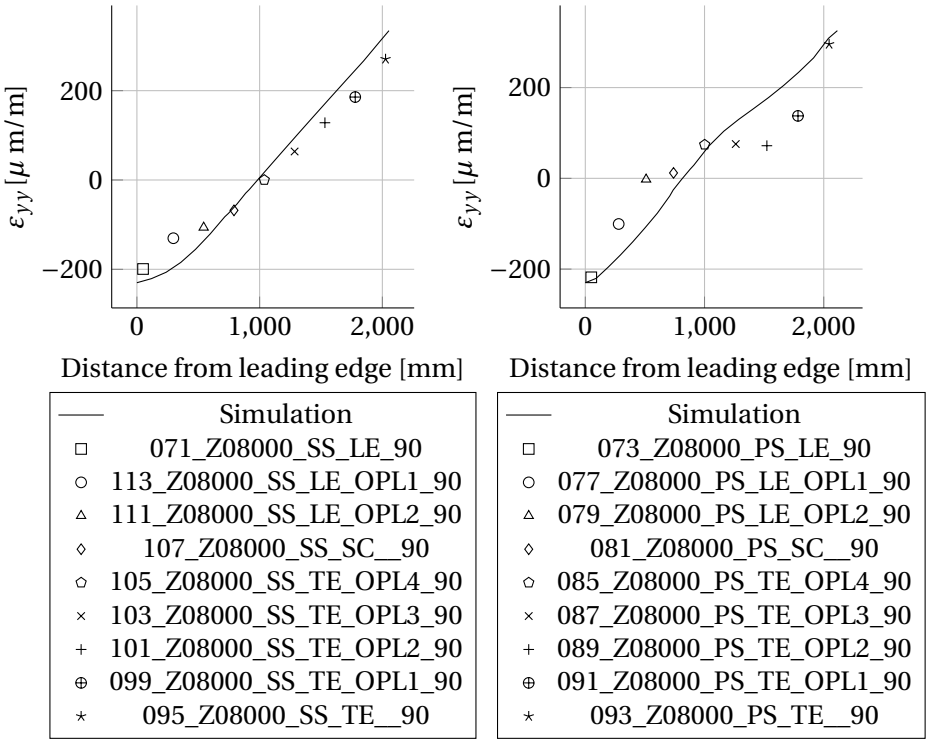

(a) Suction side.

(b) Pressure side.

Figure 5.27: Strain comparison ε_{yy} at radial position $R = 8000\ mm$ for Mxmin load case.

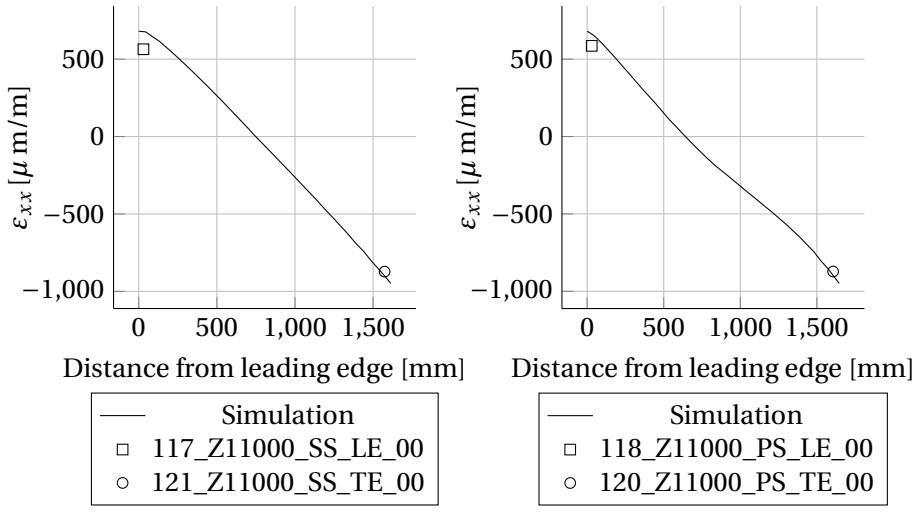

(a) Suction side.

(b) Pressure side.

Figure 5.28: Strain comparison ε_{xx} at radial position $R = 11000\ mm$ for Mxmin load case.

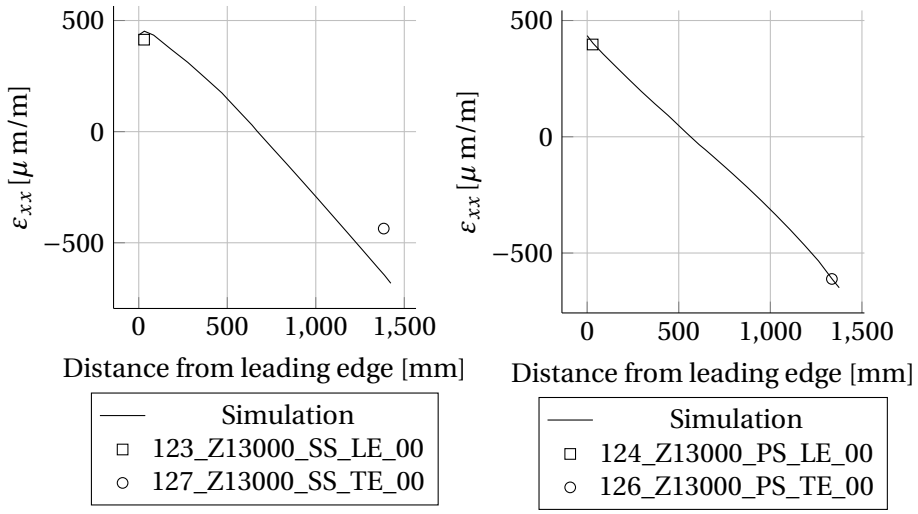

(a) Suction side.

(b) Pressure side.

Figure 5.29: Strain comparison ε_{xx} at radial position $R = 13000\ mm$ for Mxmin load case.

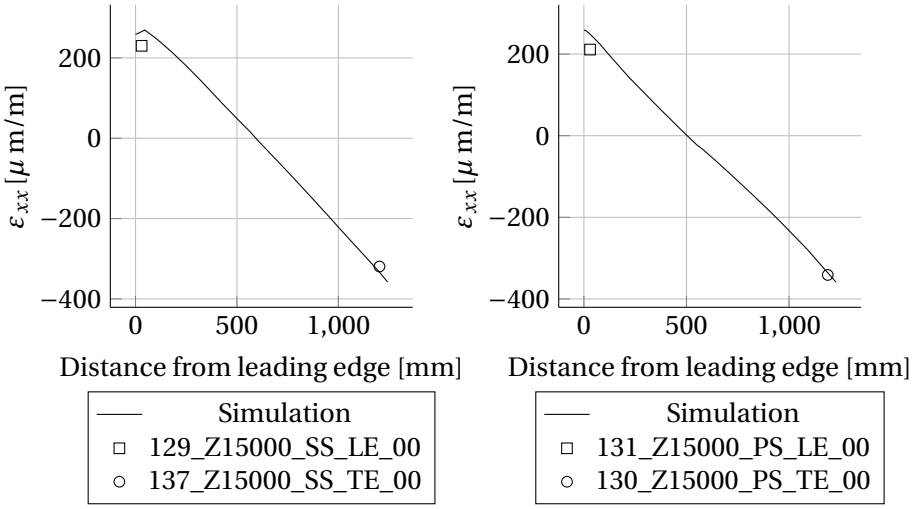

(a) Suction side.

(b) Pressure side.

Figure 5.30: Strain comparison ε_{xx} at radial position $R = 15000\ mm$ for Mxmin load case.

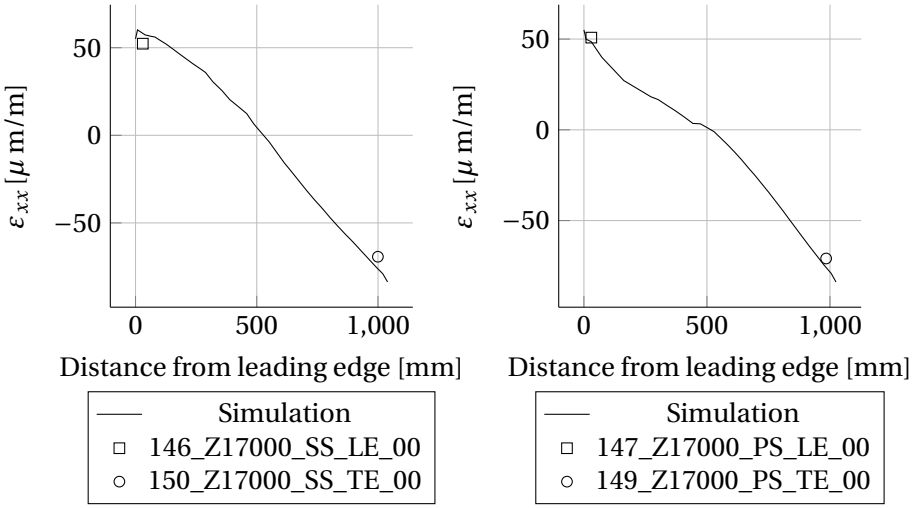

(a) Suction side.

(b) Pressure side.

Figure 5.31: Strain comparison ε_{xx} at radial position $R = 17000\ mm$ for Mxmin load case.

5.3.3 Mymax results

The results for the load case Mymax (cf. Figure 3.4a) are shown in Figure 5.32a - Figure 5.44. Due to the orientation of the rotor blade it can be expected that the mechanical strains at the belts are greater compared to the leading and trailing edges. Both the simulation and the experiment confirm this expectation, cf. Figure 5.32 for the belts and Figure 5.33 - 5.44 for the leading and trailing edge.

The comparison of the ε_{xx} strain distribution and values of the belts are shown in Figure 5.32a for the suction side and Figure 5.32b for the pressure side. The simulated values are for nearly all sensor values in good agreement. Only the strains near the root are overestimated by the simulation. This means that the wind turbine blade model is too soft.
The strongly instrumented profiles R = 5000 mm and R = 8000 mm are shown in Figure 5.36 - 5.40. The simulated ε_{xx} values and distribution at the suction (cf. Figure 5.36a) and pressure side (cf. Figure 5.36b) and ε_{yy} (cf. Figure 5.37b) at the pressure side are in very good agreement with the experiment for the profile R = 5000 mm. For the results of ε_{yy} at the suction side (cf. Figure 5.37a) the strain distribution between 0 mm - 1100 mm distance from the leading edge differs between experiment and simulation. The gradient between measurements and simulation is not equal. For the numerical solution the maximum strain value is reached at an “earlier” distance. The pressure side does not show such behavior. The strains between 800 mm - 1200 mm are overestimated by the simulation.

For R = 8000 mm the simulated ε_{xx} suction (cf. Figure 5.38a) and pressure side (cf. Figure 5.38b) strain distribution and values are in very good agreement with the experiment. The simulated ε_{yy} strain distribution for the suction (cf. Figure 5.39a) and pressure side (cf. Figure 5.39b) match also with experiments. However, the absolute ε_{yy} strain values differ. Most of the suction side ε_{yy} strain values are overestimated by the numerical solution. Only the peak ε_{yy} strain value is underestimated. In contrast to this, most of the ε_{yy} strain values are underestimated by the simulation.

All measured values ε_{xx} for the profiles R = 1600 mm, 2700 mm, 11000 mm, 13000 mm, 15000 mm and 17000 mm are in good agreement with the simulation. In this profile only the leading and trailing edge were instrumented with strain gauges. Therefore, the profile strain distribution is unknown.

MyMax - belt

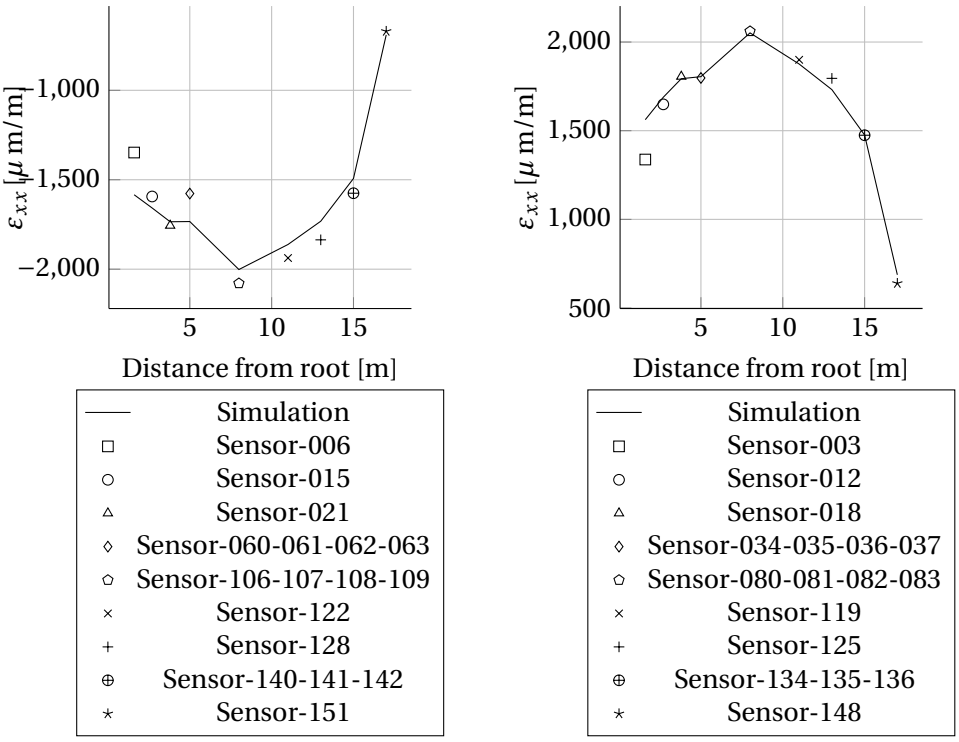

(a) Suction side belt.

(b) Pressure side belt.

Figure 5.32: Strain comparison ε_{xx} for Mymax load case.

MyMax - Section wise

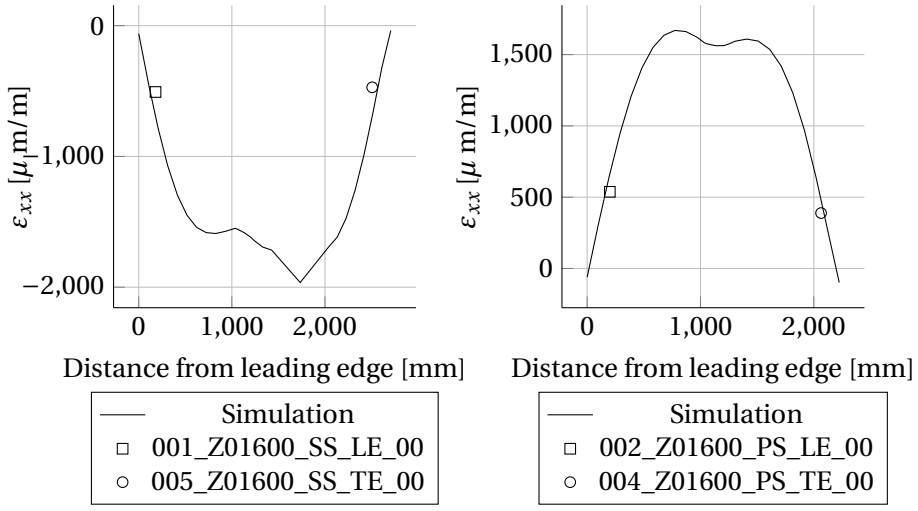

(a) Suction side.

(b) Pressure side.

Figure 5.33: Strain comparison ε_{xx} at radial position $R = 1600\ mm$ for Mymax load case.

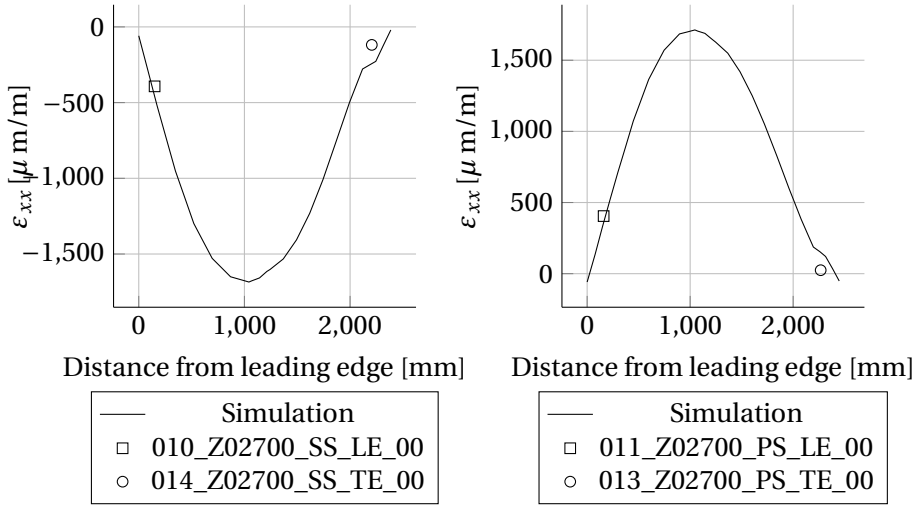

(a) Suction side.

(b) Pressure side.

Figure 5.34: Strain comparison ε_{xx} at radial position $R = 2700\ mm$ for Mymax load case.

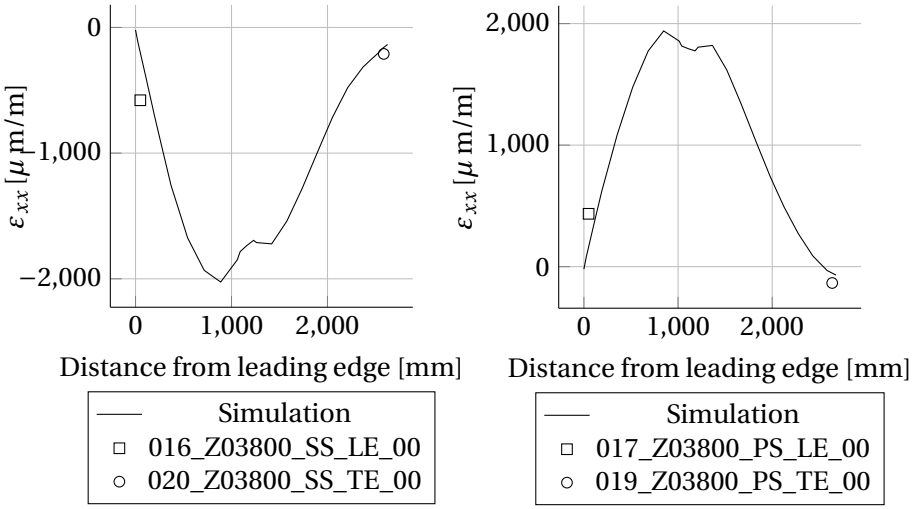

(a) Suction side.

(b) Pressure side.

Figure 5.35: Strain comparison ε_{xx} at radial position $R = 3800\ mm$ for Mymax load case.

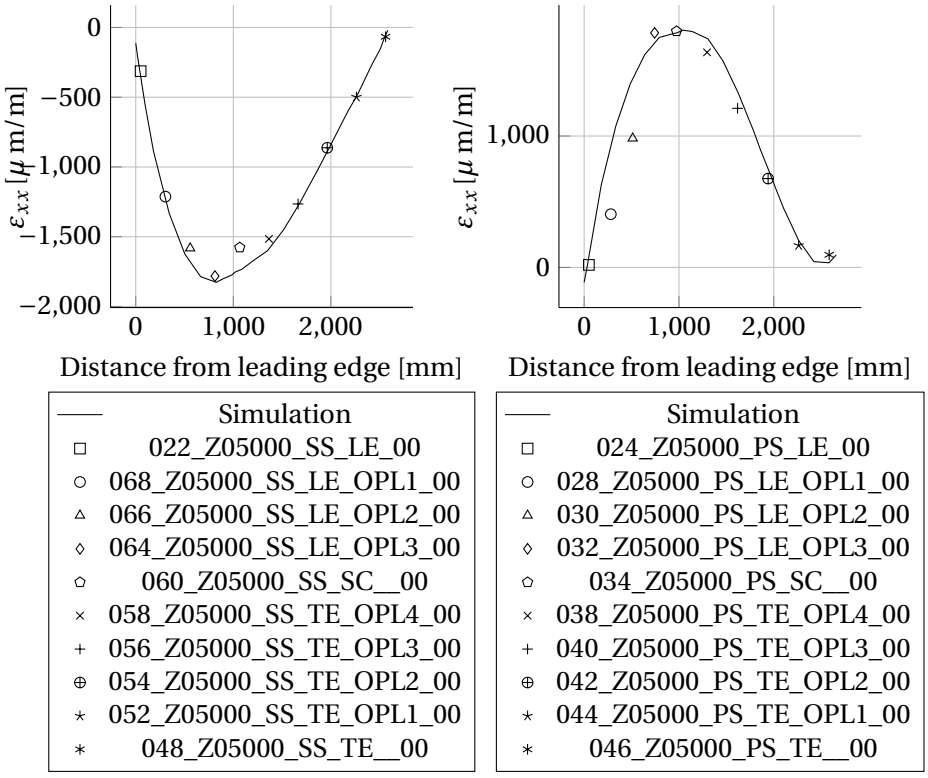

(a) Suction side.

(b) Pressure side.

Figure 5.36: Strain comparison ε_{xx} at radial position $R = 5000\ mm$ for Mymax load case.

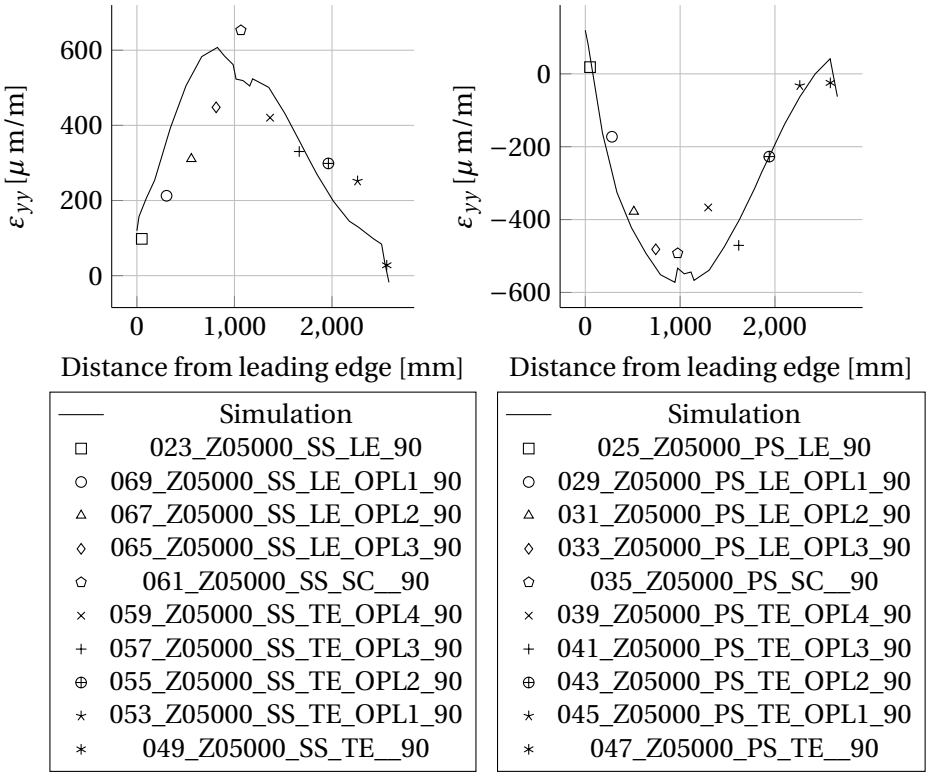

(a) Suction side.

(b) Pressure side.

Figure 5.37: Strain comparison ε_{yy} at radial position $R = 5000\ mm$ for Mymax load case.

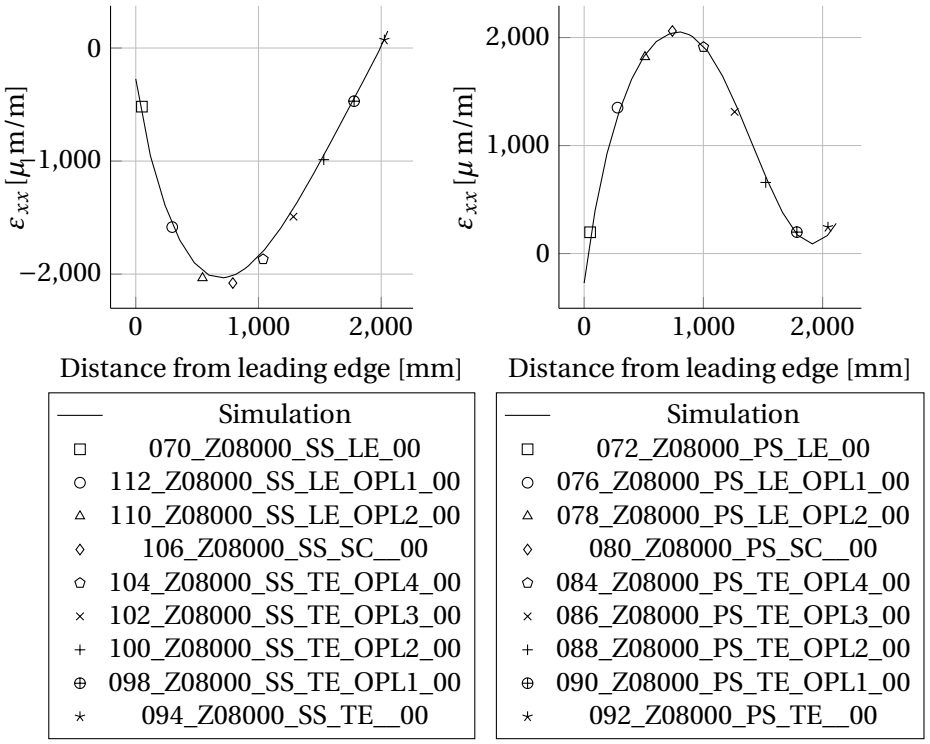

(a) Suction side.

(b) Pressure side.

Figure 5.38: Strain comparison ε_{xx} at radial position $R = 8000\ mm$ for Mymax load case.

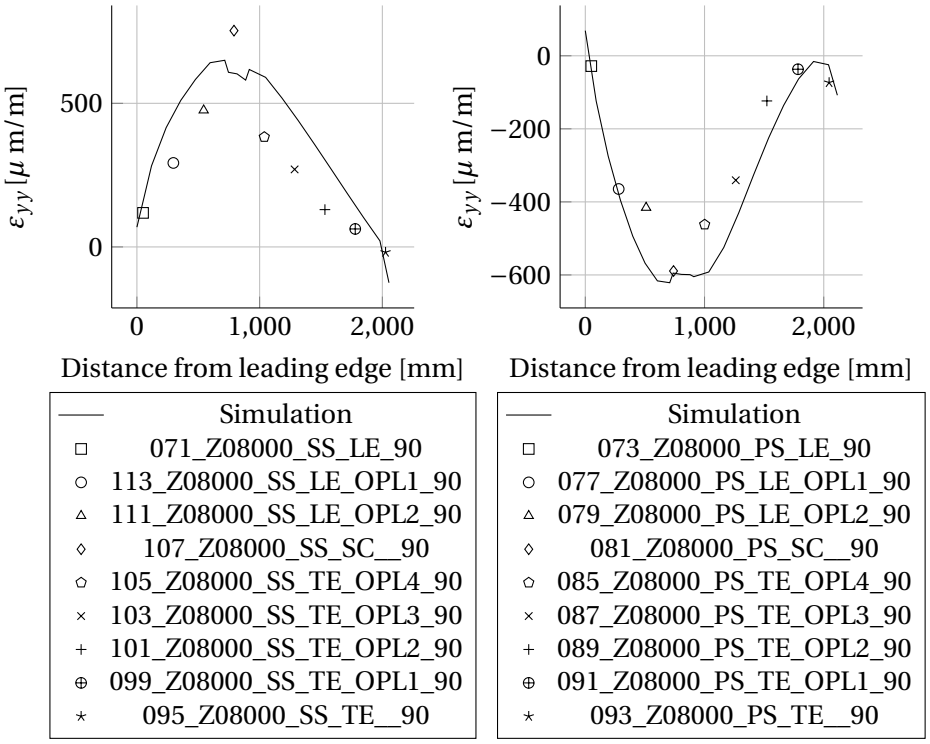

(a) Suction side.

(b) Pressure side.

Figure 5.40: Strain comparison ε_{yy} at radial position $R = 8000\ mm$ for Mymax load case.

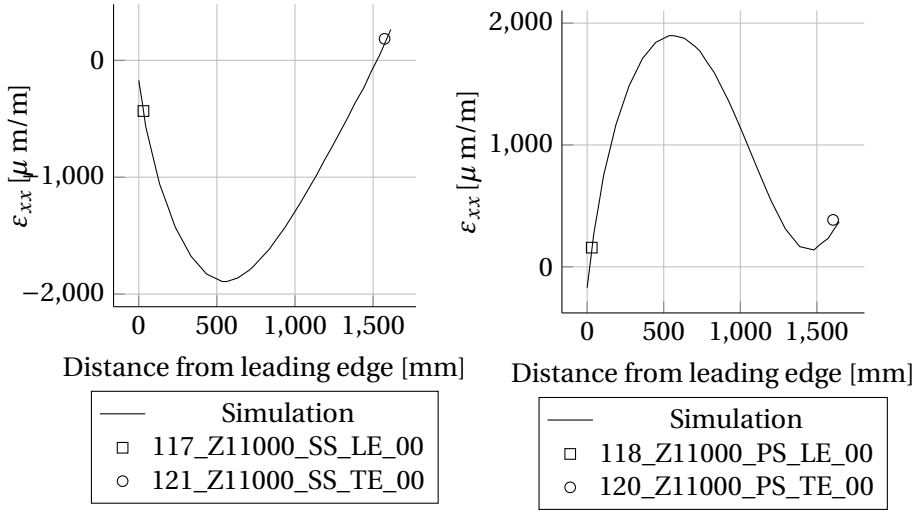

(a) Suction side.

(b) Pressure side.

Figure 5.41: Strain comparison ε_{xx} at radial position $R = 11000\ mm$ for Mymax load case.

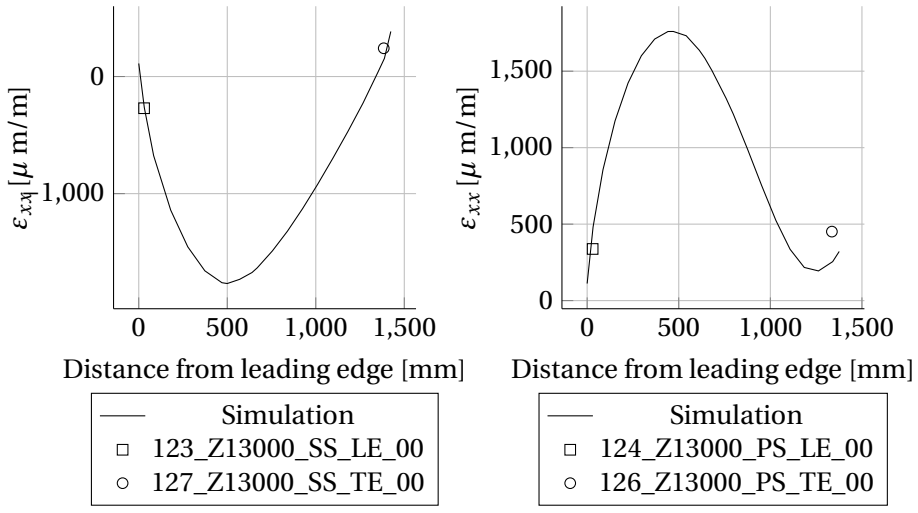

(a) Suction side.

(b) Pressure side.

Figure 5.42: Strain comparison ε_{xx} at radial position $R = 13000\ mm$ for Mymax load case.

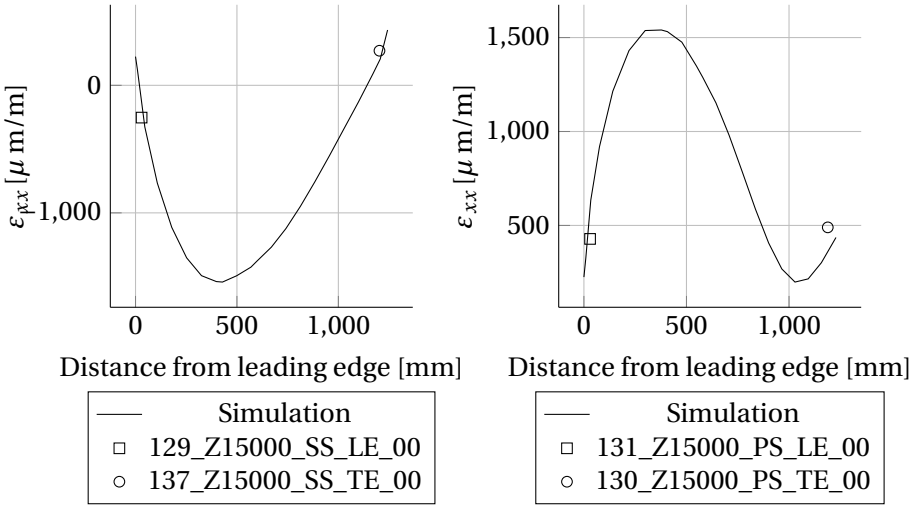

(a) Suction side.

(b) Pressure side.

Figure 5.43: Strain comparison ε_{xx} at radial position $R = 15000\ mm$ for Mymax load case.

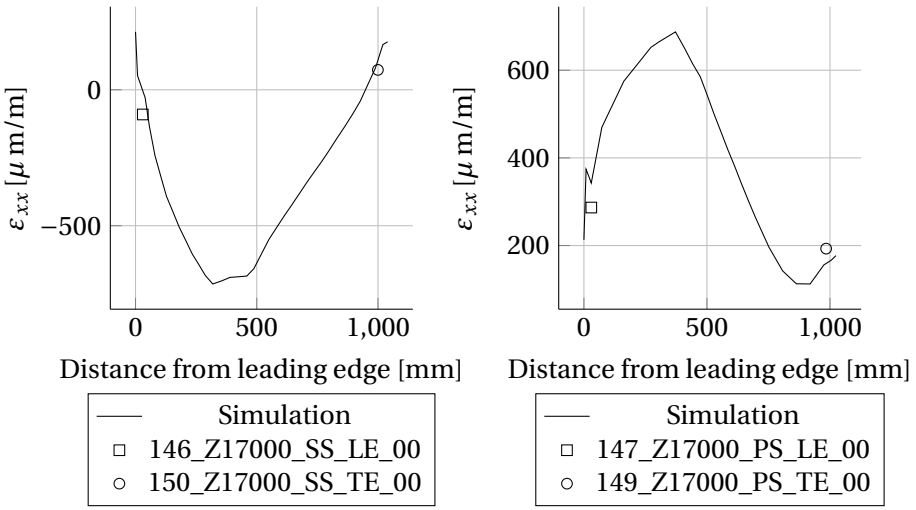

(a) Suction side.

(b) Pressure side.

Figure 5.44: Strain comparison ε_{xx} at radial position $R = 17000\ mm$ for Mymax load case.

5.3.4 Mymin results

The results for the load case Mymin (cf. Figure 3.4b) are shown in appendix Figure 5.45a - Figure 5.57. Due to the orientation of the rotor blade it can be expected that the mechanical strains at the belts are greater compared to the leading and trailing edges. Both the simulation and the experiment confirm this expectation, cf. Figure 5.45 for the belts and Figure 5.46 - 5.57 for the leading and trailing edge. Comparing the load cases Mymax and Mymin for the belts a switch in signs of the $\mu\varepsilon_{xx}$ strain values can be seen, cf. Figure 5.6a and Figure 5.19a. This is expected because the wind turbine blade was rotated by 180° between the two load cases.

The absolute deviations are small for most measuring positions. As expected, the relative deviations are higher in areas with small strains than in areas with larger strains. This behavior can be seen very well when comparing the suction side belts with the pressure side belt. These are the absolute values for the pressure side. Therefore the deviations are relatively high. The suction side course matches well between simulation and experiment. In the case of the pressure side, there are larger differences in the area near the root.

The comparison of the ε_{xx} strain distribution and values of the belts are shown in Figure 5.45a for the suction side and Figure 5.45b for the pressure side. The simulated values are for nearly all sensor values in good agreement. Only the strains near the root are overestimated by the simulation. The means the wind turbine blade model is to soft as concluded for the Mymax load case. This agrees underline the assumption made that the root stiffness is modeled to soft.
The strongly instrumented profiles R = 5000 mm and R = 8000 mm are shown in Figure 5.49 - 5.53. The simulated ε_{xx} values and distribution at the suction (cf. Figure 5.49a) and pressure side (cf. Figure 5.49b) and ε_{yy} (cf. Figure 5.50b) at the pressure side are in very good agreement with the experiment for the profile R = 5000 mm. For the results of ε_{yy} strain values at the suction side (cf. Figure 5.50a) the strain distribution between 800 mm - 1500 mm distance from the leading edge differs between experiment and simulation. The strain distribution is nearly constant for the measured strains exception of the ε_{yy} belt strain values. The simulated values overestimate the measured once. The pressure side does not show such behavior

for the ε_{yy} strain values.

For R = 8000 mm the simulated ε_{xx} suction (cf. Figure 5.51a)and pressure side (cf. Figure 5.51b) strain distribution and values are in very good agreement with the experiment. The simulated ε_{yy} strain distribution for the suction side (cf. Figure 5.52a)shows a result similar to R = 5000 mm. The ε_{yy} strain values are overestimated by the simulation. For the pressure side the ε_{yy} strain values as well as the principle distribution are correct. However, the ε_{yy} strain distribution gradient between 800 mm - 1600 mm distance from the leading edge is lower for the numerical results compared to the experimental once.

All measured values ε_{xx} for the profiles R = 1600 mm, 2700 mm, 11000 mm, 13000 mm, 15000 mm and 17000 mm are in good agreement with the simulation. In this profile only the leading and trailing edge were instrumented with strain gauges. Therefore, the profile strain distribution is unknown.

MyMin - belt

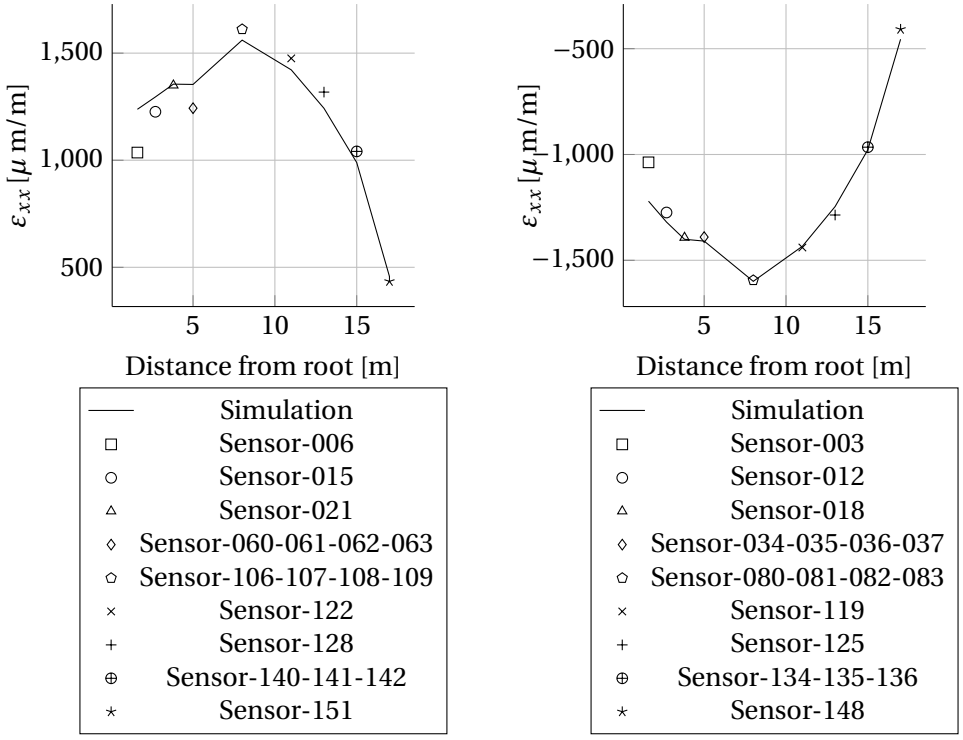

(a) Suction side belt.

(b) Pressure side belt.

Figure 5.45: Strain comparison ε_{xx} for Mymin load case.

MyMin - Section wise

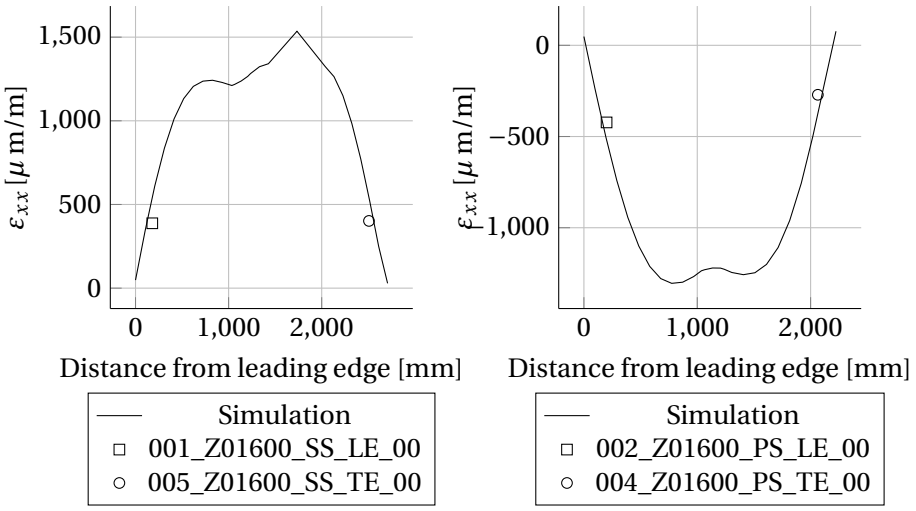

(a) Suction side.

(b) Pressure side.

Figure 5.46: Strain comparison ε_{xx} at radial position $R = 1600\ mm$ for Mymin load case.

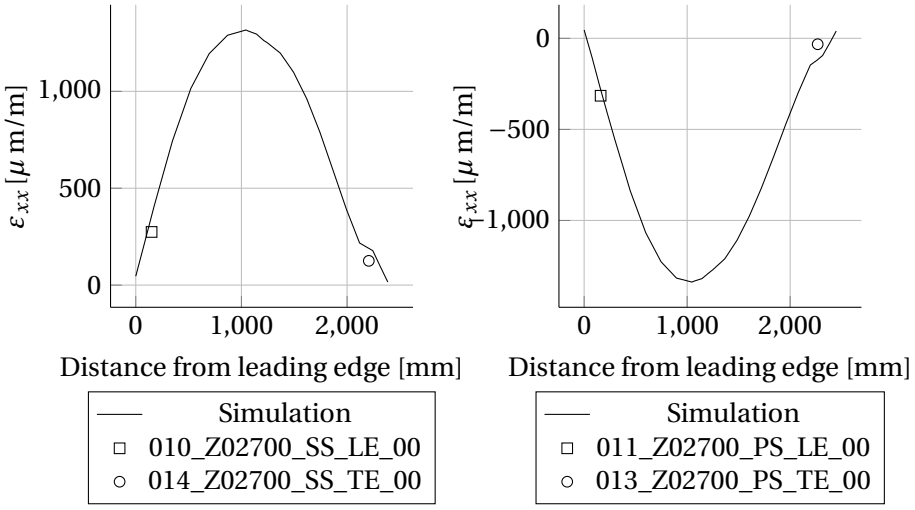

(a) Suction side.

(b) Pressure side.

Figure 5.47: Strain comparison ε_{xx} at radial position $R = 2700\ mm$ for Mymin load case.

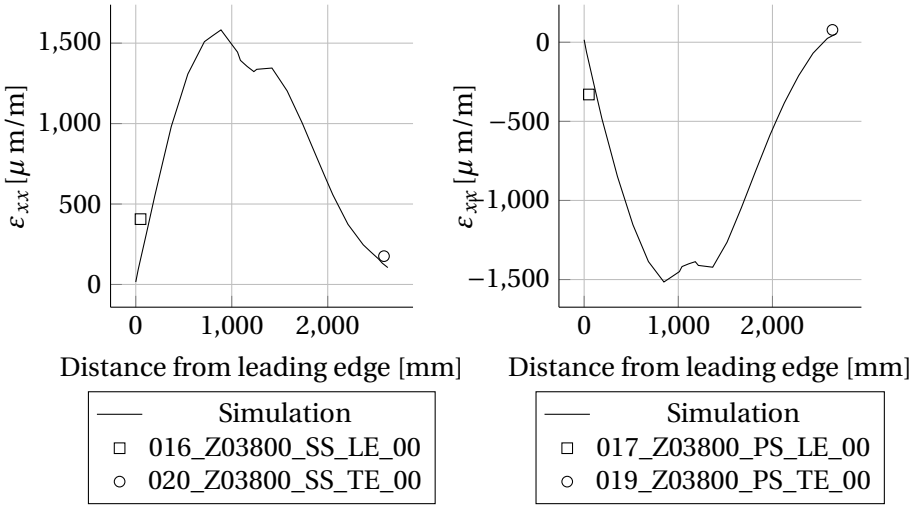

(a) Suction side.

(b) Pressure side.

Figure 5.48: Strain comparison ε_{xx} at radial position $R = 3800\ mm$ for Mymin load case.

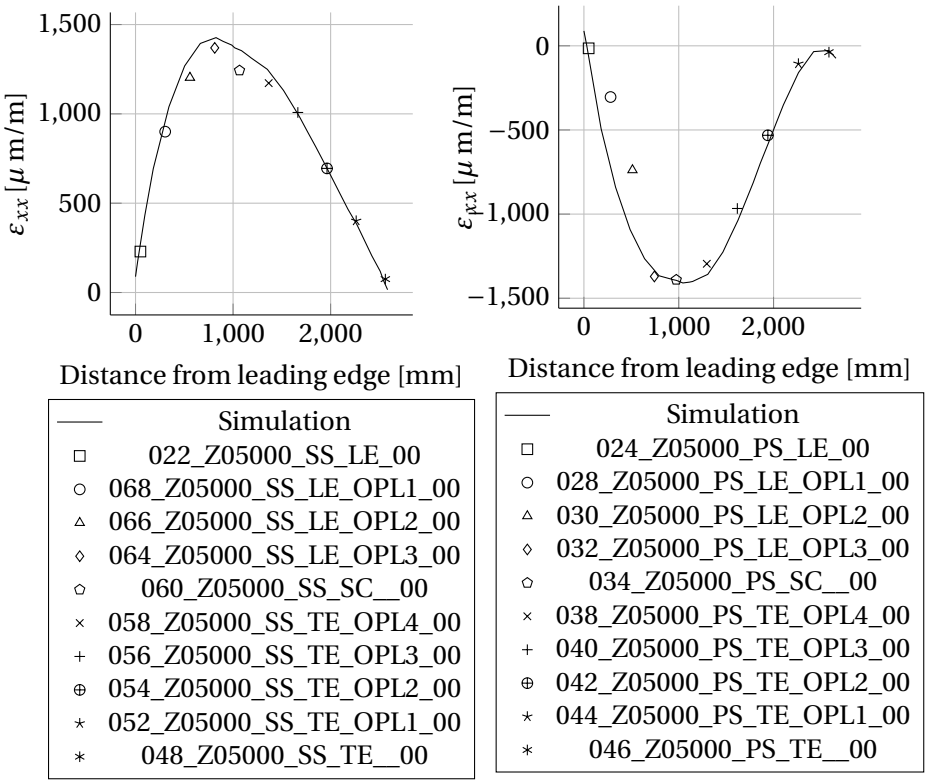

(a) Suction side.

(b) Pressure side.

Figure 5.49: Strain comparison ε_{xx} at radial position $R = 5000\ mm$ for Mymin load case.

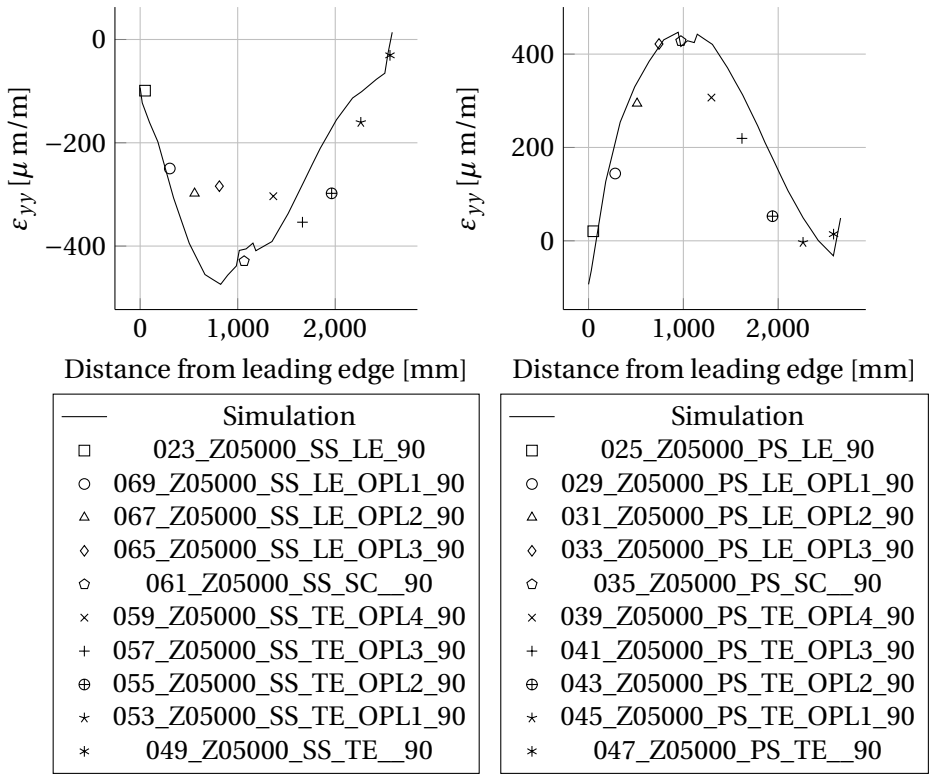

(a) Suction side.

(b) Pressure side.

Figure 5.50: Strain comparison ε_{yy} at radial position $R = 5000\ mm$ for Mymin load case.

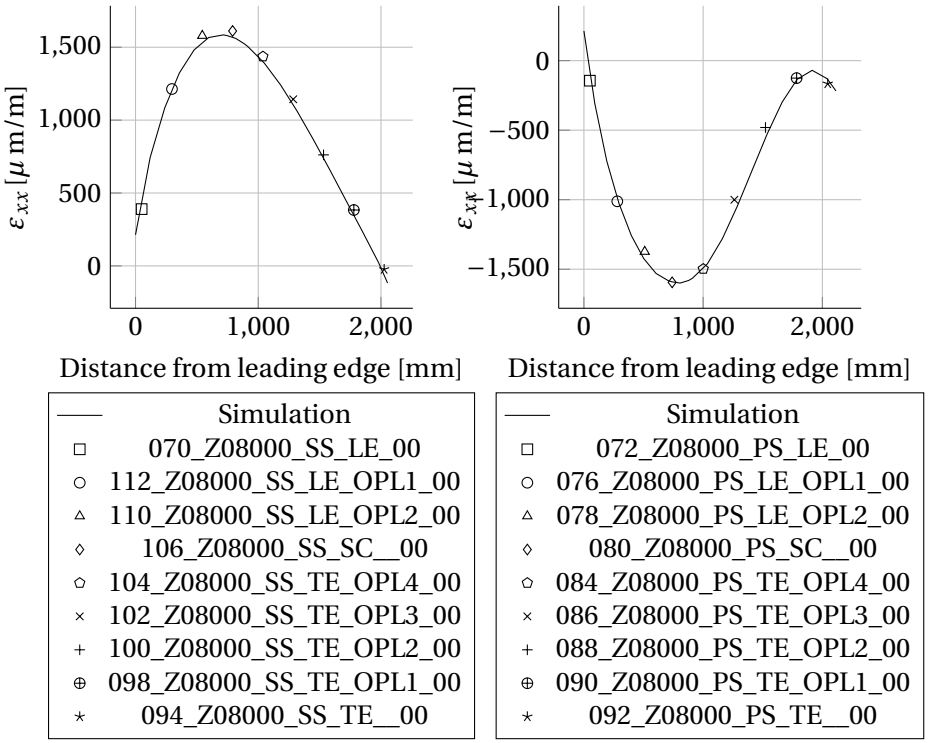

(a) Suction side.

(b) Pressure side.

Figure 5.51: Strain comparison ε_{xx} at radial position $R = 8000\ mm$ for Mymin load case.

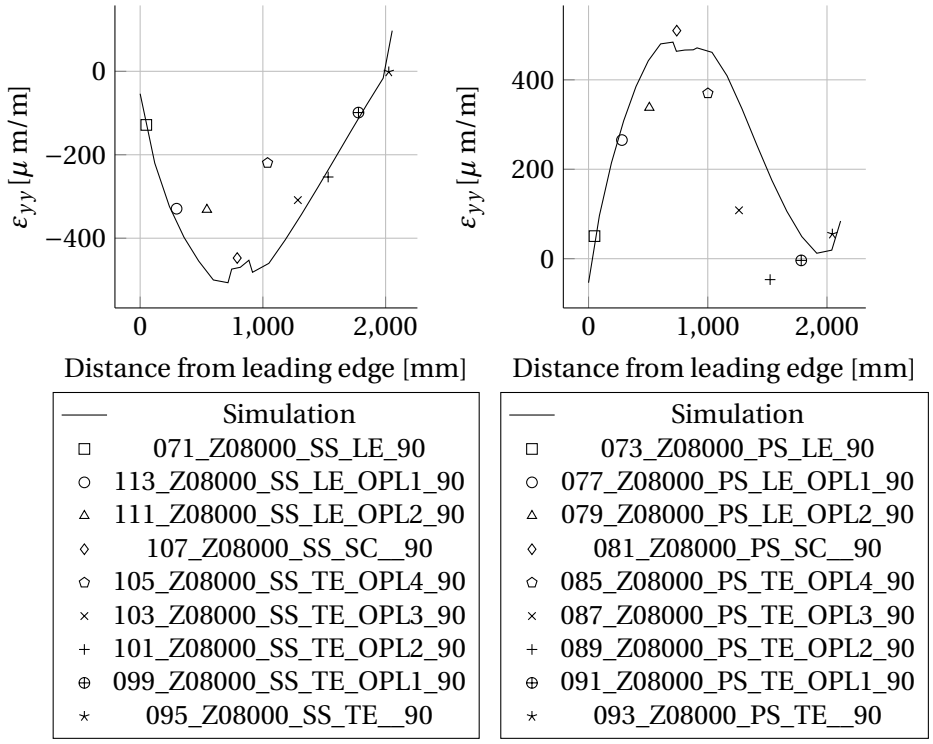

(a) Suction side.

(b) Pressure side.

Figure 5.53: Strain comparison ε_{yy} at radial position $R = 8000\ mm$ for Mymin load case.

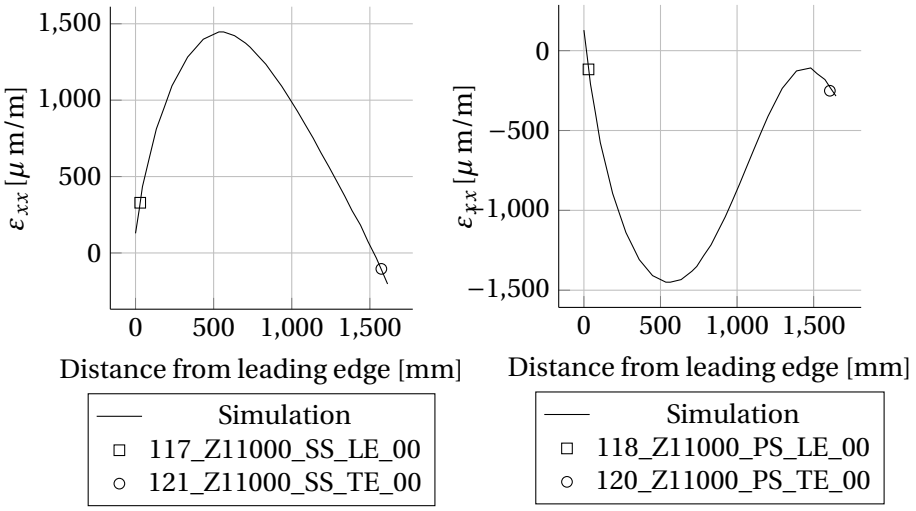

(a) Suction side.

(b) Pressure side.

Figure 5.54: Strain comparison ε_{xx} at radial position $R = 11000\ mm$ for Mymin load case.

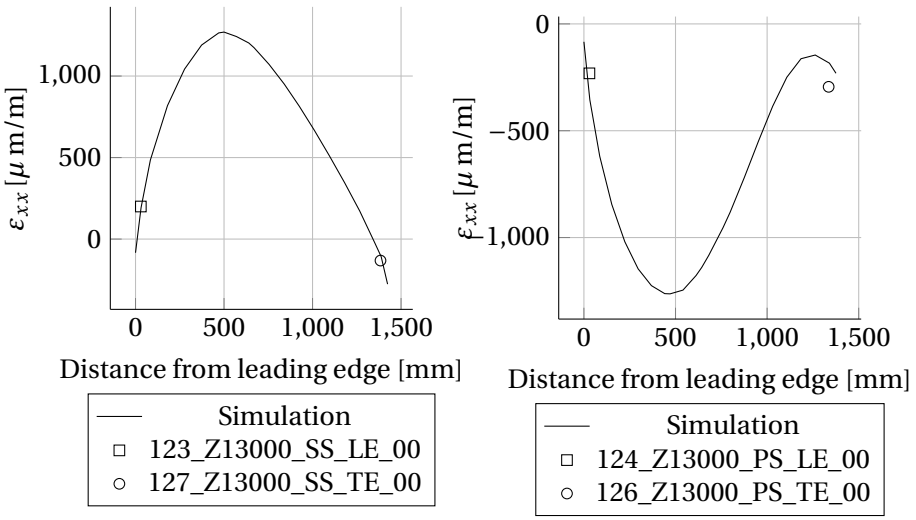

(a) Suction side.

(b) Pressure side.

Figure 5.55: Strain comparison ε_{xx} at radial position $R = 13000\ mm$ for Mymin load case.

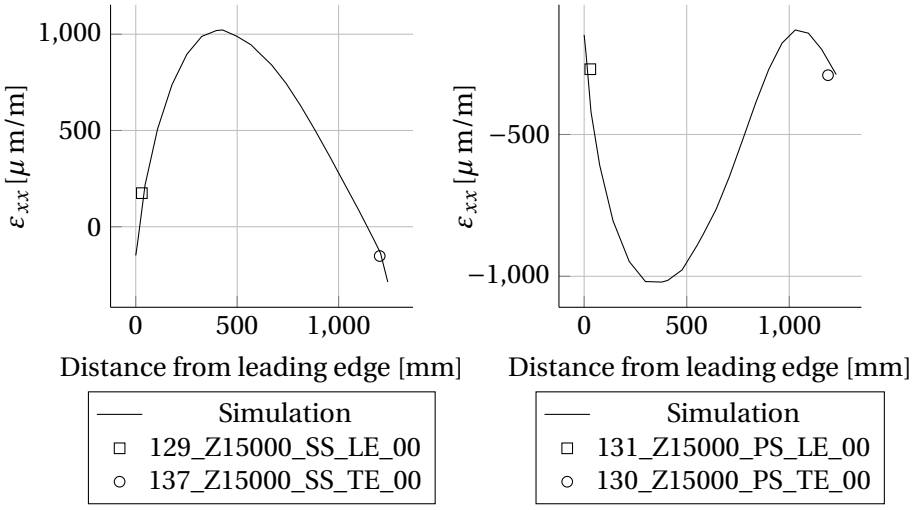

(a) Suction side.

(b) Pressure side.

Figure 5.56: Strain comparison ε_{xx} at radial position $R = 15000\ mm$ for Mymin load case.

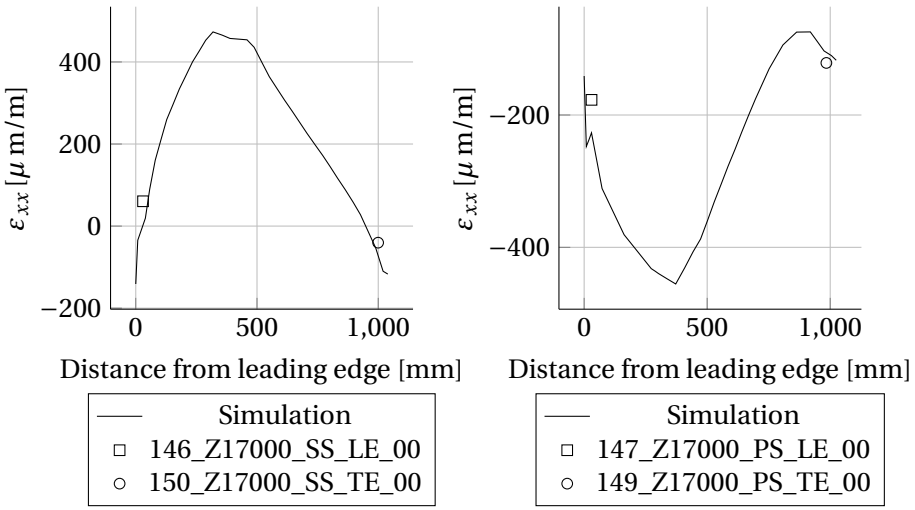

(a) Suction side.

(b) Pressure side.

Figure 5.57: Strain comparison ε_{xx} at radial position $R = 17000\ mm$ for Mymin load case.

5.4 Torsion results

The comparison of the torsion stiffness measurement (see section 3.4) results and the numerical results are illustrated in Figure 5.58 - Figure 5.61. Three scenarios (LC_1, LC_2 and LC_3) are measured and simulated. The load vector for the load cases are given in Table 3.3. The scenario LC_1 is in good agreement for all measured profiles. In this scenario the error is dominated by the load introduction point R = 9700 mm. Because this error is small, the outer radial profile errors are small as well. For scenario LC_2 the error is greater compared to LC_1 for the profiles R = 14000 mm and R = 17700 mm. The numerical model is softer compared to the tested blade, because the angle of rotation (inclination of the curve) is larger. For the scenario LC_3 the largest error occur at R = 17700 mm, where the load is introduced.
The strain distributions for the intensively instrumented profiles R = 5000 mm and R = 8000 mm are shown in Figure 5.62a - Figure 5.73 for all three load cases. Most of the numerical results are not in good agreement with the experimental data. Generally speaking, most of the strains are lower than 100 $\mu m/m$. As in the bending cases these small strains are more sensitive against minor orientation and placement errors. For larger strains above 100 $\mu m/m$ the curves are in better agreement and fits best for Figure 5.62b, Figure 5.64a and Figure 5.64b for the first load case LC_1. For LC_3 Figure 5.70b and Figure 5.72b show good agreement between simulation and measurements.

5.4.1 Displacement plots for all the torsion load cases

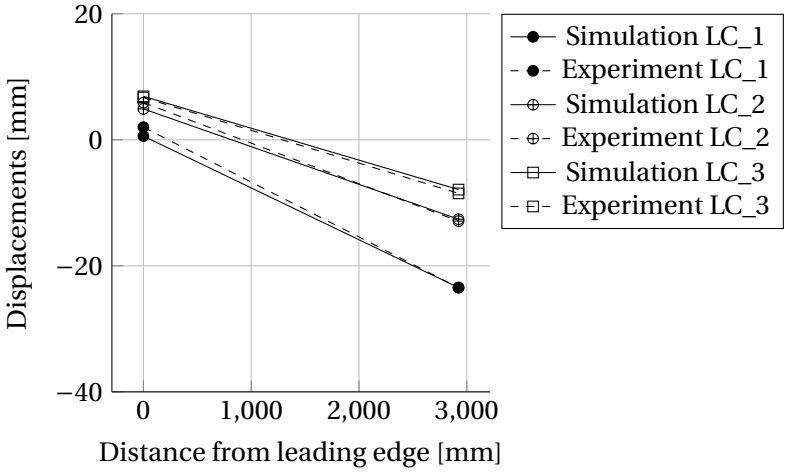

Figure 5.58: Displacements at position $R = 6700$ mm for all torsion load cases.

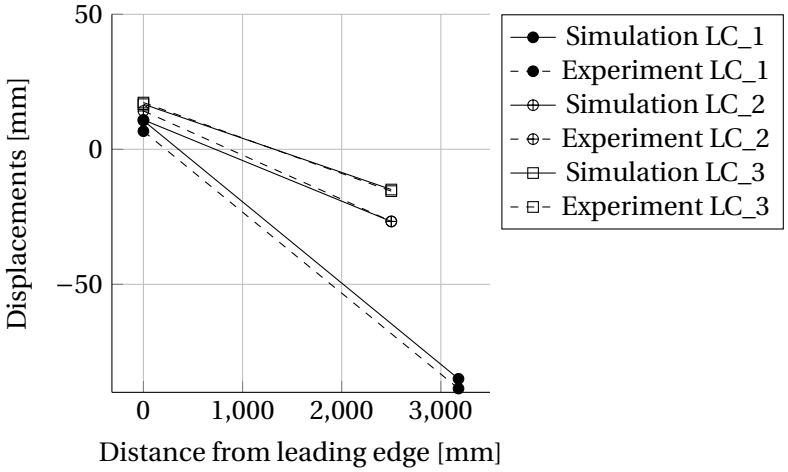

Figure 5.59: Displacements at position $R = 9700$ mm for all torsion load cases.

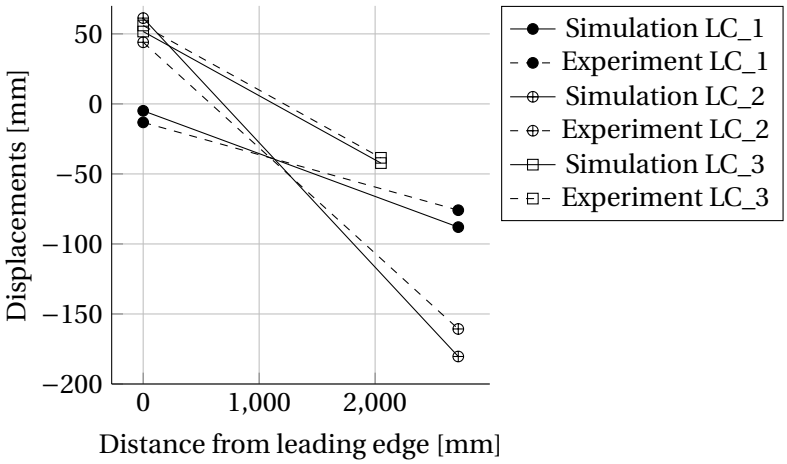

Figure 5.60: Displacements at position R = 14000 mm for all torsion load cases.

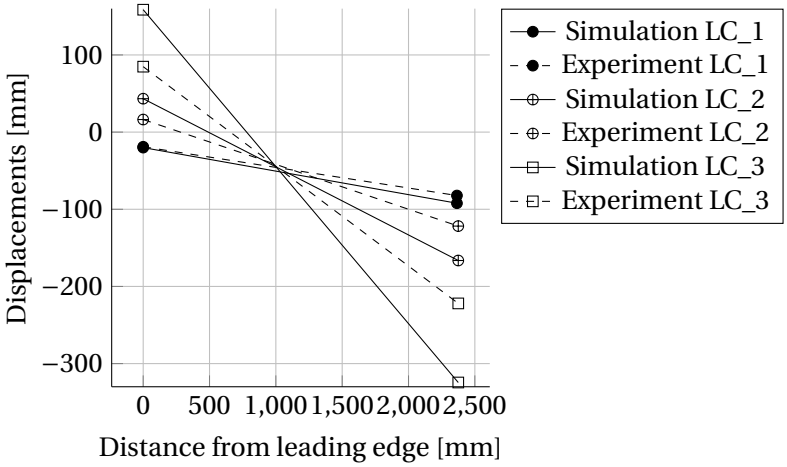

Figure 5.61: Displacements at position R = 17700 mm for all torsion load cases.

5.4.2 Strain plots - Torsion LC_1

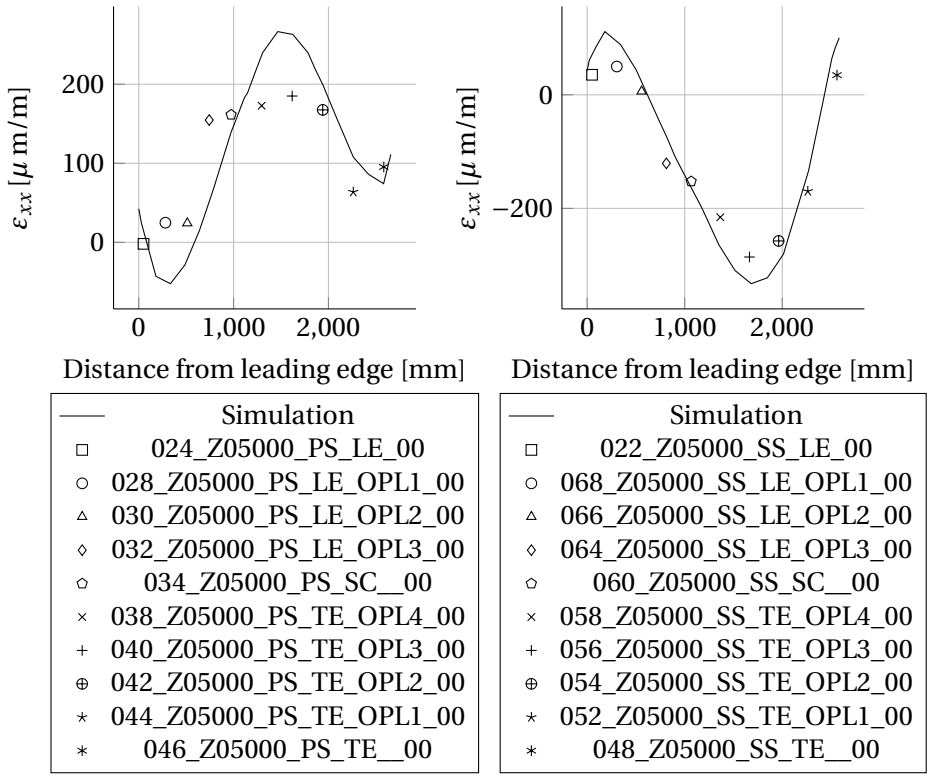

(a) Suction side.

(b) Pressure side.

Figure 5.62: Strain comparison ε_{xx} at radial position $R = 5000$ mm for torsion load case LC_1.

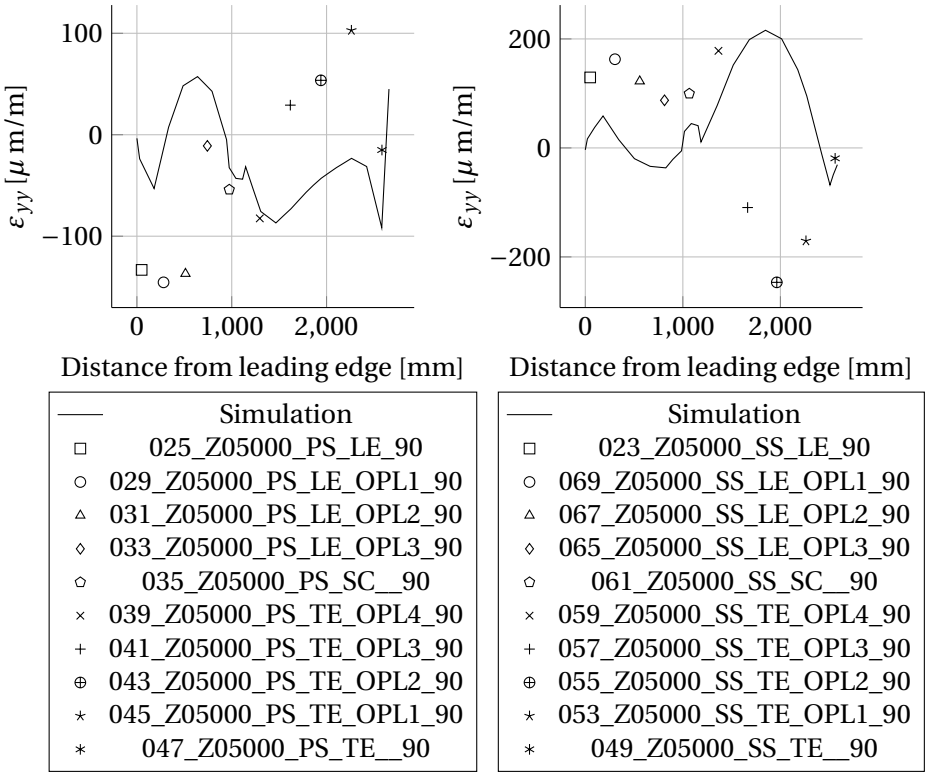

(a) Suction side.

(b) Pressure side.

Figure 5.63: Strain comparison ε_{yy} at radial position $R = 5000\ mm$ for torsion load case LC_1.

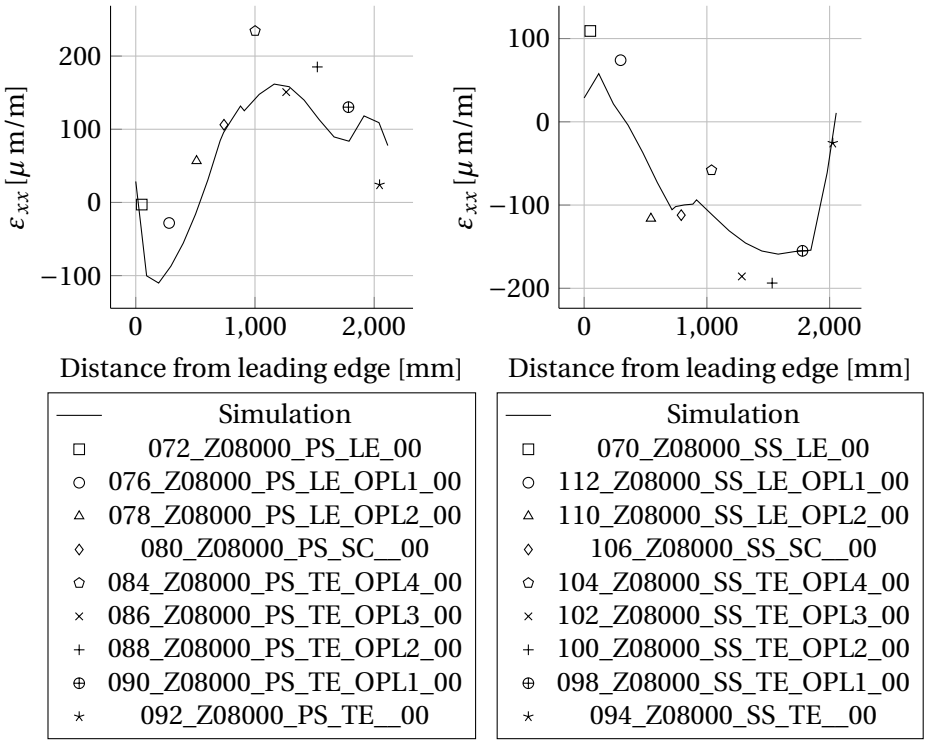

(a) Suction side.

(b) Pressure side.

Figure 5.64: Strain comparison ε_{xx} at radial position $R = 8000$ mm for torsion load case LC_1.

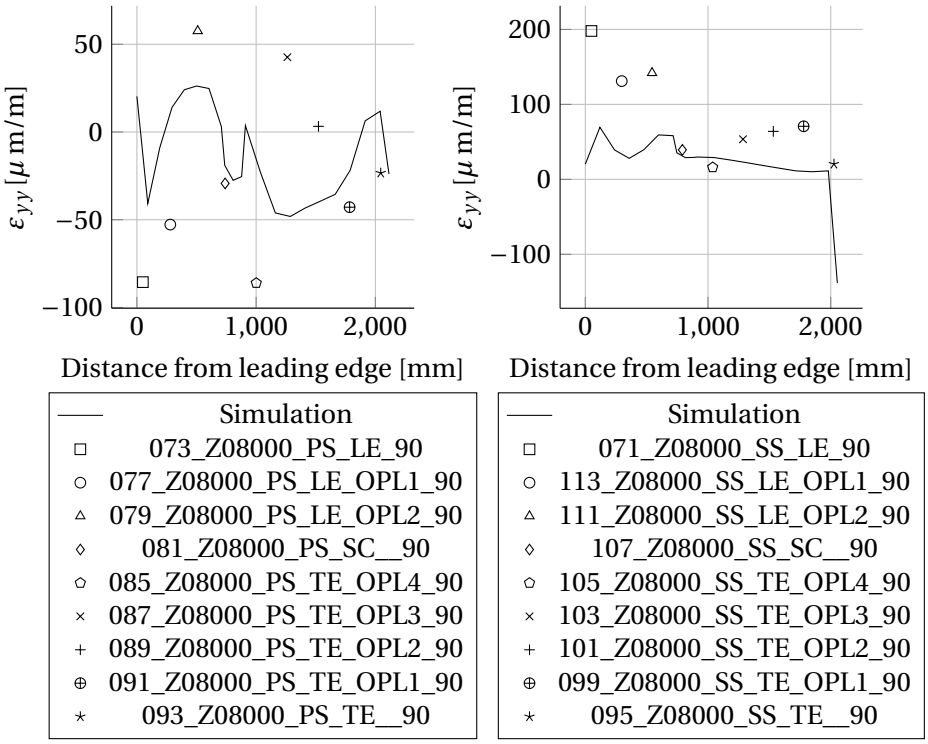

(a) Suction side.

(b) Pressure side.

Figure 5.65: Strain comparison ε_{yy} at radial position $R = 8000$ mm for torsion load case LC_1.

5.4.3 Strain plots - Torsion LC_2

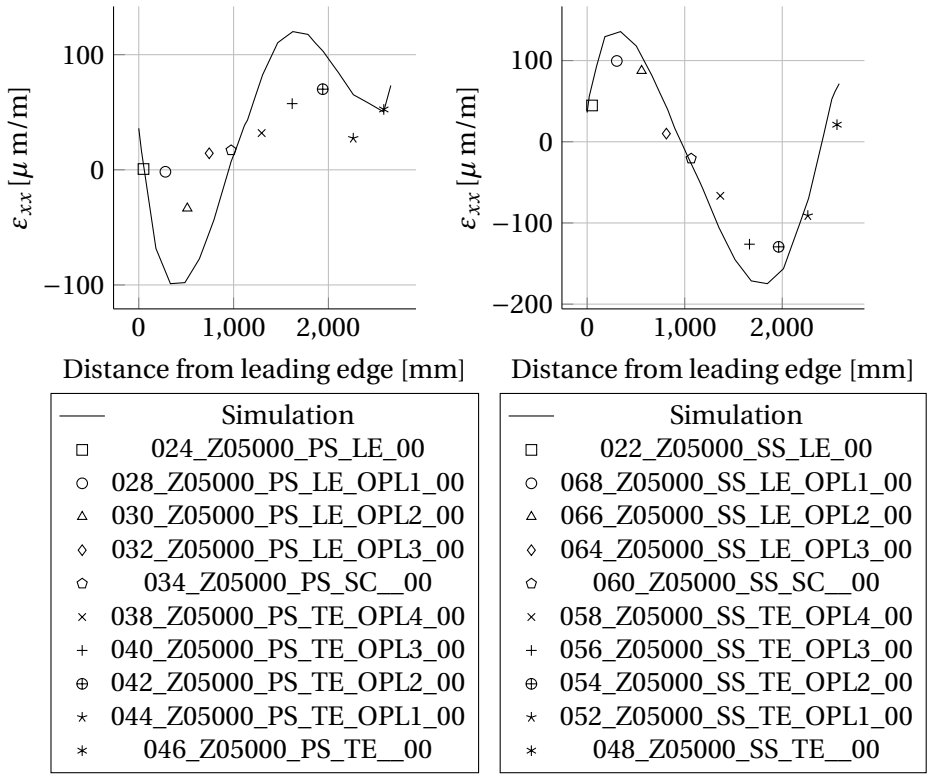

(a) Suction side.

(b) Pressure side.

Figure 5.66: Strain comparison ε_{xx} at radial position $R = 5000$ mm for torsion load case LC_2.

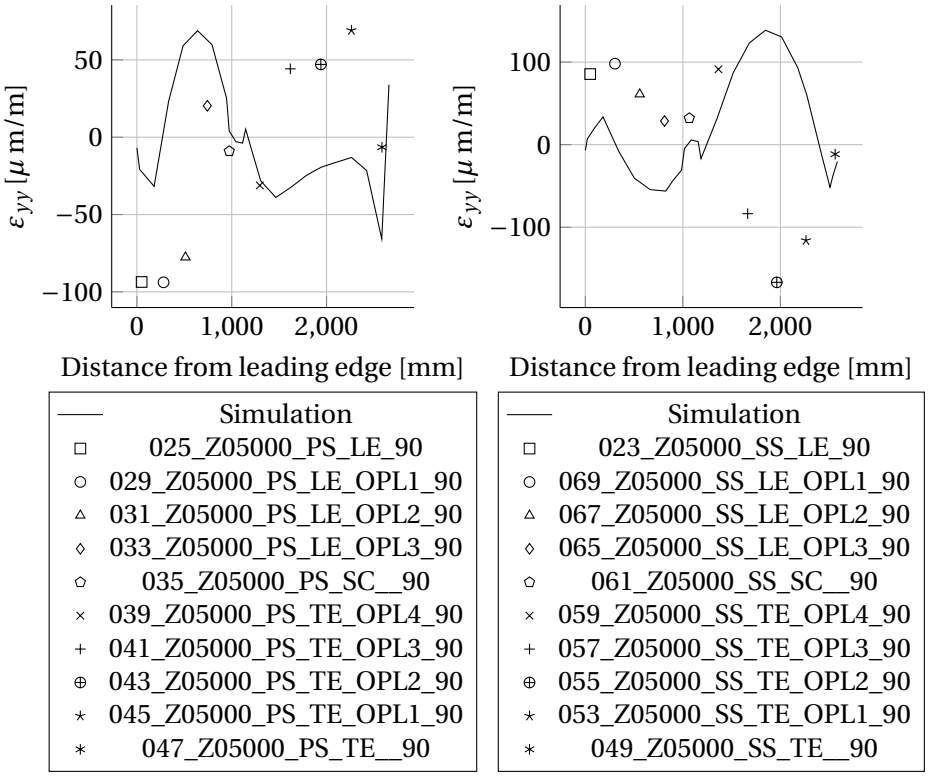

(a) Suction side.

(b) Pressure side.

Figure 5.67: Strain comparison ε_{yy} at radial position $R = 5000$ mm for torsion load case LC_2.

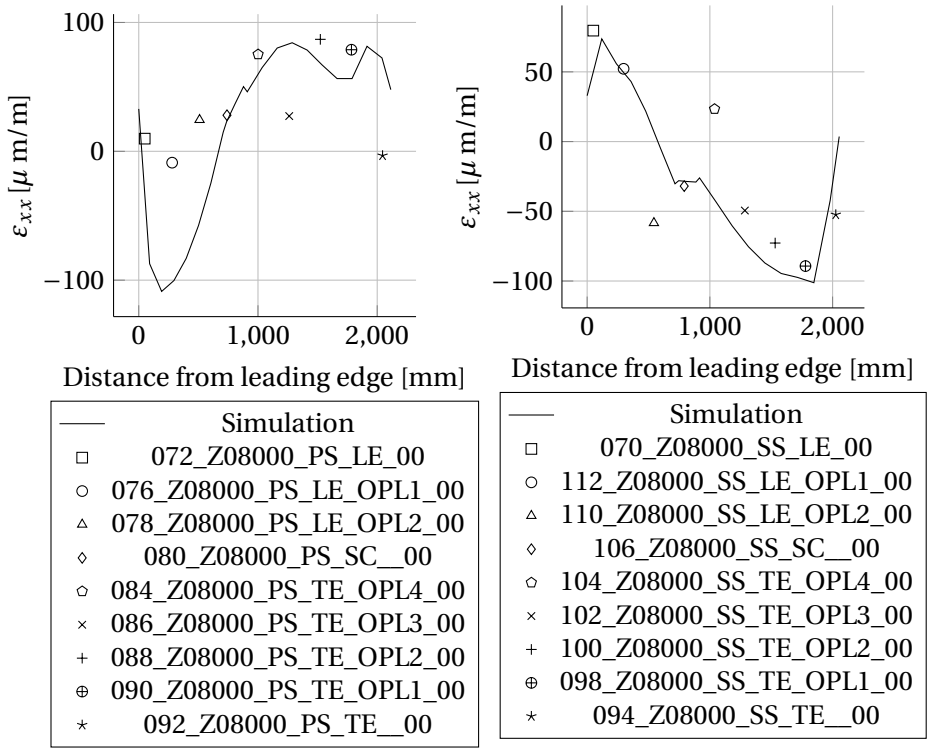

(a) Suction side.

(b) Pressure side.

Figure 5.68: Strain comparison ε_{xx} at radial position $R = 8000$ mm for torsion load case LC_2.

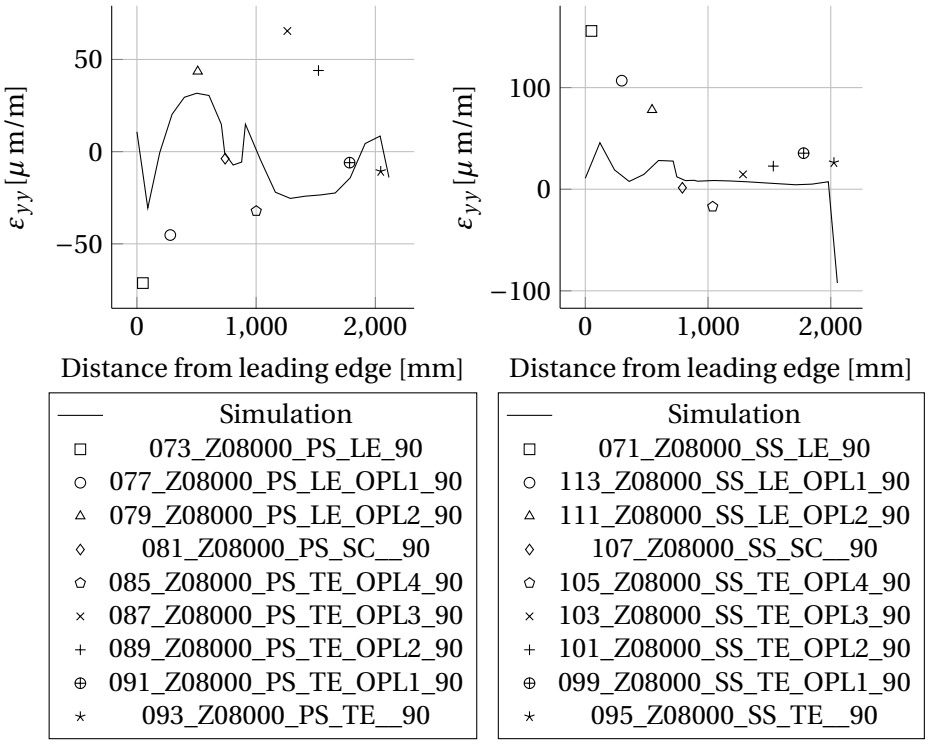

(a) Suction side.

(b) Pressure side.

Figure 5.69: Strain comparison ε_{yy} at radial position $R = 8000$ mm for torsion load case LC_2.

5.4.4 Strain plots - Torsion LC_3

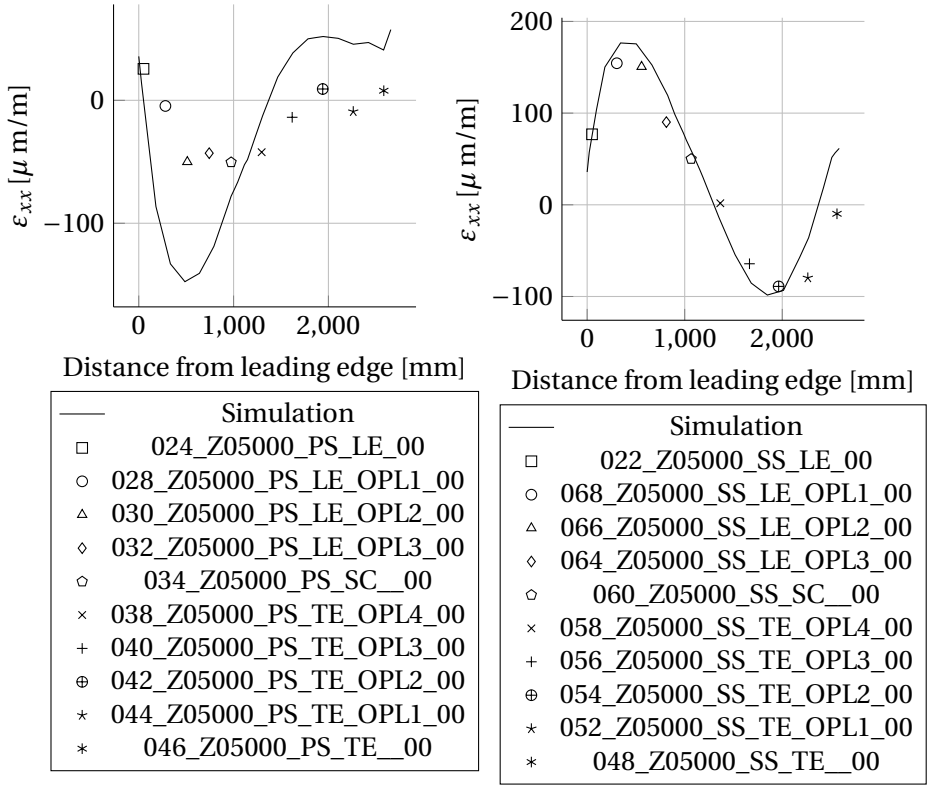

(a) Suction side.

(b) Pressure side.

Figure 5.70: Strain comparison ε_{xx} at radial position $R = 5000$ mm for torsion load case LC_3.

5.5 Effect of orientation of the blade

The simulation was performed for three different orientations i.e., 0°, 7.5° and 15°. The deviation in the results were less than 1% between 0° and 7.5° orientation.

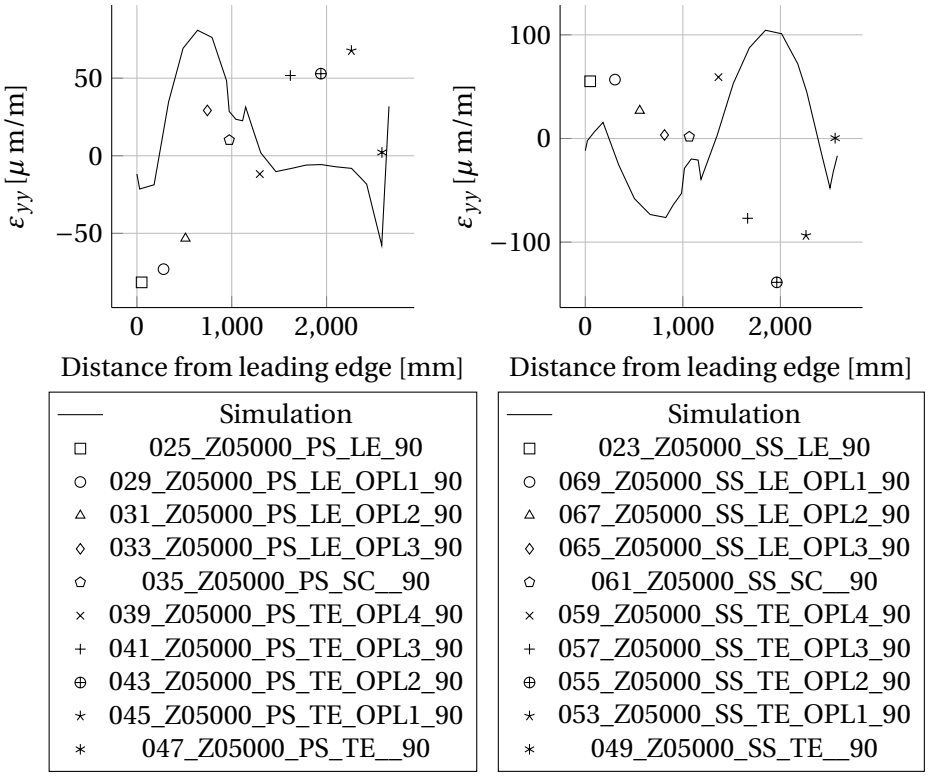

(a) Suction side.

(b) Pressure side.

Figure 5.71: Strain comparison ε_{yy} at radial position $R = 5000\ mm$ for torsion load case LC_3.

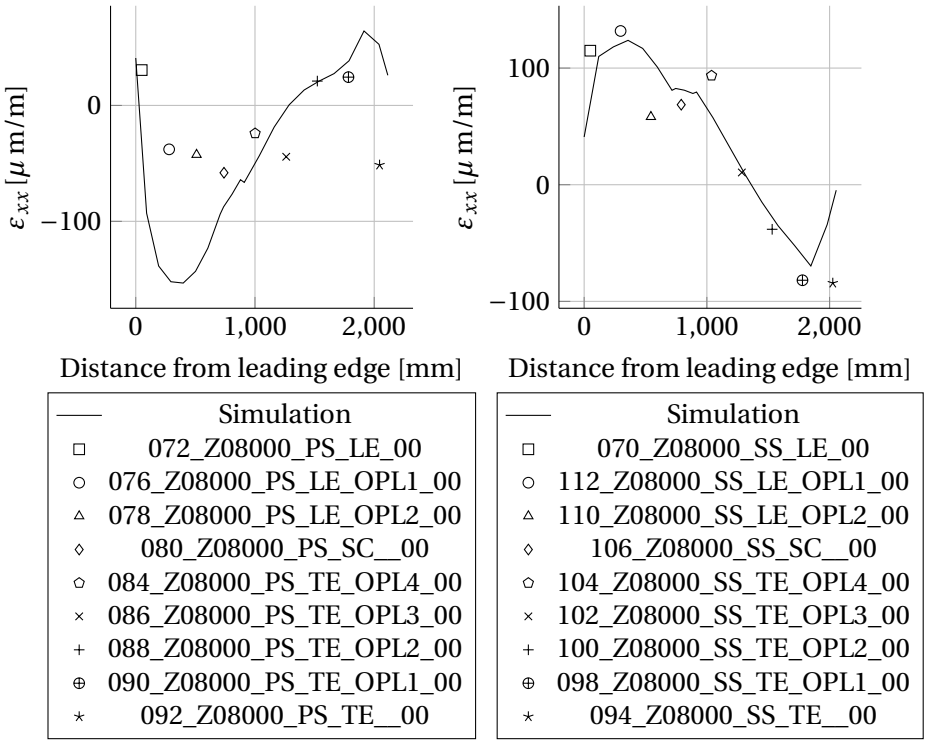

(a) Suction side.

(b) Pressure side.

Figure 5.72: Strain comparison ε_{xx} at radial position $R = 8000$ mm for torsion load case LC_3.

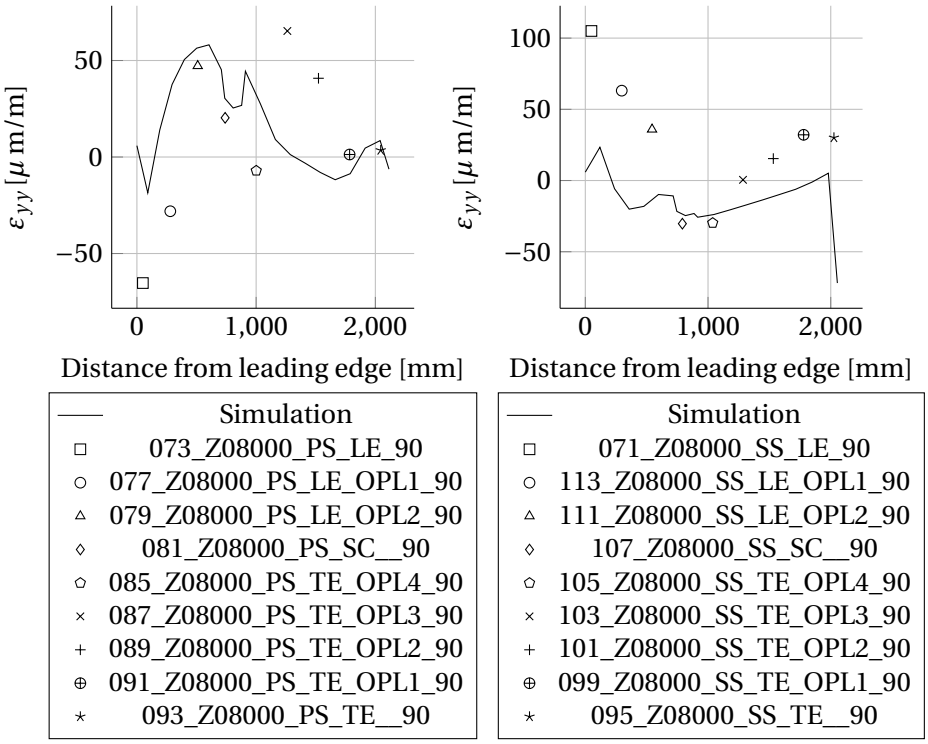

(a) Suction side.

(b) Pressure side.

Figure 5.73: Strain comparison ε_{yy} at radial position $R = 8000$ mm for torsion load case LC_3.

6

Summary and Conclusions

6.1 Summary

The present work dealt with the static structural simulation of extreme bending and torsion load cases on the given model and the simulation results were compared with the test results.
Generally speaking, most of the simulation results are in very good agreement with the experimental results for all the load cases. However, there are minor errors and deviations in the results which are discussed in this section. Here are some of the findings.
From the displacement plots, it is clear that for Mymax load case (flap-wise bending, suction side under compression) the bending-torsion coupling is more pronounced. But the simulation does not show this behavior. From the strain plots, the behavior is almost similar for both the edge-wise bending tests (Mxmax and Mxmin). At the suction side in the belt region the strain values ranges from -30 $\mu\varepsilon_{xx}$ to 180 $\mu\varepsilon_{xx}$. From 7 m to 15 m the strains are a bit underestimated by simulation. But there is a perfect match at the tip. At the pressure side the strain values are in between -30 $\mu\varepsilon_{xx}$ and 30 $\mu\varepsilon_{xx}$. Because the strain values are very less, the deviations are high but in the acceptable range.
At 5 m and 8 m span, the profiles are highly instrumented because these are the critical regions. At 5 m span, the $\mu\varepsilon_{xx}$ strains at the suction side match very well but at the pressure side there is a deviation at 0 mm to 800 mm from the leading edge. The strains in this region are over estimated. The $\mu\varepsilon_{yy}$ at the suction side match very well. But at the pressure side they are again under estimated from 1800 mm to 2400 mm. At 8 m span, the $\mu\varepsilon_{xx}$ strains at both the suction side and pressure side match very well. The $\mu\varepsilon_{yy}$ strains at the suction side from 0 mm to 600 mm from the leading edge, the strains are a bit over estimated by simulation. At the pressure side, a weak non linearity

can be seen in the test results whereas the simulation results are nearly linear. The findings from the flap-wise bending tests are discussed below.
The Mymax (suction side under compression) plots for the belt region at the suction side, the strain values from 7 m to 15 m are a bit under estimated. But there is a perfect match at the tip. There is also a slight mismatch near the root. The plot at the pressure side shows that at 1600 mm the strain is a bit over estimated by simulation. Apart from this there is a perfect match at all the other places.
At the highly instrumented region (5 m span),the $\mu\varepsilon_{xx}$ at the suction side changes direction at about 800 mm from the leading edge. The strains are a bit over estimated around this region. Otherwise there is a perfect match at other places. At the pressure side, the strains are a bit over estimated from 200 mm to 800 mm from the leading edge. The $\mu\varepsilon_{yy}$ strains at the suction side are over estimated by simulation from 0 mm to 1600 mm from the leading edge. Whereas at the pressure side, the strains are over estimated at distance 800 mm to 1200 mm from the leading edge. At 8 m span, the $\mu\varepsilon_{xx}$ strains match perfectly both at the pressure side and suction side. The $\mu\varepsilon_{yy}$ strains at the suction side are over estimated at most of the regions except at the peak where it is under estimated. But the first and the last strain values match perfectly. At the pressure side, the strains at distance 500 mm to 1500 mm from the leading edge, the strains are a bit over estimated.
For the load case, Mymin (pressure side under compression), the strains at the belt region in the suction side, there is a slight mismatch near the root till 5 m span. The strains are a bit over estimated. Otherwise there is a perfect match at other regions. At the pressure side, the strains match very well.
At 5 m span, the $\mu\varepsilon_{xx}$ peak strains at the suction side are a bit over estimated. At the pressure side, at distances 200 mm to 500 mm and at 1200 mm to 1600 mm from the leading edge the strains are over estimated. The $\mu\varepsilon_{yy}$ strains at the suction side, there is a lot of mismatch in the results. The measured strain values from the test are nearly constant from 500 mm to 2000 mm but the simulation values are a bit over estimated. At the pressure side, the strains are over estimated from 1200 mm to 2200 mm from the leading edge. At 8 m span, the $\mu\varepsilon_{xx}$ strains at both the suction and pressure sides match very well. The $\mu\varepsilon_{yy}$ strains at the suction side are nearly constant at distance 500 mm to 1500 mm from the leading edge. But the simulation plot is parabolic and a bit over estimated. At the pressure side, the deviation from 500 mm to 1800 mm is over estimated from simulation. But the peak value is under estimated.

From the torsional stiffness displacement plots it can be seen that the angle of rotation is larger in simulation results in comparison to the test results. From the bending test strain comparisons it is observed that in the pressure side at span length of 5 m, the first four sensor values do not match with the simulation results. This trend is seen in all the bending load cases. Hence it is clear that this mismatch is due to the manufacturing error at this location. The bending and torsion results comparison together proves that the wind turbine blade model is modeled too soft at the outer third the blade.

6.2 Conclusion

Some observations from the project are:

- The simulation results were great and were very close to the test results
- There is a mismatch of results at some regions, the reasons for which have been mentioned in the summary section
- The blade is cut into several components and will be analyzed regarding further manufacturing uncertainties
- The real blade was much stiffer to torsion loads than the modeled blade. This was found out in the stiffness distribution test
- The real blade was heavier than the modeled blade because of the sensors, instrumentation and the wiring

A

Load frame geometry

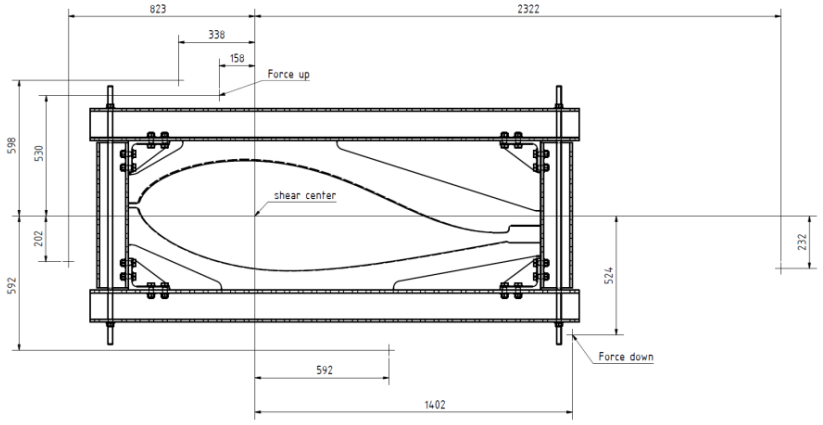

Figure A.1: Torsion test LF2 load and optical measurement points

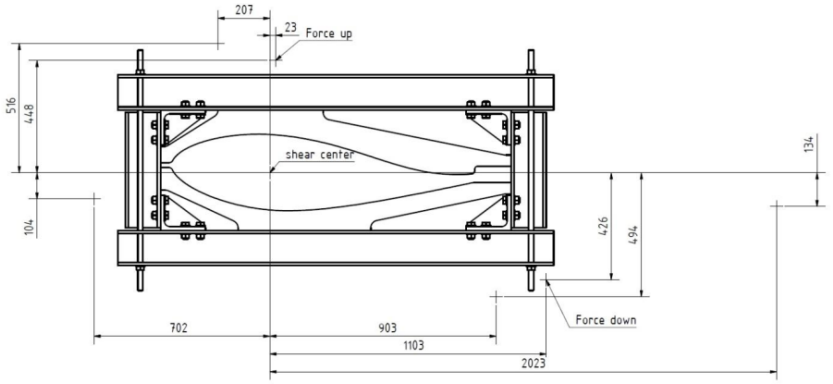

Figure A.2: Torsion test LF3 load and optical measurement points

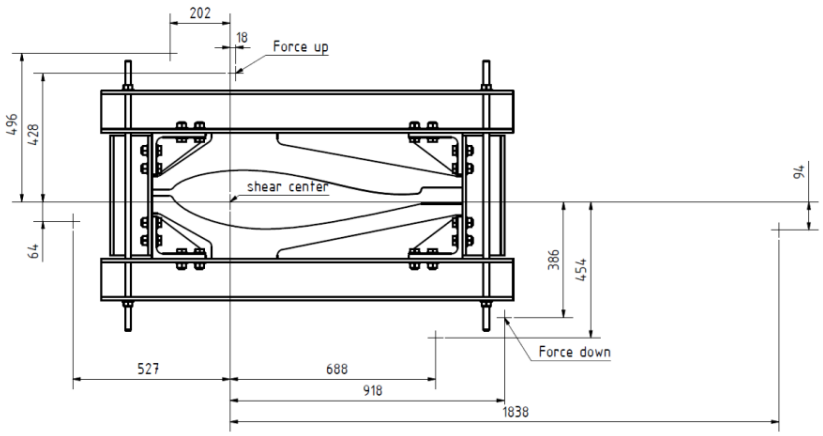

Figure A.3: Torsion test LF4 load and optical measurement points

B

Strain guage list

Radial position [mm]	Strain Gauge	Side	Edge
1600	001_Z01600_SS_LE_00	SS	LE
1600	002_Z01600_PS_LE_00	SS	LE
1600	003_Z01600_PS_SC_00	PS	B
1600	004_Z01600_PS_TE_00	PS	TE
1600	005_Z01600_SS_TE_00	SS	TE
1600	006_Z01600_SS_SC_00	SS	B
1600	007_Z01600_SW_TE_00	SW	TE
1600	008_Z01600_SW_TE_+45	SW	TE
1600	009_Z01600_SW_TE_-45	SW	TE
2700	010_Z02700_SS_LE_00	SS	LE
2700	011_Z02700_PS_LE_00	PS	LE
2700	012_Z02700_PS_SC_00	PS	B
2700	013_Z02700_PS_TE_00	PS	TE
2700	014_Z02700_SS_TE_00	SS	TE
2700	015_Z02700_SS_SC_00	SS	B
3800	016_Z03800_SS_LE_00	SS	TE
3800	017_Z03800_PS_LE_00	PS	TE
3800	018_Z03800_PS_SC_00	SS	B
3800	019_Z03800_PS_TE_00	PS	TE
3800	020_Z03800_SS_TE_00	SS	TE
3800	021_Z03800_SS_SC_00	SS	B
5000	022_Z05000_SS_LE_00	SS	LE
5000	023_Z05000_SS_LE_90	SS	LE
5000	024_Z05000_PS_LE_00	PS	LE
5000	025_Z05000_PS_LE_90	PS	LE
5000	026_Z05000_PS_LE_+45	PS	LE

Continued on next page

Radial position [mm]	Strain Gauge	Side	Edge
5000	027_Z05000_PS_LE_-45	PS	LE
5000	028_Z05000_PS_LE_OPL1_00	PS	LE
5000	029_Z05000_PS_LE_OPL1_90	PS	LE
5000	030_Z05000_PS_LE_OPL2_00	PS	LE
5000	031_Z05000_PS_LE_OPL2_90	PS	LE
5000	032_Z05000_PS_LE_OPL3_00	PS	LE
5000	033_Z05000_PS_LE_OPL3_90	PS	LE
5000	034_Z05000_PS_SC__00	PS	B
5000	035_Z05000_PS_SC__90	PS	B
5000	036_Z05000_PS_SC__+45	PS	B
5000	037_Z05000_PS_SC__-45	PS	B
5000	038_Z05000_PS_TE_OPL4_00	PS	TE
5000	039_Z05000_PS_TE_OPL4_90	PS	TE
5000	040_Z05000_PS_TE_OPL3_00	PS	TE
5000	041_Z05000_PS_TE_OPL3_90	PS	TE
5000	042_Z05000_PS_TE_OPL2_00	PS	TE
5000	043_Z05000_PS_TE_OPL2_90	PS	TE
5000	044_Z05000_PS_TE_OPL1_00	PS	TE
5000	045_Z05000_PS_TE_OPL1_90	PS	TE
5000	046_Z05000_PS_TE__00	PS	TE
5000	047_Z05000_PS_TE__90	PS	TE
5000	048_Z05000_SS_TE__00	SS	TE
5000	049_Z05000_SS_TE__90	SS	TE
5000	050_Z05000_SS_TE__+45	SS	TE
5000	051_Z05000_SS_TE__-45	SS	TE
5000	052_Z05000_SS_TE_OPL1_00	SS	TE
5000	053_Z05000_SS_TE_OPL1_90	SS	TE
5000	054_Z05000_SS_TE_OPL2_00	SS	TE
5000	055_Z05000_SS_TE_OPL2_90	SS	TE
5000	056_Z05000_SS_TE_OPL3_00	SS	TE
5000	057_Z05000_SS_TE_OPL3_90	SS	TE
5000	058_Z05000_SS_TE_OPL4_00	SS	TE
5000	059_Z05000_SS_TE_OPL4_90	SS	TE
5000	060_Z05000_SS_SC__00	SS	B
5000	061_Z05000_SS_SC__90	SS	B
5000	062_Z05000_SS_SC__+45	SS	B

Continued on next page

Radial position [mm]	Strain Gauge	Side	Edge
5000	063_Z05000_SS_SC__-45	SS	B
5000	064_Z05000_SS_LE_OPL3_00	SS	LE
5000	065_Z05000_SS_LE_OPL3_90	SS	LE
5000	066_Z05000_SS_LE_OPL2_00	SS	LE
5000	067_Z05000_SS_LE_OPL2_90	SS	LE
5000	068_Z05000_SS_LE_OPL1_00	SS	LE
5000	069_Z05000_SS_LE_OPL1_90	SS	LE
8000	070_Z08000_SS_LE_00	SS	LE
8000	071_Z08000_SS_LE_90	SS	LE
8000	072_Z08000_PS_LE_00	PS	LE
8000	073_Z08000_PS_LE_90	PS	LE
8000	074_Z08000_PS_LE_+45	PS	LE
8000	075_Z08000_PS_LE_-45	PS	LE
8000	076_Z08000_PS_LE_OPL1_00	PS	LE
8000	077_Z08000_PS_LE_OPL1_90	PS	LE
8000	078_Z08000_PS_LE_OPL2_00	PS	LE
8000	079_Z08000_PS_LE_OPL2_90	PS	LE
8000	080_Z08000_PS_SC__00	PS	B
8000	081_Z08000_PS_SC__90	PS	B
8000	082_Z08000_PS_SC__+45	PS	B
8000	083_Z08000_PS_SC__-45	PS	B
8000	084_Z08000_PS_TE_OPL4_00	PS	TE
8000	085_Z08000_PS_TE_OPL4_90	PS	TE
8000	086_Z08000_PS_TE_OPL3_00	PS	TE
8000	087_Z08000_PS_TE_OPL3_90	PS	TE
8000	088_Z08000_PS_TE_OPL2_00	PS	TE
8000	089_Z08000_PS_TE_OPL2_90	PS	TE
8000	090_Z08000_PS_TE_OPL1_00	PS	TE
8000	091_Z08000_PS_TE_OPL1_90	PS	TE
8000	092_Z08000_PS_TE__00	PS	TE
8000	093_Z08000_PS_TE__90	PS	TE
8000	094_Z08000_SS_TE__00	SS	TE
8000	095_Z08000_SS_TE__90	SS	TE
8000	096_Z08000_SS_TE__+45	SS	TE
8000	097_Z08000_SS_TE__-45	SS	TE
8000	098_Z08000_SS_TE_OPL1_00	SS	TE

Continued on next page

Radial position [mm]	Strain Gauge	Side	Edge
8000	099_Z08000_SS_TE_OPL1_90	SS	TE
8000	100_Z08000_SS_TE_OPL2_00	SS	TE
8000	101_Z08000_SS_TE_OPL2_90	SS	TE
8000	102_Z08000_SS_TE_OPL3_00	SS	TE
8000	103_Z08000_SS_TE_OPL3_90	SS	TE
8000	104_Z08000_SS_TE_OPL4_00	SS	TE
8000	105_Z08000_SS_TE_OPL4_90	SS	TE
8000	106_Z08000_SS_SC__00	SS	B
8000	107_Z08000_SS_SC__90	SS	B
8000	108_Z08000_SS_SC__+45	SS	B
8000	109_Z08000_SS_SC__-45	SS	B
8000	110_Z08000_SS_LE_OPL2_00	SS	LE
8000	111_Z08000_SS_LE_OPL2_90	SS	LE
8000	112_Z08000_SS_LE_OPL1_00	SS	LE
8000	113_Z08000_SS_LE_OPL1_90	SS	LE
8000	114_Z08000_SW_TE_00	SW	TE
8000	115_Z08000_SW_TE_+45	SW	TE
8000	116_Z08000_SW_TE_-45	SW	TE
11000	117_Z11000_SS_LE_00	SS	LE
11000	118_Z11000_PS_LE_00	PS	LE
11000	119_Z11000_PS_SC_00	PS	B
11000	120_Z11000_PS_TE_00	PS	TE
11000	121_Z11000_SS_TE_00	SS	TE
11000	122_Z11000_SS_SC_00	SS	B
13000	123_Z13000_SS_LE_00	SS	LE
13000	124_Z13000_PS_LE_00	PS	LE
13000	125_Z13000_PS_SC_00	PS	B
13000	126_Z13000_PS_TE_00	PS	TE
13000	127_Z13000_SS_TE_00	SS	TE
13000	128_Z13000_SS_SC_00	SS	B
15000	129_Z15000_SS_LE_00	SS	LE
15000	130_Z15000_PS_TE_00	PS	TE
15000	131_Z15000_PS_LE_00	PS	LE
15000	132_Z15000_PS_LE_+45	PS	LE
15000	133_Z15000_PS_LE_-45	PS	LE
15000	134_Z15000_PS_SC_00	PS	TE

Continued on next page

Radial position [mm]	Strain Gauge	Side	Edge
15000	135_Z15000_PS_SC_+45	PS	TE
15000	136_Z15000_PS_SC_-45	PS	TE
15000	137_Z15000_SS_TE_00	SS	TE
15000	138_Z15000_SS_TE_+45	SS	TE
15000	139_Z15000_SS_TE_-45	SS	TE
15000	140_Z15000_SS_SC_00	SS	B
15000	141_Z15000_SS_SC_+45	SS	B
15000	142_Z15000_SS_SC_-45	SS	B
15000	143_Z15000_SW_TE_00	SW	TE
15000	144_Z15000_SW_TE_+45	SW	TE
15000	145_Z15000_SW_TE_-45	SW	TE
17000	146_Z17000_SS_LE_00	SS	LE
17000	147_Z17000_PS_LE_00	PS	LE
17000	148_Z17000_PS_SC_00	PS	LE
17000	149_Z17000_PS_TE_00	PS	TE
17000	150_Z17000_SS_TE_00	SS	TE
17000	151_Z17000_SS_SC_00	SS	B

Table B.1: List of strain gauges at components (PS - pressure side, SS - suction side, SW - shear web)and position (LE - leading edge, TE - trailing edge, B - belt).

C

List of Figures

2.1 Example of an airfoil cross section of a wind turbine blade with two shear webs. 7

2.2 Picture of a SmartBlade developed by DLR and Fraunhofer IWES 8

2.3 SOLID186 - 3-D 20-Node homogeneous Structural Solid 11

2.4 SHELL281 - 8-Node Shell 12

2.5 MASS21 Structural point Mass 13

3.1 Positions of strain gauges and load frames (Distances in mm) 16

3.2 Configuration example of a static loading rotor blade test performed by Fraunhofer IWES in Bremerhaven - Source: report of Bernd Haller [4] 17

3.3 Blade orientation Mx load cases. 18

3.4 Blade orientation My and torsion load cases. 19

3.5 Definition of a strain gauge rosette. 19

3.6 Torsion test - Forces (represented by red arrows) - Figure taken from the report of Bernd Haller [4] 21

4.1 Reference planes of the finite shell elements and stacking direction 25

4.2 Upper shell of the wind turbine blade to illustrate assumptions made at the trailing edge (black circle). 26

4.3 Visualization of the shell and solid element distribution in a cross section. 26

4.4 Boundary Condition 27

4.5 Load introduction 27

5.1 Displacements at position $R = 6700\,mm$ for all bending load cases. 30

5.2 Displacements at position $R = 9700\,mm$ for all bending load cases. 30

5.3 Displacements at position $R = 14000\,mm$ for all bending load cases. 31

5.4 Displacements at position $R = 17700\,mm$ for all bending load cases. 31

5.5 Definition of paths for comparing experimental and numerical results. 32

5.6 Strain comparison ε_{xx} for Mxmax load case. 34

5.7 Strain comparison ε_{xx} at radial position $R = 1600\ mm$ for Mxmax load case. 35

5.8 Strain comparison ε_{xx} at radial position $R = 2700\ mm$ for Mxmax load case. 35

5.9 Strain comparison ε_{xx} at radial position $R = 3800\ mm$ for Mxmax load case. 36

5.10 Strain comparison ε_{xx} at radial position $R = 5000\ mm$ for Mxmax load case. 37

5.11 Strain comparison ε_{yy} at radial position $R = 5000\ mm$ for Mxmax load case. 38

5.12 Strain comparison ε_{xx} at radial position $R = 8000\ mm$ for Mxmax load case. 39

5.14 Strain comparison ε_{yy} at radial position $R = 8000\ mm$ for Mxmax load case. 40

5.15 Strain comparison ε_{xx} at radial position $R = 11000\ mm$ for Mxmax load case. 41

5.16 Strain comparison ε_{xx} at radial position $R = 13000\ mm$ for Mxmax load case. 41

5.17 Strain comparison ε_{xx} at radial position $R = 15000\ mm$ for Mxmax load case. 42

5.18 Strain comparison ε_{xx} at radial position $R = 17000\ mm$ for Mx-max load case. 42

5.19 Strain comparison ε_{xx} for Mxmin load case. 44

5.20 Strain comparison ε_{xx} at radial position $R = 1600\ mm$ for Mxmin load case. 45

5.21 Strain comparison ε_{xx} at radial position $R = 2700\ mm$ for Mxmin load case. 46

5.22 Strain comparison ε_{xx} at radial position $R = 3800\ mm$ for Mxmin load case. 46

5.23 Strain comparison ε_{xx} at radial position $R = 5000\ mm$ for Mxmin load case. 47

5.24 Strain comparison ε_{yy} at radial position $R = 5000\ mm$ for Mxmin load case. 48

5.25 Strain comparison ε_{xx} at radial position $R = 8000\ mm$ for Mxmin load case. 49

5.27 Strain comparison ε_{yy} at radial position $R = 8000\ mm$ for Mxmin load case. 50

5.28 Strain comparison ε_{xx} at radial position $R = 11000\ mm$ for Mxmin load case. 51

5.29 Strain comparison ε_{xx} at radial position $R = 13000\ mm$ for Mxmin load case. 51

5.30 Strain comparison ε_{xx} at radial position $R = 15000\ mm$ for Mxmin load case. 52

5.31 Strain comparison ε_{xx} at radial position $R = 17000\ mm$ for Mxmin load case. 52

5.32 Strain comparison ε_{xx} for Mymax load case. 54

5.33 Strain comparison ε_{xx} at radial position $R = 1600\ mm$ for My-max load case. 55

5.34 Strain comparison ε_{xx} at radial position $R = 2700\ mm$ for My-max load case. 55

5.35 Strain comparison ε_{xx} at radial position $R = 3800\ mm$ for My-max load case. 56

5.36 Strain comparison ε_{xx} at radial position $R = 5000\ mm$ for Mymax load case. 57

5.37 Strain comparison ε_{yy} at radial position $R = 5000\ mm$ for Mymax load case. 58

5.38 Strain comparison ε_{xx} at radial position $R = 8000\ mm$ for Mymax load case. 59

5.40 Strain comparison ε_{yy} at radial position $R = 8000\ mm$ for Mymax load case. 60

5.41 Strain comparison ε_{xx} at radial position $R = 11000\ mm$ for Mymax load case. 61

5.42 Strain comparison ε_{xx} at radial position $R = 13000\ mm$ for Mymax load case. 61

5.43 Strain comparison ε_{xx} at radial position $R = 15000\ mm$ for Mymax load case. 62

5.44 Strain comparison ε_{xx} at radial position $R = 17000\ mm$ for Mymax load case. 62

5.45 Strain comparison ε_{xx} for Mymin load case. 65

5.46 Strain comparison ε_{xx} at radial position $R = 1600\ mm$ for Mymin load case. 66

5.47 Strain comparison ε_{xx} at radial position $R = 2700\ mm$ for Mymin load case. 67

5.48 Strain comparison ε_{xx} at radial position $R = 3800\ mm$ for Mymin load case. 67

5.49 Strain comparison ε_{xx} at radial position $R = 5000\ mm$ for Mymin load case. 68

5.50 Strain comparison ε_{yy} at radial position $R = 5000\ mm$ for Mymin load case. 69

5.51 Strain comparison ε_{xx} at radial position $R = 8000\ mm$ for Mymin load case. 70

5.53 Strain comparison ε_{yy} at radial position $R = 8000\ mm$ for Mymin load case. 71

5.54 Strain comparison ε_{xx} at radial position $R = 11000\ mm$ for Mymin load case. 72

5.55 Strain comparison ε_{xx} at radial position R = 13000 mm for Mymin load case. 72

5.56 Strain comparison ε_{xx} at radial position R = 15000 mm for Mymin load case. 73

5.57 Strain comparison ε_{xx} at radial position R = 17000 mm for Mymin load case. 73

5.58 Displacements at position R = 6700 mm for all torsion load cases. 75

5.59 Displacements at position R = 9700 mm for all torsion load cases. 75

5.60 Displacements at position R = 14000 mm for all torsion load cases. 76

5.61 Displacements at position R = 17700 mm for all torsion load cases. 76

5.62 Strain comparison ε_{xx} at radial position R = 5000 mm for torsion load case LC_1. 77

5.63 Strain comparison ε_{yy} at radial position R = 5000 mm for torsion load case LC_1. 78

5.64 Strain comparison ε_{xx} at radial position R = 8000 mm for torsion load case LC_1. 79

5.65 Strain comparison ε_{yy} at radial position R = 8000 mm for torsion load case LC_1. 80

5.66 Strain comparison ε_{xx} at radial position R = 5000 mm for torsion load case LC_2. 81

5.67 Strain comparison ε_{yy} at radial position R = 5000 mm for torsion load case LC_2. 82

5.68 Strain comparison ε_{xx} at radial position R = 8000 mm for torsion load case LC_2. 83

5.69 Strain comparison ε_{yy} at radial position R = 8000 mm for torsion load case LC_2. 84

5.70 Strain comparison ε_{xx} at radial position R = 5000 mm for torsion load case LC_3. 85

5.71 Strain comparison ε_{yy} at radial position $R = 5000\ mm$ for torsion load case LC_3. 86

5.72 Strain comparison ε_{xx} at radial position $R = 8000$ mm for torsion load case LC_3. 87

5.73 Strain comparison ε_{yy} at radial position $R = 8000$ mm for torsion load case LC_3. 88

A.1 Torsion test LF2 load and optical measurement points 93

A.2 Torsion test LF3 load and optical measurement points 93

A.3 Torsion test LF4 load and optical measurement points 94

D

List of Tables

3.1 Applied loads for all the bending load cases 20

3.2 Distance between the draw wire sensors placed in the leading and trailing edges for all the torsion test scenarios 21

3.3 Applied loads for all the torsion load cases 22

4.1 Material parameters based on [25]. 1-Values after matrix infusion 23

4.2 Material number in the finite element models 24

B.1 List of strain gauges at components (PS - pressure side, SS - suction side, SW - shear web)and position (LE - leading edge, TE - trailing edge, B - belt). 99

E

Bibliography

[1] BMWi. *Renewable Energy*, 2019 (accessed September 4, 2019). https://www.bmwi.de/Redaktion/EN/Dossier/renewable-energy.html.

[2] Tyler J. Stehly, Donna M. Heimiller, and George N. Scott. 2016 cost of wind energy review. 12 2017.

[3] Robert Wood, AbuBakr Bahaj, Stephen Turnock, Ling Wang, and M.-H Evans. Tribological design constraints of marine renewable energy systems. *Philosophical transactions. Series A, Mathematical, physical, and engineering sciences*, 368:4807–27, 10 2010.

[4] Bernd Haller. SmartBlades 2 - Combined deliverable report; Del 1.2.2.1, Del 1.2.2.2, Del 1.2.2.3. Technical report, Fraunhofer IWES, 2018.

[5] D. Griffith and Thomas Carne. *Experimental Modal Analysis of 9-meter Research-sized Wind Turbine Blades*, volume 44, pages 1–14. 07 2011.

[6] J. Schaarup and T. Krogh. Dnv-risø "guidelines for design of wind turbines". 2001. Risø vinddag 2001 ; Conference date: 28-11-2001 Through 28-11-2001.

[7] Fethullah Özlük. *Wind Turbine Blade Design*. PhD thesis, 06 2015.

[8] Ali Almukhtar. Effect of drag on the performance for an efficient wind turbine blade design. *Energy Procedia*, 18:404–415, 12 2012.

[9] Mick Sagrillo. Small turbine column. *Windletter*, 29(1), 2010.

[10] A Ning and K Dykes. Understanding the benefits and limitations of increasing maximum rotor tip speed for utility-scale wind turbines. *Journal of Physics: Conference Series*, 524:012087, jun 2014.

[11] Asis Sarkar and Dhiren Kumar Behera. Wind turbine blade efficiency and power calculation with electrical analogy.

[12] S.M. Habali and Ibraheem Saleh. Local design, testing and manufacturing of small mixed airfoil wind turbine blades of glass fiber reinforced plastics: Part ii: Manufacturing of the blade and rotor. *Energy Conversion and Management*, 41:281–298, 02 2000.

[13] Ole Thomsen. Sandwich materials for wind turbine blades – present and future. *Journal of Sandwich Structures and Materials - J SANDW STRUCT MATER*, 11:7–26, 01 2009.

[14] R. Allemang. *Special Topics in Structural Dynamics, Volume 6: Proceedings of the 33rd IMAC, A Conference and Exposition on Structural Dynamics, 2015*. Conference Proceedings of the Society for Experimental Mechanics Series. Springer International Publishing, 2015.

[15] H.F. Zhou, H.Y. Dou, L.Z. Qin, Y. Chen, Y.Q. Ni, and J.M. Ko. A review of full-scale structural testing of wind turbine blades. *Renewable and Sustainable Energy Reviews*, 33:177 – 187, 2014.

[16] D. N.V. GL. Dnvgl-st-0376 rotor blades for wind turbines.

[17] Per Hørlyk Nielsen, Peter Berring, Christian Pavese, and Kim Branner. *Rotor blade full-scale fatigue testing technology and research*. DTU Wind Energy, Denmark, 2013.

[18] Othman Al-Khudairi, Homayoun Hadavinia, Christian Little, Gavin Gillmore, Peter Greaves, and Kirsten Dyer. Full-scale fatigue testing of a wind turbine blade in flapwise direction and examining the effect of crack propagation on the blade performance. *Materials*, 10:1152, 10 2017.

[19] Magda Nielsen, Agnieszka Roczek-Sieradzan, Per H. Nielsen, Peter Berring, Tomasz Sieradzan, Vatslav Roudnitski, Robert D. Bitsche, Henrik Witthøft Knudsen, Anders B. Rasmussen, Jens Jakob Aagaard Rasmussen, Ulla Uldahl, Zuzana Andrlová, Kim Branner, Christian Bak, Bjarne Skovmose Kallesøe, Malcolm McGugan, Mikkel Lagerbon, Jakob Wedel-Heinen, Torben Lindby, Hans Jørgen Riber, and Christian Jensen. Full scale test ssp 34m blade, edgewise loading ltt. extreme load and poc_inve data report. 2010.

[20] C. Kong, J. Bang, and Y. Sugiyama. Structural investigation of composite wind turbine blade considering various load cases and fatigue life. *Energy*, 30(11):2101 – 2114, 2005. International Symposium on CO2 Fixation and Efficient Utilization of Energy (CandE 2002) and the International World Energy System Conference (WESC-2002).

[21] Magda Nielsen, Find M Jensen, H Nielsen, Peter Berring, Karolina Martyniuk, Agnieszka Roczek, Tomasz Sieradzan, Vatslav Roudnitski, Piotr Kucio, Robert Bitsche, Peter Andresen, Troels Lukassen, Zuzana Andrlová, Kim Branner, Christian Bak, Bjarne Kallesøe, Malcolm Mcgugan, Jakob Wedel-Heinen, Torben Lindby, and Jens Jakob Rasmussen. Full scale test of ssp 34m blade, edgewise loading ltt: Data report 1, 01 2010.

[22] Kim Branner, Find Jensen, Peter Berring, Amit Puri, Andrew Morris, and John Dear. Effect of sandwich core properties on ultimate strength of a wind turbine blade. 05 2008.

[23] Changduk Kong, Yoshihiko Sugiyama, J Lee, and Constantinos Soutis. Full scale structural experimental investigation of an e-glass/epoxy composite wind turbine blade. *Advanced Composites Letters*, 11:207–219, 09 2002.

[24] Stefan Keil. *Technology and Practical Use of Strain Gages With Particular Consideration of Stress Analysis Using Strain Gages: With Particular Consideration of Stress Analysis Using Strain Gages*. Wilhelm Ernst & Sohn, Verlag für Architektur und technische Wissenschaften GmbH & Co. KG , 2017.

[25] Wolfgang Heydlauff. Materialspezifikation der Faserverbundwerkstoffe für das Rotorblatt IWES20.0 - Testbench Version - Rev. 2.0. Technical report, Aero Dynamik Consult, 2018.

[26] Robert M Jones. *Mechanics of composite materials*. CRC press, 2014.

Versicherung an Eides Statt

Ich versichere an Eides statt durch meine untenstehende Unterschrift,

- dass ich die vorliegende Arbeit - mit Ausnahme der Anleitung durch die Betreuer - selbstständig ohne fremde Hilfe angefertigt habe und
- dass ich alle Stellen, die wörtlich oder annähernd wörtlich aus fremden Quellen entnommen sind, entsprechend als Zitate gekennzeichnet habe und
- dass ich ausschließlich die angegebenen Quellen (Literatur, Internetseiten, sonstige Hilfsmittel) verwendet habe und
- dass ich alle entsprechenden Angaben nach bestem Wissen und Gewissen vorgenommen habe, dass sie der Wahrheit entsprechen und dass ich nichts verschwiegen habe.

Mir ist bekannt, dass eine falsche Versicherung an Eides Statt nach § 156 und nach § 163 Abs. 1 des Strafgesetzbuches mit Freiheitsstrafe oder Geldstrafe bestraft wird.

.....	.....
Ort, Datum	Unterschrift